Monte Carlo simulations of Hall effect in variable range hopping systems

Mathias Storhaug Reistad

Thesis for the degree of Master of Science
in Condensed Matter Physics

Department of Physics
Faculty of Mathematics and Natural Sciences
University of Oslo

Spring 2019

Acknowledgements

First and foremost I would like to thank my two supervisors, Professor Joakim Bergli and Professor emeritus Yuri Galperin. Joakim's humble yet analytic intuition helped me more than anything in understanding this world of material physics and disordered systems. Your eagerness and enthusiasm for physics inspired me to work hard and to learn more.

I see Yuri is a man of vast knowledge. His many years of experience in the subject of semiconductor physics and variable range hopping makes him a true expert. He knows what there is to know, and understands what there is to understand. He is always open and welcoming of both easy and difficult questions. Your guidance and wisdom was instrumental in forming my understanding of variable range hopping.

I need to thank my family. Especially my parents, Knut and Ragnhild, for their continuous support and encouragement. You have always been there for me. And you always give me the advice I needed. I'm grateful for everything you have given me. I would like to thank each member of the "Sunday dinner club" personally. Ole Kristian, Maria, Ole Tobias, Konstanse, Camilla, Nabil and Karen, you really made Oslo feel like a home to me. I don't know if I could have done this if it were not for you.

Thank you to fellow student Joachim Brodin, for reading my thesis and giving me good constructive feedback. You made me consider the human element of reading a thesis, and I think I gained greatly from it. I wish you good luck in the years to come!

Last, but not least, I need to thank my love, Evgeniya. Even from Moscow you have given me endless support and encouragement in my studies and life. Meeting you has changed my life for the better. I look forward to many more crazy and exciting adventures together with you.

The wonderful subject of variable range hopping is already several decades old. Its authors and researchers are many. Some of the most important works in variable range hopping stem from the Ioffe Physical-Technical Institute in Saint Petersburg, Russia. My supervisor Yuri Galperin studied there, and worked with some of these men who made remarkable contributions to the science of variable range hopping. He brough this field of study with him when he moved to Norway. He taught it to his student, Joakim Bergli, my advisor. And now Joakim Bergli has taught it to me. In this sense I feel like a great-grandstudent of the Ioffe Institute and its great history. In a sense I feel honored.

Mathias Storhaug Reistad

Oslo, June 2019

Abstract

This thesis concerns itself with the ordinary Hall effect in variable range hopping systems. The best example of such a system occurs in compensated, lightly doped semiconductors at temperatures of a few Kelvin. In this state, the semiconductor acts as an insulator and electrons are highly localized to impurity states. The resultant transport in this system is only possible via phonon assisted tunneling, given the name variable range hopping (VRH). There are two types of VRH, Efros-Shklovskii (ES) VRH which considers dynamic Coulomb interactions of donor states, and Mott VRH which neglects this interaction. Both with their respective conductivity laws that are studied in this thesis. The Hall effect plants itself in VRH systems via constructive interference of the Aharanov-Bohm phases between different electron paths.

We have developed a kinetic Monte Carlo algorithm that simulate the time development of charge transport in a VRH system in external electric and magnetic field. We use periodic boundary conditiosn and a lattice model for the main simulations. The longitudinal and Hall conductivities, σ_x and σ_H respectively, are measured from simulations. In the Mott case, results align almost perfectly with theoretical predictions and experimental results. There are small deviations that were explained as lattice effects. In the ES case, simulated σ_x acted as expected whereas σ_H did not. ES regime σ_H featured large fluctuations making it difficult to draw precise conclusions. The cause of these fluctuations is not known, but a possible explanations is given. The sign of the Hall effect is found to be independent of charge carrier, in agreement with established VRH theory.

Contents

Source code

The source code for simulations used in this project is given in
https://github.com/mathisre/KMC-algorithm-for-Hall-effect-in-VRH

CHAPTER 1

Introduction

Semiconductors have had a tremendous impact on human life. The technological applications have revolutionized human life far more than anyone could have anticipated. With the significant importance of these materials, it has become the area of focus for scientists everywhere. Almost every aspect of these materials are studied with great enthusiasm. In this project we turn our eyes to conductivity in the low-temperature regime of the compensated semiconductor, the *hopping conduction regime*.

First proposed by Mott [1] and Convell [2], and independently by Anderson *et al*, hopping conduction is a *phonon induced* process that allows charge transport through hopping between *highly localized impurity states*. Such states are highly *disordered*, both positionally and energetically. The wavefunction overlap between highly localized neighboring states decreases exponentially with the distance between them. This results in a conductivity that tends to zero as the temperature is lowered. Hopping conduction is the dominant conduction mechanism at temperatures low enough such that no electrons are present in the conduction band, typically at a few Kelvin. The electron jumps have the interesting property of hopping-length increasing with decreasing temperature. This property has given the mechanism the name variable range hopping (VRH). It has later been discovered that VRH occurs not only in compensated semiconductors, but also in granular materials [3] and quantum dots [4].

There are two laws for VHR conduction, Mott's law and Efros-Shklovskii's law. Generally Mott's law describes hopping in amorphous materials, and Efros-Shklovskii's law describes hopping in crystalline semiconductors where Coulomb interactions are important. With these laws, variable range hopping conduction is adequately described.

The Hall effect in the VRH regime was a difficult question for a large number of years. Holstein [5] was the first to prove that there should be a Hall effect associated with hopping conduction. It should arise from interference between electron jumps on a minimum of three sites. Using his premises, other scientists used percolation methods to develop theories for the Hall mobility with similar yet different results [6–9].

Normal conductivity is very small, but possible to measure. The Hall conductivity is even more small and experimental measurements have proven difficult. Magnetoresistance adds another layer of difficulty to measurements. Initial experiments in the 1960s and 1970s showed no result, the instruments at the time weren't sensitive enough to measure the very small Hall effect. The first measurements of the Hall conductivity were made in 1987 [10] and were in

good agreement with predictions from Ref. [6]. Later experiments [11–14] found results on the same function form, but with parameter values in disagreement with Refs. [6] and [10].

The first simulations of VRH Hall effect were done in 1981. Percolation methods were used to measure the Hall mobility as function of concentration [15, 16]. Later simulations were performed in 2018 [17], again using percolation methods. Percolation methods are static methods and don't perform any time evolution. Time correlation effects such as dynamic Coulomb interactions and polaron clouds cannot be included from such methods.

For many years, time evolving Monte Carlo simulations of VRH conductivity have been slow and computationally inefficient. The development of the dynamic Monte Carlo algorithm by Tsigankov et al [18]. has made such simulations much more efficient and realistic to perform. Such simulations have been used to successfully study important qualities of VRH conduction [19, 20]. To date there are no time evolution simulations of the VRH Hall effect. The aim of this thesis is to perform such simulations.

1.1 Project goals

The aim of this thesis is to use Kinetic Monte-Carlo (KMC) methods to simulate the time evolution of VRH hopping conduction under the influence of magnetic fields, and to measure the temperature dependence of the Hall effect that arises in these simulations. To our knowledge, such simulations have not as of yet been conducted.

The first challenge of this thesis is to establish the KMC algorithm that best fits the problem. There are three KMC algorithms that will be discussed, the rejection-free algorithm, the rejection algorithm and the dynamic algorithm [18]. The programming starting point is a C++ code with Tsignakov's dynamic algorithm, developed by Martin Kirkengen and Andreas Glatz. The code has been used in previously published scientific works [19–21]. The second challenge is to extend the code to include Holstein's equations and make it produce a Hall effect.

Once a working program is established, the temperature dependence of the Hall effect will be studied. Simulation measurements can be tested against known VRH Hall effect theories, experiments and percolation simulations.

The thesis is structured as follows. Semiconductors is where VRH research began, therefore it is a good topic to study to understand VRH. Chapter 2 gives an understanding of semiconductors, percolation theory and the VRH mechanism when there are no magnetic fields present. Chapter 3 aims to explain the Hall effect and how it is expected to behave in VRH conditions. Chapter 4 details the algorithms that are used in this thesis and how measurements of system properties can be made. Chapter 5 covers the results produced in the present work, and discusses them. Finally chapter 6 summarizes the main findings and discusses possible next steps.

CHAPTER 2

Semiconductors and variable range hopping (VRH)

The aim of this chapter is to build an understanding of VRH conductivity. Before discussing VRH, semiconductors and phenomenological percolation theory is covered.

2.1 Lightly doped semiconductors

Semiconductors are materials that have small energy gaps between valence and conduction bands. At temperatures below the semiconductor band gap, there are free charge carriers in the conduction band and the valence band is completely filled. As a result the electrons are localized to their atoms and cannot move through the material.

The properties of semiconductors are altered by doping with acceptor or donor impurities. The energy levels are displayed in Fig. 2.1. Acceptor impurities are atoms with one less electron than the intrinsic semiconductor atoms. They leave one empty energy state close to the valence band. This allows intrinsic electrons to be excited to these states even at low temperatures. The empty state left by the excited electron creates holes in the valence band. The holes act as positive charge carriers and the hole state is able to move through the material, making it able to pass current. Donor impurities have one more electron than the intrinsic atoms. The extra electron state has energy just below the conduction band. These electrons are easily excited to the conduction band and the semiconductor can pass current through these negative charge carriers. Acceptor (donor) doped semiconductors are often called p(n)-type. A semiconductor with both types of impurities is called a *compensated* semiconductor. The degree of compensation, K, refers the ratio of acceptor to donor concentration N_A/N_D.

Let us investigate the properties of the donor state. Assume that it is localized to the atom. The electron feels Coulomb interaction from the other electrons and the nucleus. The electrons and protons screen each other such that the electron effectively only feels $+1$ charge from the atomic nucleus. The scenario described can be approximated as a 2-body hydrogen-like problem. There are only two necessary alterations, the particle mass m_0 needs to be replaced with the effective mass m^*, and the dielectric constant κ needs to be included by replacing ϵ_0 with $\epsilon_0\kappa$. The effective mass accounts for how particles actually move, and depends on the band structure. The dielectric constant is included to account for the polarization of the environment the donor electron is submerged in. The equation for the hydrogen ground state

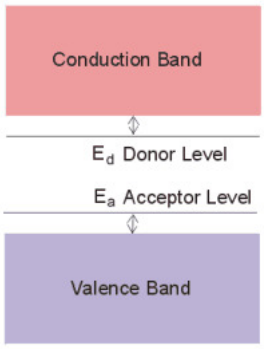

Figure 2.1: Energy levels in a semiconductor with acceptor and donor impurities. Figure taken from Ref. [22].

energy is

$$E = -\frac{me^4}{2(4\pi\epsilon_0)^2\hbar^2} = -\frac{e^2}{8\pi\epsilon_0 a}, \quad a = \frac{4\pi\epsilon_0\hbar^2}{me^2},$$

where a is the Bohr radius, often called the localization length. Putting the effective mass and dielectric constant into the hydrogen ground state gives the donor energy E_d. The result is

$$E_d = -\frac{m^*e^4}{2(4\pi\kappa\epsilon_0)^2\hbar^2} = -\frac{e^2}{8\pi\epsilon_0\kappa a}, \quad a = \frac{4\pi\kappa\epsilon_0\hbar^2}{m^*e^2}, \tag{2.1}$$

The donor wavefunction is on the form

$$\psi(r) \propto e^{-r/a}, \tag{2.2}$$

same as the hydrogen ground state wavefunction. The donor state acts like a hydrogen electron in it's ground state. The localization length of the donor electron is of special interest. The value of m^* for the donor state can vary a lot between semiconductors. To give some examples $m^* = 1.06m_0$ in Si semiconductors at 4K [23], and $m^* = 0.066m_0$ in GaAs [24][1]. Typical values are $m^* < m_0$. The dielectric constant is always > 1. This means the localization length of the donor electron is quite large, and often bigger than the lattice constant. While still localized to the donor atom, the donor electron state wavefunction can extend over many intrinsic atoms. It is important to consider how much the wavefunctions of neighboring donors overlap. If this overlap is *small* then the semiconductor is said to be only lightly doped. This occurs when $Na^3 \ll 1$, with N as the concentration of impurities. A key feature of lightly doped conductors is the exponentially vanishing conductivity as $T \to 0$, whereas the conductivity of a heavily doped semiconductors is only weakly temperature dependent [25].

2.1.1 Conductivity in lightly doped semiconductors

The conductive behavior of semiconductors has severe variations with temperature. A qualitative sketch of the logarithmic resistivity is displayed in Fig. 2.2. Consider a n-type semiconductor (the arguments are similar for p-type). In region A, the conductance is primarily caused by intrinsic electrons. The high temperature allows valence band electrons to be excited

[1] page 201

to the conduction band. Region B corresponds to temperatures below the band-gap, such that only impurity charges can pass current. Region C is a gradual freeze-out of impurity charges from the conduction band.

In Region D conduction is purely caused by transport through impurity states. This only happens in compensated semiconductors, as empty states are a requirement. In highly doped semiconductors, the donor states have a large overlap causing electrons to be delocalized. It can be described as an *impurity band* of free moving electrons. If the impurity concentration is small, in lightly doped semiconductors, there is only a small overlap and states are heavily localized. In the localized system electrons can hop from occupied to empty donor states. This is called *hopping conduction*. It should be noted that hopping conduction does not only occur in lightly doped semiconductors, other examples are granular materials [3] and arrays of quantum dots [4, 26].

It is possible to break down region D further. First is nearest neighbor hopping. As the name implies, jumps happen almost exclusively between nearest-neighbor donor sites. The region is associated with a constant activation energy. The final region is *variable range hopping* (VRH). In VRH the activation energy is itself a function of temperature. The region features an increasing average jump length as the temperature sinks.

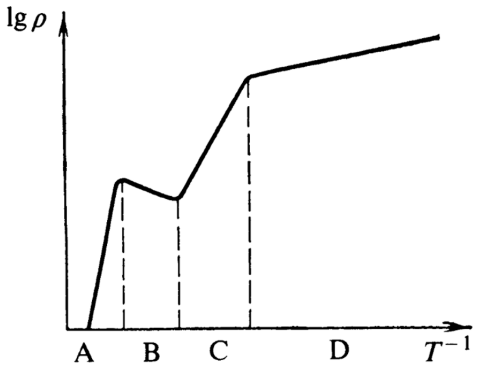

Figure 2.2: Logarithmic resistivity ρ variations with inverse temperature. There are 4 highlighted conduction regions: A: intrinsic electrons, B: donor (acceptor) electrons (holes) conduct in conduction (valence) bands, C: gradual freeze-out region of extrinsic charge carriers from the valence band, D: impurity conduction. Figure taken from Ref. [25] p. 75.

Semiconductors can be either *amorphous* or *crystalline*. The intrinsic atoms of an crystalline semiconductors are located on an ordered lattice. In amorphous materials they are disorderly located. Amorphous semiconductors might still be ordered on a small-scale, but there is no long range order like in crystalline semiconductors. In both amorphous and crystalline semiconductors the impurity atoms are disorderly positioned. The deformation potential approximation is a way of dealing with crystal deformations. Due to it, the potential energy is fluctuating through the material. Amorphous semiconductors experience larger fluctuations than crystalline ones. The deformation potential is often referred to as the *disorder* potential ϕ.

Consider a compensated lightly doped semiconductor with more donors than acceptors at $T = 0K$. N_A donor electrons are de-excited to the acceptor states, leaving $N_D - N_A$ electrons in

the donor states. There is an equal number of positively charged donors and negatively charged acceptors, and there are $N_D - N_A$ neutral donors. The impurities in the material are located in a semi-random structure. Each impurity site experiences a unique charge configuration experiences, leading to a random and fluctuating Coulomb potential. The Coulomb potential changes every time an electron is moved, meaning the site potentials are changing with time.

The impurity site potentials are randomized both by the deformation potential and the Coulomb interaction. The energy situation at $T = 0K$ is displayed in Fig. 2.3a. The site energies are randomly distributed and all the donor levels below the Fermi level are filled. Since the site potentials are different, every jump is happens with the absorption or emission of a phonon.

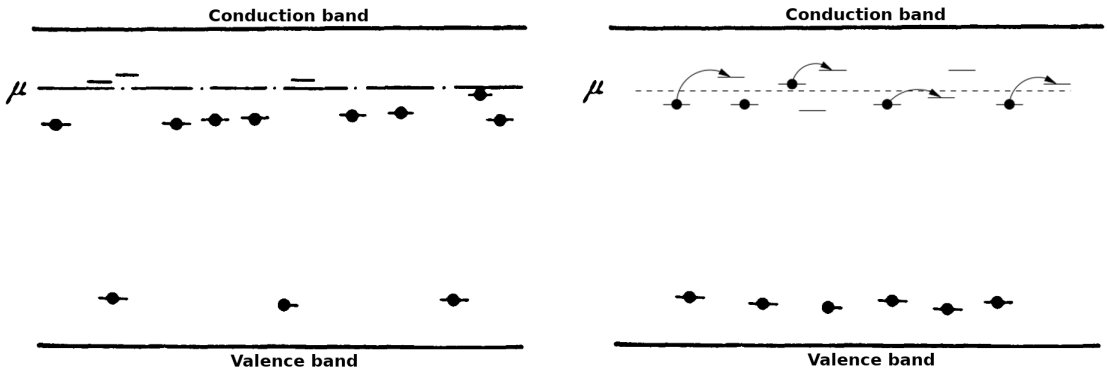

(a) (b)

Figure 2.3: (a) Energy levels in a compensated, lightly doped, semiconductor at $T = 0K$. Figure taken from [25] p. 57 with personal edits. (b) Conduction by hopping in presence of electric field. Part of figure taken from Ref. [27], combined with (a).

2.2 Introduction to percolation theory

In this section we give a brief, mostly phenomenological, introduction to percolation theory. This is to better the understanding of the methods used to derive the soon-to-be introduced *random resistor network*, and of the theoretical framework behind the theories of the VRH Hall effect. There are many percolation methods, and they are applicable to many different areas. For the problem at hand, *bond percolation* is directly useful.

The framework behind bond percolation is that two sites are *connected* if a bonding criteria is met. In terms of hopping conduction it means that electrons are able to jump from site to another at a given temperature and electric field. The temperature and field are replaced with a dimensionless percolation parameter ξ. For a low ξ, very few sites will be connected. Increasing ξ connects more and more sites. Connected sites form a *network* of paths through which electrons are able to pass. A sample will contain many such networks, but we are interested in is a network that will go from one edge of a sample to the other. Such a network will be able to produce conductivity. At some critical $\xi = \xi_C$, such a network will arise. We call this the percolating or infinite network. The value of ξ_C varies between samples, and if the sample size is small then ξ_C will fluctuate. As sample size increases the value of ξ_C between samples will quickly converge to some universal value that holds for infinitely large samples.

The situation looks like Fig. 2.4. Unconnected sites are not shown in the figure. Consider the

sample only within the large dashed box. The networks outside are the hypothetical case if the box was bigger. The requirement for percolation is a network connecting the left and right sides of the box. Bonds that are necessary for percolation to happen are called *singly connected bonds* (red). If one such bond is removed, percolation breaks. Bonds that are not vital, but used to percolate, are called the *backbone* (green). One or more bonds can be removed from the backbone without breaking percolation. The rest of the infinite cluster consists of *dangling ends* (blue). These are parts of the cluster that don't lead to percolation and can be safely removed. In reality the vast amount of bonds in the percolating network are dangling ends. The density of singly connected bonds is vastly over-exaggerated in Fig. 2.4.

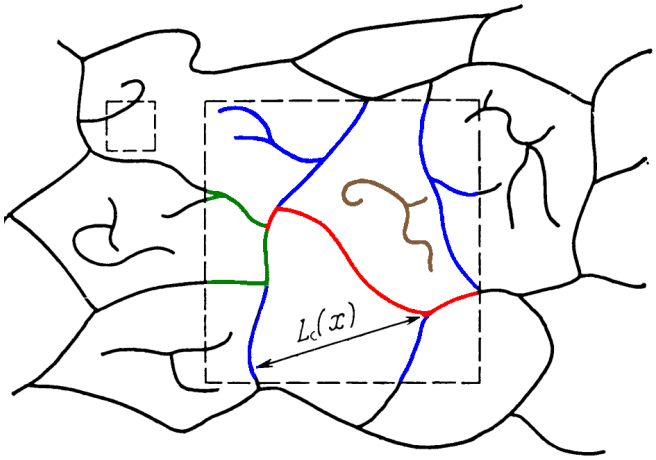

Figure 2.4: An example of networks generated by percolation methods. Connected sites are connected through solid lines. The scale is large such that lattice structure is not visible. $L_C(x)$ denotes the correlation length as function of the percolation parameter (ξ used in text). Color scheme illustrates parts of the infinite network for the sample only inside the large dashed box. Figure taken from [25] p. 97 with colors added personally. Red - singly connected bonds. Green - backbone. Blue - dangling ends. Brown - finite network.

Consider simulations of bond-percolation in a finite 2D sample of quadratic size with edges of length L. Each site in the sample has some random number x to be used for the bonding criteria. The aim of the simulations is to find the critical ξ_C that will produce a spanning network on the sample. Values of ξ are chosen one at a time, forming networks of bonds allowed by ξ, until a spanning network is detected. The value of ξ will now be ξ_C. Two different size samples with networks made using the *same* value of ξ can be seen in Fig. 2.4 inside the striped lines. The large sample features a spanning network, whereas the small sample does not. The small sample is too small to "see" the infinite network. Here it becomes useful to introduce the *correlation length* $L_C \sim$ the typical size of a not-percolating network. If the $L < L_C$, then there will be large *mesoscopic* effects, the properties of the sample will vary heavily depending on the configuration of sites in the sample. If $L > L_C$, then these effects are avoided.

2.3 Variable range hopping (VRH)

First described in 1969 by Mott [28], VRH is the behavior of the lowest temperature region in the compensated semiconductor. It has the unusual effect of having the important jump lengths increase as the temperature decreases. There are "regimes" in VRH, Mott and Efros-Shklovskii (ES). The ES regime considers long range Coulomb interaction between donor electrons. This

is neglected in the Mott regime. Both consider the disorder potential ϕ described in section 2.1.1. We will soon see that the important difference between the regimes is in the density of states.

As previously mentioned, hopping only happens in compensated semiconductors if there are more donors than acceptors, or opposite. Consider the case of more donor and acceptor impurities. All the acceptors are occupied with an electron for the temperatures considered. The acceptors are regarded to be completely static and are regarded as the background of the platform of donor sites on which VRH happens. The energy of the state at donor site i is

$$\epsilon_i = \phi_i + \sum_{i \neq j} \frac{(n_i - \nu)(n_j - \nu)}{r_{ij}}, \tag{2.3}$$

where ϕ_i is the (random) deformation potential at site i, $n_i = 0, 1$ is the occupation number of site i, r_{ij} is the distance between sites i and j and $\nu = 1 - K$ is the number of electrons divided by the number of sites. ν can be considered as the average occupation number. Energy is expressed in units of the Coulomb interaction, e^2/κ. ϵ_i represents the energy required to remove or place an electron at site i, it is often referred to as the *single particle energy* (SPE). The last term in Eq. 2.3 accounts for the Coulomb interaction between donor sites in a background of acceptors, shifting the average charge. The SPE does not give the exact energy for every site in the system, but on average the SPE should be an accurate estimator for the site energy. To produce the Mott regime, the Coulomb interaction terms are simply removed from Eq. 2.3. The Hamiltonian of the entire system is

$$H = \sum_i \phi_i n_i + \frac{1}{2} \sum_{i, i \neq j} \frac{(n_i - \nu)(n_j - \nu)}{r_{ij}}. \tag{2.4}$$

The 1/2 factor in Eq. 2.4 is added such that Coulomb interactions are counted only once. Before looking at the derivation of conductivity in the VRH regime, we examine the *random resistor network* model proposed by Miller and Abraham's in 1960 [29].

2.3.1 Random resistor network

The aim of this section is to show that the problem of hopping conduction can be reduced to a random resistor network. Each jump an electron can perform, can be represented as having a resistance R_{ij} associated with that jump. We follow the explanation given in [25] pages 86-89 closely.

Miller and Abraham's begin with the derivation of the *jump rate* of electrons going from site i to j, Γ_{ij}, with the absorption/emission of an appropriate phonon. The derivation of Γ_{ij} will not be given in this text, it can be found in [25] pages 83-86. The result is

$$\Gamma_{ij} = \tau_0^{-1} \exp\left(-\frac{2r_{ji}}{a}\right) \eta(\Delta\epsilon_{ij}) f_i(1 - f_j), \tag{2.5}$$

where τ_0 is a unit of time related to phonon-relaxation timescales of order 10^{-12}s [25,30]. f_i is the average occupation number of site i, $\Delta\epsilon_{ij} = \epsilon_j - \epsilon_i$ and

$$\eta(\Delta\epsilon_{ij}) = \begin{cases} 1, & \Delta\epsilon_{ij} < 0 \\ \exp(-\Delta\epsilon_{ij}/T), & \Delta\epsilon_{ij} > 0 \end{cases} \tag{2.6}$$

is the probability of finding a phonon with the energy needed to perform jump $i \to j$. T represents the thermal energy, equal to Boltzmann's constant multiplied by the temperature. T is often simply referred to as the temperature in this thesis.

Next we look at the current between sites i and j. It is $j_{ij} = -e(\Gamma_{ij} - \Gamma_{ji})$. In the absence of an electric field there should be zero current. Turning on $\mathbf{E}$ will change f_i and ϵ_i to create a current. In the linear field approximation and direct comparison to Ohm's law, it is possible to show

$$j_{ij} = R_{ij}^{-1}\,(U_i - U_j) \quad \text{where} \quad R_{ij} = \frac{T}{e^2\Gamma_{ij}^0}, \tag{2.7}$$

where $U_i - U_j$ is the local voltage drop from site $i \to j$ and Γ_{ij}^0 is the jump rate without an external electric field.

The goal is now to study the resistance R_{ij}. Setting Eq. 2.6 for $\Delta\epsilon_{ij} > 0$ into Eq. 2.5, and that into the expression for R_{ij} yields

$$R_{ij} = \frac{T}{e^2\gamma_{ij}^0}\exp\left(\frac{2r_{ij}}{a} + \frac{\epsilon_{ij}}{T}\right) \propto T\exp(\xi_{ij}), \quad \xi_{ij} = \frac{2r_{ij}}{a} + \frac{\epsilon_{ij}}{T}. \tag{2.8}$$

This problem can be interpreted as a bond-percolation problem with ξ as the percolation parameter. The bonding criteria of sites i and j is

$$\frac{2r_{ij}}{a} + \frac{\epsilon_{ij}}{T} \leq \xi. \tag{2.9}$$

Increasing ξ will connect sites, creating networks through which electrons can travel. It is the infinite network that is of interest, this is the only network that will produce current. We are interested in finding the ξ_C that will produce an infinite network.

As ξ increases, more and more sites bond, at some ξ_C the last bonds are formed and the network will percolate through the sample. It is only the resistance of the largest resistor before percolation that is of interest. The resistance of the entire network is defined by the last resistance to be connected. The resistance of the sample is given by R

$$R \approx R_C = R_0\exp(\xi_C), \quad R_0 \propto T. \tag{2.10}$$

In normal materials, and in simulations, $\xi > \xi_C$ tends to be the case. What this means is that electrons travel down several different paths through the sample. Each path can be considered to have it's own resistance R_{path}. These paths are opened at some $\xi > \xi_C$, and so $R_{\text{path}} > R_C$. The approximation in Eq. 2.10 is exact if there is the one percolating path opened at $\xi = \xi_C$. This is clearly not the case, but as will be seen, Eq. 2.10 still proves to be an excellent approximation.

ξ_C needs to be calculated in order to find the full behavior of R. But first the density of states in the VRH system needs to be known.

2.3.2 Density of states

As mentioned earlier, there are two main regimes in VRH studies. Mott and ES. The ES regime considers long-range Coulomb interaction whereas the Mott regime does not. Experimental studies show some materials fall neatly into one or the other, and other materials fall somewhere between the two. The qualitative difference between the two regimes is the density of states.

Mott regime

The site energies in the Mott regime are determined entirely from the random potential ϕ. The potential is uniformly distributed, resulting in a flat DOS for the Mott regime.

Coulomb gap

Efros and Shklovskii [31] showed in 1975 that when Coulomb interactions between the donor electrons is considered, the DOS should vanish at the Fermi level in the limit $T \to 0K$. Consider a system at $T = 0K$. If there is a possible jump, then that jump has to net zero or negative energy to stay in or reach a ground state. The change in energy $\Delta\epsilon_{ij}$ has to be greater than or equal to zero. The change in energy associated with the jump $i \to j$ with respective site energies ϵ_i and ϵ_j (given by Eq. 2.3) is

$$\Delta\epsilon_{ij} = \epsilon_i - \epsilon_j - \frac{1}{r_{ij}} \geq 0 \quad \Rightarrow \quad r_{ij} > \frac{1}{|\epsilon_i - \epsilon_j|} \tag{2.11}$$

Setting the expression ≥ 0 is a requirement for being in the ground state at $T = 0K$ as thermal excitations are impossible. Setting the Fermi energy $\mu = 0$, the occupation number at $T = 0K$ is

$$n_i = \begin{cases} 0, & \epsilon_i > 0 \\ 1, & \epsilon_i < 0 \end{cases}. \tag{2.12}$$

Any possible jump must go from an occupied donor to an empty state. Eq. 2.12 sets the requirement that these states must be on different sites of the Fermi level. Consider two donor sites on opposite sides in the energy range $(-\epsilon/2, \epsilon/2)$. From Eq. 2.11 The minimum distance between the sites has to be $1/|\epsilon|$. The minimum concentration in d-dimensions is $n = 1/r^d \propto |\epsilon|^d$ and the density of states is

$$g(\epsilon) = \frac{\partial n}{\partial \epsilon} \propto |\epsilon|^{d-1}. \tag{2.13}$$

In the relation above we have set $\mu = 0$. Using a generic Fermi energy simply shifts the result $\epsilon \to (\epsilon - \mu)$. We can now use a completely general DOS

$$g(\epsilon) \propto |\epsilon - \mu|^n, \tag{2.14}$$

where $n = 0$ corresponds to the constant Mott DOS and $n = d - 1$ the Coulomb gap DOS.

2.3.3 Mott and Efros-Shklovskii's law

The solution to the random resistor network will now be derived. The conductivity of the random resistor follows the relation

$$\sigma \propto R^{-1}, \quad \sigma = \sigma_0 \exp(-\xi_C), \quad \sigma_0 \propto T^{-1} \tag{2.15}$$

The conductivity of the hopping type system can be studied as a bond percolation problem. Two sites are connected according to the bonding criteria Eq. 2.9. For a given ξ, the maximum values of r and ϵ allowed by the bonding criteria are

$$r_{max}(\xi) = \frac{a\xi}{2} \text{ and } \epsilon_{max}(\xi)' = T\xi.$$

Percolation methods are often unable to predict values of numerical factors. We set the volume of a d-dimensional sphere to be $V(r) = v_d r^d$, v_d being the dimensional dependent numerical factors. Using the generic DOS, Eq. 2.14, the concentration of sites in the volume $V(r_{max})$, with energies less than ϵ_{max} is

$$n(\xi) = V(r_{max}^d) \int_{\mu-\epsilon_{max}(\xi)}^{\mu+\epsilon_{max}(\xi)} g(\epsilon)d\epsilon = \frac{g(\mu)v_d}{n+1}\epsilon_{max}^{n+1} r_{max}^d(\xi) = \frac{g(\mu)v_d}{2^d(n+1)}(kT)^{n+1}a^d\xi^{d+n+1} \tag{2.16}$$

where $g(\mu)$ is the density of states at the Fermi level. Setting $n(\xi_C) = n_C$, and solving Eq. 2.16 for ξ gives

$$\xi_C = \left(\frac{2^d(n+1)n_C}{g(\mu)v_d T^{n+1}a^d}\right)^{\frac{1}{d+n+1}} = \left(\frac{T_0}{T}\right)^{\frac{n+1}{d+n+1}}, \quad T_0 = \left(\frac{2^d(n+1)n_C}{g(\mu)v_d a^d}\right)^{\frac{1}{n+1}} = \left(\frac{C_0}{a^d}\right)^{\frac{1}{n+1}}.$$

T_0 is often referred to as the temperature constant, even though it depends on a. The numerical factors in T_0 are grouped into some constant C_0. The value of C also depends on dimensionality and the VRH regime. In the Mott regime it additionally depends on the value of the density of states at the Fermi level. Using self-consistent type of percolation approach, the results in two dimensions are $C_{\text{Mott}} = 13.8/g(\mu)$ in the Mott regime and $C_{\text{ES}} = 6.5$ in the ES regime [25, 32].

Setting ξ_C into Eq. 2.15 gives the conductivity

$$\sigma = \sigma_0 \exp\left(-\left(\frac{T_0}{T}\right)^p\right), \quad p = \frac{n+1}{d+n+1} \tag{2.17}$$

Mott's law is found by setting $n = 0$, in 2-dimensions $p = 1/3$. Efros-Shklovskii's law is found by setting $n = d - 1$. In any dimension the law is $p = 1/2$. Finally they are

$$\sigma_{\text{Mott}} = \sigma_0 \exp\left(-\left(\frac{T_{\text{Mott}}}{T}\right)^{1/3}\right) \quad \text{and} \quad \sigma_{\text{ES}} = \sigma_0 \exp\left(-\left(\frac{T_{\text{ES}}}{T}\right)^{1/2}\right),$$

where $T_{\text{Mott}} = C_{\text{Mott}}/a^2$ and $T_{\text{ES}} = C_{\text{ES}}/a$. Continuing forwards, T_0 with subscript 0 will be used to refer to both the Mott or ES regime.

2.3.4 Validity and difficulties with VRH laws

The two laws have their own areas of applicability. In some materials the long range Coulomb interactions are not significant to the hopping dynamics and follow Mott's law very neatly. Other materials follow the Efros-Shklovskii law closely. And yet some materials lie somewhere between the two.

Below is a description of the methods used to test measured data against the VRH conductivity laws.

Linearity test

One way to test if measured conductivity follows Eq. 2.17 for some values of p is to plot the data in a fashion that is expected to be linear. In Eq. 2.17, $\sigma_0 \propto T^{-1}$. Multiplying both sides of Eq. 2.17 with T, then taking the logarithm gives

$$\ln(\sigma T) = -T_0^p T^{-p} + \ln(A), \tag{2.18}$$

where $A = \sigma_0 T$ is a temperature independent numerical factor. If a material follows the VRH law, then a plot of measured $\ln(\sigma T)$ versus T^{-p} should result in a straight line according to Eq. 2.18. This method requires an input of p. A great difficulty is however that the linearity does not change much between $p = 1/3$ and $p = 1/2$. It is often difficult to determine what value of p best linearizes the conductivity.

Data collapse

The reason it's often difficult to determine if $p = 1/3$ or $p = 1/2$ best linearizes the data is that the temperature range is not wide enough. Simulating at lower temperatures takes a long time and results can have large uncertainty. In simulations this issue can be bypassed by comparing the results from using different localization lengths a. T_0 depends on a, meaning different localization lengths will cover different (T_0/T). If the data is instead plotted as function of $(T_0/T)^p$ then the data from the different a should lie on the same line if it follows the law. This is what we call a data collapse.

We have also found $T_{\text{Mott}} \propto a^{-2}$ and $T_{\text{ES}} \propto a^{-1}$. The exponent of a that best produces a data collapse can therefore also be used to help determine what law the data follows.

Hill's method

The above detailed method of determining the conductivities behavior requires us to input an expected value of p, and then check how well it fits. There is another method by Hill [33] that seeks to measure what the value of p should be. The idea is to compare the activation energy with the temperature in a log-log plot. The activation energy ϵ_3 comes from the definition

$$\sigma = \sigma_0 \exp\left(-\frac{\epsilon_3}{T}\right) \tag{2.19}$$

Solving ϵ_3 from Eq. 2.19 gives

$$\epsilon_3 = -T \ln\left(\frac{\sigma}{\sigma_0}\right) = -T \ln(\sigma T)$$

where in the last step we have used $\sigma_0 \propto T^{-1}$ from Eq. 2.10. Another way to solve for ϵ_3 is to take the logarithm of Eq. 2.19 which gives

$$\ln(\sigma) = \ln(\sigma_0) - \frac{\epsilon_3}{T} \Rightarrow \epsilon_3 = -\frac{\partial \ln(\sigma)}{\partial 1/T} + T \tag{2.20}$$

Setting Eq. 2.17 in as σ into the last part of Eq. 2.20 returns

$$\epsilon_3 = p T_0^p T^{1-p}$$

Plotting $\epsilon_3 = -T \ln(\sigma T)$ vs T in a log-log plot should return a straight line with slope $(1 - p)$. The gradient of the measured line can then be used to find the value of p from the data. The measured exponent p can then be compared with the theoretical VRH exponents 1/2 and 1/3.

VRH laws in real materials

There are advantages and disadvantages in the different approaches to determining p. The linearity test doesn't make any assumptions about the relative size of input parameters, but it

is difficult to determine what p gives the best linearization. Hill's method on the other hand makes assumptions about the size of $\ln(A)$, but gives one result for the p it predicts to give the best fit.

Analyzing experimental results using Hill's method finds p to take values between 0.18 and 0.70 [25, 33, 34], but most most amorphous follow Mott's law (in 3-dimensions) closely with $p \approx 0.25$ and most crystalline semiconductors follow ES's law with $p \approx 0.50$.

Amorphous materials experience Coulomb interactions between it's components. So why doesn't it follow the ES law? The answer is that the magnitude of variations in the deformation potential is much stronger than that of the Coulomb interactions. Amorphous semiconductors tend to have a constant DOS, with no Coulomb gap. There are dips close to ϵ_F caused by the Coulomb interaction, but they are small compared to the $g(\epsilon)$. The insignificant Coulomb gap makes the material follow Mott's law, even when there are Coulomb interactions between material constituents. The degree of amorphousness will impact the significance of the Coulomb gap, adjusting the p value between 0.25 and 0.5.

Some materials even exhibit both Mott and ES type conductivity depending on the temperature [4, 25]. At high temperatures the thermal fluctuations dominate and Coulomb interaction has minimal effect, leading to Mott type conductivity. At low temperatures the Coulomb interaction becomes important and the material's conductivity is closer to that of ES's law.

Note that in crystalline semiconductors it is only the intrinsic atoms that are positioned in a structured manner. The impurities are still placed in a disordered configuration. Meaning the positions used for hopping are in disorder, both for crystalline and amorphous semiconductors.

CHAPTER 3

Hall effect

The Hall effect is how current traveling through a material is affected when an external magnetic field is applied. It was E. H. Hall who discovered this effect in 1879 [35]. It has since been found to be an important tool used to investigate materials. Specifically the Hall effect can be used to determine the type of charge carrier in materials. Mainly there are two types of Hall effect, the ordinary and the anomalous. The anomalous Hall effect is when a magnetic material experiences a Hall effect without an external magnetic field due to internal magnetization. This project only concerns itself with the ordinary Hall effect.

3.1 Classical ordinary Hall effect

In classical terms it is explained by the Lorentz force $\mathbf{F} = q(\mathbf{E} + \mathbf{v} \times \mathbf{B})$. The electric field accelerates charges parallel or anti parallel the electric field. The magnetic component of the Lorentz force has direction perpendicular to the applied magnetic field and velocity of the charges. If the magnetic field has a component perpendicular to the charge velocity, moving charges will be deflected by the magnetic field, creating charge imbalances in the material. The Hall effect is different depending on what type of charge carrier is dominant in the material. Let us consider the cases separately.

Electrons as majority carrier

First consider the situation in Fig. 3.1a. There is an applied electric field pushing the electrons (white arrows) in the direction of $q\mathbf{E}$. The magnetic field is turned on in Fig. 3.1b. The direction of the magnetic force $q(\mathbf{v} \times \mathbf{H})$ will be $q^2(\mathbf{E} \times \mathbf{B})$, since the electric field is giving the electrons its velocity. In the figure, the electrons are moving down, causing a buildup of negative charges on bottom surface. The electric charges moving down, moves the positive holes up. So there are positive charges on the top surface. The charge difference produces a transverse electric field, E_y. The charge buildup on material boundaries continues until the force from E_y is balanced by the magnetic deflection. Then the system has reached a steady state as in Fig. 3.1c. The material posesses a charge difference in the transverse direction, but current travels through the material normally.

Holes as majority carrier

The process is very similar when holes replace electrons as majority carrier. The holes (black arrows in Fig. 3.1) are initially moving in the direction of the electric field. The holes have

opposite charge, and opposite velocity direction to the electrons. The combination results in particles being deflected in the *same* direction by the magnetic field. The deflection of the holes will push electrons in the opposite direction, causing a buildup of charge on opposite surfaces. The resultant field E_y will balance the magnetic force, creating a steady state situation. The polarization of the charge buildup is opposite for holes and electrons. The sign of E_y depends on the type of charges carriers in the material.

Real materials

The Hall effect is often characterized by the Hall coefficient $R_H \equiv E_y/(j_x B_z)$. We see that electrons and holes as majority carrier produces different signs for E_y and therefore have different signs for R_H. Real materials have both electrons and holes as charge carriers. The opposite charge carriers counteract each other. The combination of both charge carriers lowers the Hall effect.

If there is an equal number of holes and electrons, then the fields will cancel out and there is no classical Hall effect! As the sign of the Hall effect depends on the type of charge carrier, measurements of the effect can be used to determine the charge carrier of materials. Some specific materials still exhibit a Hall effect with equal number of holes and electrons, this is called the compensated Hall effect.

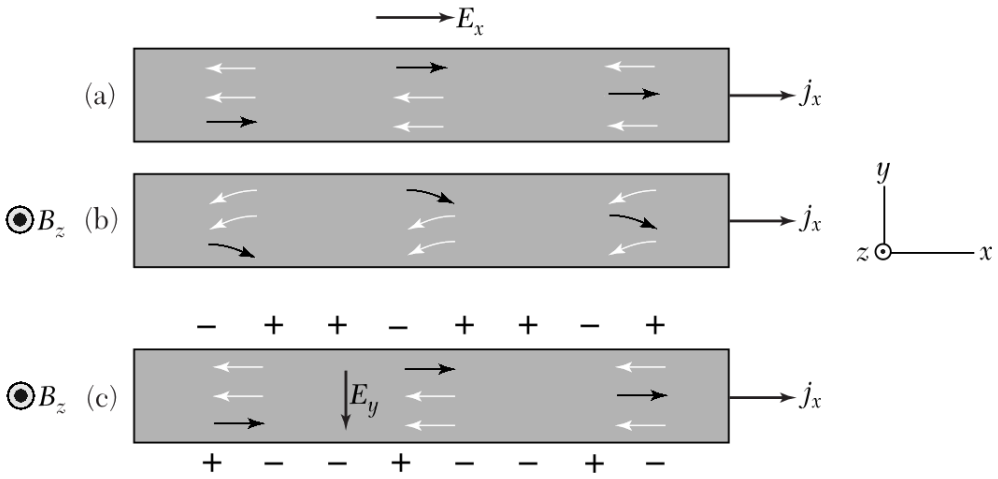

Figure 3.1: 3 stages of the classical ordinary Hall effect. White arrows represent electrons and black arrows represent holes. (a) Current flowing through the material when an electric field is applied. (b) The movement of the charges is deflected when the magnetic field is turned on. (c) The deflection causes a buildup of charges on opposite sides of the material, creating E_y to counteract the influence of B_z. In the final steady state situation, the current is moving just as it did in (a), without any magnetic field. Figure taken from [24] page 154 with personal edits.

3.2 VRH Hall effect

The effect is different in the VRH regime. The electrons travel by hopping discretely. There is no velocity on which the Lorentz force can act to cause a magnetic deflection. The Hall effect can be explained by including higher order electron transitions.

The jump rate between two sites, Eq. 2.5, is independent of **H** and is unchanged by magnetic fields. The resulting current is unaffected by a magnetic field. Holstein [5] considered jumps between two sites $i \to j$, in the direct presence of a third site k, and showed that such jumps create a magnetic field dependence. The third intermediate site allows the electron two paths to get from i to j. It can travel directly $i \to j$ or by stopping by the intermediate site $i \to k$ then $k \to j$. The process is illustrated on Fig. 3.2a. Holstein considered only jumps in which the intermediate site k was unoccupied. Shumilin [17] extended the model to include jumps in the presence of an occupied intermediate site. That process is illustrated in Fig. 3.2b. If k is occupied, then the electron on i cannot jump to k before the electron on k has jumped to i. The two processes when the intermediate site is occupied are $k \to j$ followed by $i \to k$, and the direct jump $i \to j$. The two processes are different because the electron on k ends up on j instead of the i electron for the intermediate path. Even so, the final states are indistinguishable and it makes no difference which electron went where.

It might be more natural to think of the jumps involving an occupied intermediate site as if the hole was performing the jump instead of electrons. The hole has two paths, $j \to k$ then $k \to i$, and $j \to i$.

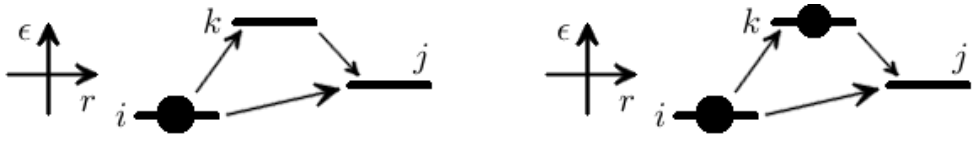

Figure 3.2: Jump paths from i to j in presence of available (a) and occupied (b) intermediate sites. The configuration of energy for the different sites in the figure is chosen arbitrarily.

The magnetic field impacts the system through the Aharanov-Bohm effect. The Aharanov-Bohm effect changes the wavefunction trough the gauge function

$$\chi \equiv \frac{e}{\hbar}\int_0^{\mathbf{r}} \mathbf{A}(\mathbf{r}) \cdot d\mathbf{r}$$

that changes the wavefunction $\psi(\mathbf{r}) \to e^{i\chi}\psi(\mathbf{r})$. $\mathbf{A}$ is the electromagnetic vector field. It is interference in the phase of the wavefunction between different paths from i to j that produces a magnetic field dependence in the rate equations. Holstein and Shumilin only consider effects *linear* in H. Using (n) to note the occupation number of site k, the magnetic field dependent rates are

$$\Gamma^{(0)}_{ikj} = \frac{1}{t_0\tau_1}\left(\frac{\mathbf{H}\cdot\mathbf{A}_{ikj}}{2\Phi_0}\right)\exp\left(-\frac{r_{ij}+r_{jk}+r_{ik}}{a}\right)\times \\ \left[\eta(\Delta\epsilon_{ij})\eta(\Delta\epsilon_{ik}) + \eta(\Delta\epsilon_{ij})\eta(\Delta\epsilon_{jk}) + \eta(\Delta\epsilon_{ik})\eta(\Delta\epsilon_{kj})\right] f_i(1-f_j)(1-f_k) \quad (3.1)$$

and

$$\Gamma^{(1)}_{ikj} = -\frac{1}{t_0\tau_1}\left(\frac{\mathbf{H}\cdot\mathbf{A}_{ikj}}{2\Phi_0}\right)\exp\left(-\frac{r_{ij}+r_{jk}+r_{ik}}{a}\right)\times \\ \left[\eta(\Delta\epsilon_{ki})\eta(\Delta\epsilon_{kj}) + \eta(\Delta\epsilon_{ij})\eta(\Delta\epsilon_{ki}) + \eta(\Delta\epsilon_{ij})\eta(\Delta\epsilon_{kj})\right] f_i f_k(1-f_j). \quad (3.2)$$

where $\mathbf{H}$ is the applied magnetic field, $\mathbf{A}_{ikj}$ is the vector area of the triangle with vertices at sites ikj, $\Phi_0 = h/2e$ is the magnetic flux quanta, t_0 and τ_1 are phonon relaxation timescales and $\eta(\Delta\epsilon_{ij})$ is defined by Eq. 2.6. The definition of the vector area determines how specific jump configurations become more or less frequent as the magnetic field increases. The sign difference in front of the area between $\Gamma^{(0)}_{ikj}$ and $\Gamma^{(1)}_{ikj}$ mean that electrons and holes effectively favor different configurations when a magnetic field is present. The reason there is a sign difference can be interpreted as coming from the charge difference. The product $\mathbf{H}\cdot\mathbf{A}_{ikj}/\Phi_0$ is the magnetic flux through the field perpendicular area component A_{ikj}.

The rate equations $\Gamma^{(n)}_{ikj}$ are only the magnetic field correction to the total rate of jumps. The total rate of jumps from $i \to j$ is

$$\Gamma^{\text{total}}_{ij} = \Gamma_{ij} + \sum_k (\Gamma^{(1)}_{ikj} + \Gamma^{(0)}_{ikj}). \tag{3.3}$$

As mentioned the rate equations only consider linear magnetic field effects. Effects such as magnetoresistance are not considered. Magnetoresistance is the effect of decreasing conductivity with increasing magnetic field. It is explained by a squeezing of the electron orbitals, decreasing the overlap between neighboring sites.

3.2.1 Explanation of VRH Hall effect

It is not trivial to see that Eqs. 3.1 and Eq. 3.2 will produce a Hall effect. The magnetic field will increase the rate to some sites, and decrease it to others. The favorable direction is determined by the definition of the vector area $\mathbf{A}_{ikj}$. The decision was made to set *counterclockwise* areas to be positive. As will be seen, this results in a *negative* sign of the Hall effect.

Let us consider only *available* intermediate sites first. For simplicity and convenience, the correction jump rate is split into into magnetic field and electric field components. These are referred to as transition rates and acceptance rates, as indicated by their respective subscripts T and A, and will be discussed more in the methods chapter. Eq. 3.1 becomes $\Gamma^{(0)}_{ikj} = \Gamma^{(0)T}_{ikj}(\mathbf{H})\Gamma^{(0)A}_{ikj}(\mathbf{E})$, where the transition and acceptance rates are defined as

$$\Gamma^{(0)T}_{ikj}(\mathbf{H}) = \frac{1}{t_0\tau_1}\left(\frac{\mathbf{H}\cdot\mathbf{A}_{ikj}}{2\Phi_0}\right)\exp\left(-\frac{r_{ij}+r_{jk}+r_{ik}}{a}\right)$$
$$\Gamma^{(0)A}_{ikj}(\mathbf{E}) = \left[\eta(\Delta\epsilon_{ij})\eta(\Delta\epsilon_{ik}) + \eta(\Delta\epsilon_{ij})\eta(\Delta\epsilon_{jk}) + \eta(\Delta\epsilon_{ik})\eta(\Delta\epsilon_{kj})\right] f_i(1-f_j)(1-f_k),$$

The effect of the transition rate is to increase the rate of jumps with positive areas and reduce the jumps with negative areas. The transition rate reduces exponentially with distance, and increases linearly with area, making short jumps most notable. From symmetry arguments it is clear that $\sum_k \Gamma^{(0)T}_{ikj}(\mathbf{H})$ is independent of $\mathbf{H}$ due to pairing of areas with opposite signs. Neither the transition nor the acceptance rates alone can explain the Hall effect. The combination of $\mathbf{E}$ and $\mathbf{H}$ is necessary.

The acceptance rate is a bit more complicated to work with due to the random site energy ϵ_i. Consider a simplified case in which all the site potentials are equal. In this case, $\eta(\Delta\epsilon_{ij})$ is 1 for any jump in the direction opposite $\mathbf{E}$ and is exponentially decreasing with distance going with $\mathbf{E}$.

The simplified system is considered in Fig. 3.3. There is one electron at the center site and all the other sites are unoccupied. All the site potentials are equal. Electric and magnetic field are set to 1. We only consider the *change* in Eq. 3.1 when a magnetic field is added. As jump rates decrease exponentially with distance, this system only considers nearest neighbors as intermediate sites. And we only calculate transitions ending up at the *corners* sites. Each corner has two intermediate sites leading there, the two transitions having different orientation and the vector areas of the respective transitions have different sign. The signs are highlighted by color in Fig. 3.3, blue for negative and red for positive.

$\Delta_H\left(\sum_k \Gamma^{(0)}_{ikj}\right)$ in Fig. 3.3 denotes the change in jump rate going from the center to the a corner, when the magnetic field is turned on. The radial exponential dependence of $\Gamma^{(0)T}_{ikj}$ has been omitted from $\Delta_H\left(\sum_k \Gamma^{(0)}_{ikj}\right)$ for visual purposes. The configuration of distances are equal for all the points, and therefore only results in a constant factor. We are primarily interested in the jump going against the electric field, as those happen most frequently. $\Delta_H\left(\sum_k \Gamma^{(0)}_{ikj}\right)$ is *positive* going to the bottom left corner, and *negative* going to the top left one. This means that when the magnetic field is turned on, more electrons will jump down-left than up-left.

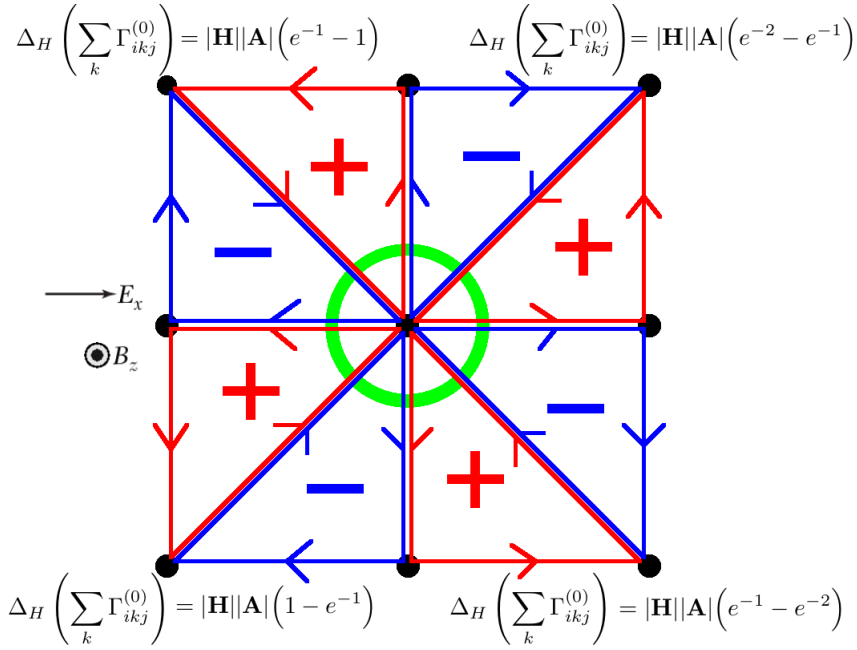

Figure 3.3: Change in jump rate going from center site to corner sites when no other sites are occupied. Red (blue) color denotes areas aligned with (against) the magnetic field. The green circle is the occupied electron state.

Effectively what happens is that going to the bottom left site, positive areas pair up with large phonon probabilities. And negative areas pair up with smaller phonon probabilities. The sum is net positive. Oppositely, large phonon probabilities pair up with negative areas and small phonon probabilities with positive areas when going up left.

This means electrons will be deflected from the going up and left, to going down and left when the magnetic field is turned on. This effect is expected to last when considering variable site

potentials ϵ. The resultant Hall effect for electrons should have *negative* sign.

If the intermediate site is occupied, then the jumps effectively use opposite sign for the vector area A_{ikj}. Naively one might think that the $\Gamma^{(1)}_{ikj}$ will change oppositely to $\Gamma^{(0)}_{ikj}$. However, the phonon averaging for occupied jumps change the transitions that give large contributions. The resultant $\Delta_H\left(\sum_k \Gamma^{(1)}_{ikj}\right)$ are identical to $\Delta_H\left(\sum_k \Gamma^{(0)}_{ikj}\right)$. Therefore holes are expected to produce the same Hall sign as electrons using this model.

3.2.2 Sign of VRH Hall effect

From the calculations in the previous section it appears electrons and holes produce Hall effect with the same sign. Holstein [36] showed that the sign of the VRH Hall effect does not depend solely on the charge carrier, but also on the type of jump responsible for the Hall effect. In this context, he considered jumps involving n sites, and found

$$\text{sign}(R_H) = \text{sign}\left(q^{n+1}\prod_{i=1}^{n} J_{i,j+1}\right), \tag{3.4}$$

where $q = \mp 1$ is the opposite charge of the assumed charge carrier, and $J_{i,i+1}$ is the *transfer integral* between sites i and $i+1$. The RHS of Eq. 3.4 is the product of transfer integrals going around the structure of the n site jump. If $n = 3$, then it is the product of transfer integrals going around the triangle. Site $n+1$ is defined to be site 1 to make transfer integrals go in a loop.

The sign of the transfer integral between i and j is opposite for electrons and holes [36], $J^{(h)}_{ij}(H) = -J^{(e)}_{ij}(H)$. The resultant sign of $\prod_{i=1}^{n} J_{i,j+1}$ is then the *same* for electrons and holes when n is odd-numbered, and *different* when n is even. As the Cage changes from electrons to holes, it means the sign of the Hall effect produced by n site jumps is independent of charge carrier for odd n and changes for even n. Therefore, when considering jumps involving three sites, electrons and holes should produce the same sign. Jumps involving four sites should produce different Hall effect signs.

Measurements of the thermoelectric effect can typically be used to determine the charge carriers of a material, just as the Hall effect traditionally. In many amorphous semiconductors, the Hall effect experiences no sign change while the thermopower does. [37,38]. The Hall effect anomaly is explained by Eq. 3.4 if the main contribution comes from odd-numbered loops. While the structure of amorphous materials is disordered, it is believed to contain many odd-numbered loops [39]. Hence the experimental measurements are in agreement with Eq. 3.4.

Experimental results of n-type amorphous Si films find the thermopower sign to be electron-like and the Hall effect sign to be hole-like. The thermopower sign is measured to be hole-like in p-type amorphous Si films, while the Hall effect sign is electron-like [38]. The electrons in amorphous Si films are believed to be of anti-bonding orbital type in the conduction band, and holes to be bonding orbital type in the valence band. The band and the different orbital structure changes the transfer integrals entering Eq. 3.4. For odd-numbered loops anti-bonding holes and bonding electrons should produce different Hall signs [39], in agreement with the results.

In conclusion, the sign of the Hall effect should not depend solely on the charge carrier, but also on the local geometry and type of wavefunction for charge carrying particles. For our simulations we will only consider hydrogen-like wavefunctions, and jumps involving only two or three sites. Thus we expect the sign to be the same for electrons and holes.

3.2.3 Theoretical approaches to VRH Hall

There are multiple theoretical solutions to the VRH Hall conductivity [6, 7, 9, 40–45]. Most theories rely on percolation arguments to calculate the VRH Hall mobility. Using similar methods, they result in slightly different results. Below is a description of the methods and argumentation behind these theories.

The main idea is to consider current traveling through the percolating network, and see how the magnetic field correction affects that current. Fig. 3.4a shows a percolating network with junctions highlighted with circles. The principle idea is that the magnetic field corrections are only important at the junctions of the percolating network. When an external magnetic field is present, Eqs. 3.1 and 3.2 should redirect some current from one site to another. This results in a favorable direction when there is a magnetic field, and the Hall effect is generated.

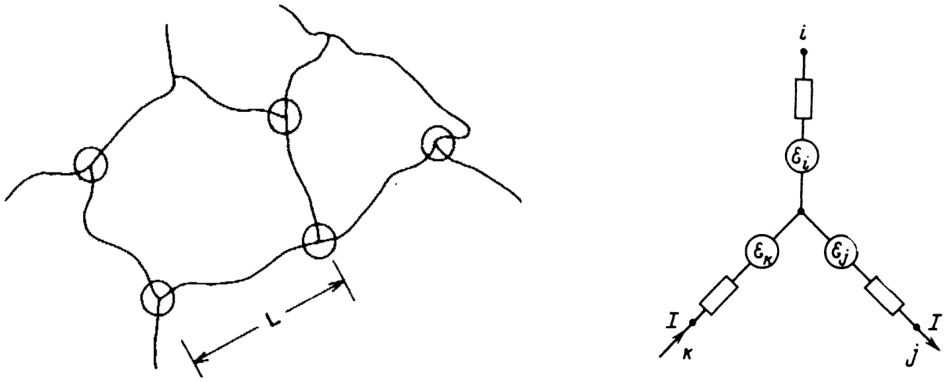

(a) (b)

Figure 3.4: (a) Junctions in percolating network. L denotes the correlation length, L_C used in text. Figure taken from [46]. (b) Optimal position of sites at junction in percolating network. Taken from [7].

With this framework, the configuration of sites at the junctions become important in determining the magnetic properties of the network. The three sites at the junction might not be good generators of Hall current depending on the configuration of site potentials ϵ and the intersite distances. Therefore it is expected that the average distance between effective Hall generators at junctions is *larger* than the correlation length of the percolating network. The Hall current should have a correlation length larger than that of the longitudinal current. This implies the Hall current is more susceptible to mesoscopic effects than the longitudinal current.

The authors of Ref. [41] find that the main contribution to the Hall effect should come from equilateral triangles formed by sites in the clusters. Such triangles should generate much more Hall current than other triangles.

Galperin et al. [7] develop the theory of optimal triangles for the Hall conductivity. They find that the Hall conductivity is dominated by some specific configurations of site potentials and intersite distances. Such a configuration can be referred to as an optimal triangle and is illustrated in Fig. 3.4b. An optimal triangle is described by several requirements. The resistances between the sites must all be of the order of the critical percolating resistance $R_{ij} \approx R_{ik} \approx R_{jk} \approx R_C$. The site potentials $\epsilon_i, \epsilon_k, \epsilon_j$ all need to be on one side of the Fermi energy. Two of them need to be within T of some ϵ_{max}. The sites all need to be as close as possible, $r_{ij} \approx r_{ij} \approx r_{kj} \approx r_{ik} \approx r_{\min}$. The minimum distance $r_{\min}$ is defined from intersite quantum repulsion. $\epsilon_{\max}$ is the maximum energy defined by the bonding criteria Eq. 2.9 when the intersite distance is $r_{\min}$.

Using P^3 as the probability of finding an optimal triangle, the correlation length of the Hall conductivity is defined by $L_H \approx L_C/P$. The result from [7] gives

$$L_H \approx L_C \left[\frac{\xi_C^2}{\ln(V/T\xi_c)} \right]^4 .$$

Using typical values, L_H can be $10^2 - 10^3$ times larger than L_C. In a real material it can be $\sim$ some millimeters. The drastically larger correlation predicts mesoscopic fluctuations from sample to sample depending on if or how many optimal triangles there are.

Most works find the Hall mobility to be on the form of

$$\mu_H \equiv \frac{\sigma_H}{\sigma_x H} \propto \frac{a^\gamma}{T^{\lambda-1}} \exp\left(-\alpha \left(\frac{T_0}{T}\right)^p\right), \tag{3.5}$$

where α, γ and λ are constants. The implication of Eq. 3.5 is that $\sigma_H \propto H a^\gamma T^{-\lambda} \exp(-(1+\alpha)(T_0/T)^p)$.

The exact value of α is in dispute between the theoretical predictions. The value of α can be interpreted as the Hall mobility having a different T_0 than the normal mobility. α is expected to vary with applied magnetic field, the reported values are the zero-field extrapolated value. The results are gathered in table 3.1. With the exception of Burkov *et al.* [44], the results predict an $\alpha < 1$.

Table 3.1: Values of α and λ for different theories. *Németh and Mühslchlegel find Mott regime α to depend on dimensionality. $\alpha = 0.310$ for 2d and $\alpha = 0.355$ in 3d.

Author	α_{Mott}	λ_{Mott}	γ_{Mott}	α_{ES}	λ_{ES}	γ_{ES}
Gruenewald *et al.* 1981 [6]	0.375	-	-	-	-	-
Friedman 1982 [42]	-	-	-	0.2247	1	-
Németh and Mühslchlegel 1988 [9]	0.355,0.310*	0.5	0.5	0.2247	1	1
Burkov *et al.* 2003 [44]	2	1	2	-	-	-
Arsenault 2008 [45]	0.375	-	-	-	-	-

Table 3.2: Experimental results for VRH Hall effect. The value of λ is the one that fitted measurements best. *α value interpreted in Ref. [9]. **Roy et al. found longitudinal conductivity to follow Mott's law, but found that both 1/2 and 1/4 fitted for the Hall mobility. They saw no clear behavior for α as function of applied field and were unable to extrapolate a zero field value. ***Qiao *et al.* varied oxygen pressure to control electron density. The two values reported are for two different densities. Qiao's et al.'s α parameter is reported at finite field.

Author	Material	Regime	α	λ
Koon and Castner 1987 [10]	SiAs	Mott	0.37 ± 0.02	0
Rhode and Micklitz 1987 [47]*	Bi_xKr_{1-x}	-	0.28 ± 0.05	-
Roy et al. 1989 [11]	n-type CdSe	Mott or ES**	< 0.7	0
Zhang *et al.* 1993 [12]	CdSe	-	0.46 ± 0.04	-
Essaleh et al 2006 [48]	n-type $CuInSe_2$	Mott	-	0
Qiao *et al.* 2014 [13]	$In_{0.27}Co_{0.73})_2O_{3-v}$	Mott	0.82	0
Qiao *et al.* 2014 [13]	$In_{0.27}Co_{0.73})_2O_{3-v}$	ES	0.31,0.39***	0
Kajikawa 2017 [14]	Si doped n-type GaN	ES	0.3	1
Stepina 2018 [17]	Ge/Si quantum dots	ES	0.56	0

The result from the theory of optimal triangles [7] is

$$\mu_H \propto \frac{a^2}{T}\xi_C \left[\frac{\ln(V/T\xi_C)}{\xi_C}\right]^4. \tag{3.6}$$

The main result of Friedman and Pollak [43] is

$$\mu_H \propto a^2 \left(\frac{T}{T_0}\right)^{13/4} \left[b + cf_1\left(\frac{T}{T_0}\right)^{1/4} + df_2\left(\frac{T}{T_0}\right)^{1/2} + ef_3\left(\frac{T}{T_0}\right)^{3/4}\right], \tag{3.7}$$

where f_n are numerical factors expressed as incomplete Gamma functions. Despite very different function forms between Eqs. 3.7, 3.6 and 3.4, numerical estimates show they are identical to exponential precision to $\alpha_{\text{Mott}} = 0.375$ [7, 43].

The reason σ_H has a larger T_0 than σ_x can be intuitively explained through the larger correlation length. The increased L_H implies a critical percolating concentration n_C, such that the numerical factor β should be larger. This argument is not perfect as it is difficult to define what percolation means for σ_H.

3.2.4 Experimental results of VRH Hall effect

The purpose of this subsection is to give an overview of experimental results of the VRH hall effect. There are more published experimental studies, but there are too many to include here. Some of the results are presented in text, all are gathered in table 3.2.

The first prediction of an impurity conduction Hall effect was made by Holstein in 1961 [5]. His prediction included an estimate that the Hall effect should be anomalously large. Amitay and Pollak were unable to measure any Hall effect in 1966 [49]. The negative result was attributed to a requirement for more sensitive instruments. In 1985 Klein was also unable to measure anything [50].

The first experimental results of the VRH Hall effect are from 1987 by Koon *et al.* [10]. They measured the Hall coefficient in SiAs for temperatures approximately between $0.5K - 4$K and find α in good agreement with [6] theoretical prediction. They find the value of α to depend on applied magnetic field, but extrapolate to the zero field value at the critical percolating concentration for their final α. Their measurements are made using magnetic fields between 1 T and 15 T.

Roy et al. [11] find difficulty extrapolating the zero-field value of α. Their measurements are made using magnetic fields $0.3 - 1.0$ T. They report a larger α than [10] for the fields used, and that α may tend to one.

Rhode and Micklitz [47] measured σ_H in Bi_xKr_{1-x} but do not make attempts to measure α from their data. Instead they measure the relation $\sigma_H \propto \sigma_x^{1.28\pm0.05}$. The authors of Ref. [9] imply $\sigma_H \propto \sigma_x^{1+\alpha}$ and interpret the result from [47] as $\alpha = 0.28 \pm 0.05$. Zhang et al. [12] instead find the empirical relation $\sigma_H \propto \sigma_x^{2-\alpha}$ and measure $\alpha = 0.46 \pm 0.04$ in CdSe. Note that if $\sigma_H \propto \sigma_x^{2-\alpha}$ then the only possibility is $\alpha = 0.5$.

Zhang et al. also find α to be constant for $B > 3T$, in disagreement with results from Ref. [10]. Zhang et al. perform their measurements on the same material as Roy et al. do in [11], commenting that Roy et al.'s inability to find a definite α results from using magnetic fields lower than 1 T.

Qiao et al. measure measure the Hall effect in $(In_{0.27}Co_{0.73})_2O_{3-v}$ and vary the O_2 partial pressure to reproduce both ES and Mott regime conductivity. They find $\alpha_{\mathrm{ES}} > \alpha_{\mathrm{Mott}}$, but do not extrapolate α values to zero-field.

All experimental results in table 3.2 measure $\alpha < 1$ and most measure $0.3 < \alpha < 0.5$ independent of conduction regime. The results are not far off some of the theoretical predictions. With the exception of Kajikawa's result [14], all the experimental work favors $\lambda = 0$. It should be noted that it is difficult to determine the value of λ without having a data over a significant temperature range.

3.2.5 Previous VRH Hall effect simulations

The first simulations of VRH Hall effect are from 1981 by P. N. Butcher et al. [15, 16]. They used percolation methods to solve Kirchhoff's equations to produce a result for the Hall mobility. An outline of percolation simulation methods is found at the end of the methods chapter. As function of density, the simulations reported agreement with [40] for high density [15]. As for the temperature behavior, they report μ_H on the form of Eq. 3.5 with $\lambda = 0$, but no measurements of α were made [16].

P. N. Butcher et al.'s results were produced using 13x13x13 sites with only one configuration of disorder potentials. The predicted large correlation length of the Hall mobility is likely bigger than the simulated system. As such, larger samples and more configurations are important for making the results trustworthy.

Shumilin and Stepina have used similar methods to simulate the VRH Hall effect, using 100x100 sites in 2-dimensions for multiple disorder configurations [17]. The results follow Eq. 3.5 with

$\alpha_{\text{Mott}} = 0.46$ and $\alpha_{\text{ES}} = 0.3$ and $\mu_H \propto a^2$ for both regimes. The ES regime is simulated in Ref. [17] by performing a zero-temperature MC algorithm to produce a Coulomb gap, then applying percolation algorithms to effectively simulate dynamics using static Coulomb interactions.

CHAPTER 4

Methods

The main goal of this project is to measure the conductivity in the x and y-directions as functions of various parameters. This chapter mainly deals with the Kinetic Monte Carlo algorithms, and how the simulations are performed. First the system on which the alorithms act is described. Then the algorithms themselves are detailed, and methods used for measuring conductivity from simulation data is explained. Finally a brief comparison between the Kinetic Monte Carlo and percolation algorithms is given.

4.1 System description

For our simulations we use sites located on an ordered lattice of dimensions $L \times L$. The sites represent the donor impurities in the lightly doped semiconductor. The disorder potential ϕ_i (see Eq. 2.3) is generated for each site as a uniformly distributed random number $\phi_i \in [-1, 1]$. The simulations take the percentage of sites to be filled with electrons as a parameter. This will be referred to as the fill fraction ν. The sites are randomly filled with electrons until the fill fraction is satisfied. An example lattice is displayed in Fig. 4.1. This is the platform on which the simulations are done. The site locations in real materials also feature positional disorder. This is not accounted for by the lattice model, but is not expected to cause big problems [32, 51]. The lattice model is chosen for its computational effectivity and low memory usage. The boundaries are periodic.

The simulations are initialized with a constant temperature, electric and magnetic field. The sites are thermally connected to a heat bath of constant temperature. Phonons are absorbed and emitted from/into this heat bath. It is assumed to be large such that the temperature is constant.

The requirement for a semiconductor to be defined as lightly doped is $Na^d \ll 1$, N being the concentration of doped impurities. The localization length is very small, and the wavefunction overlap is a exponentially small. This means that jumps happen very infrequently. Using realistic localization lengths in simulations would lead to impossibly long computation times. This project uses localization lengths between 0.2 and 1 times the donor spacing.

The initial state is a randomly generated configuration of occupied and non-occupied states. The KMC algorithm is used for time evolution. The initial state is likely a very unlikely configuration for the system to naturally find itself in, because high energy states are just as likely to be occupied as low energy states. The system uses some configuration time to

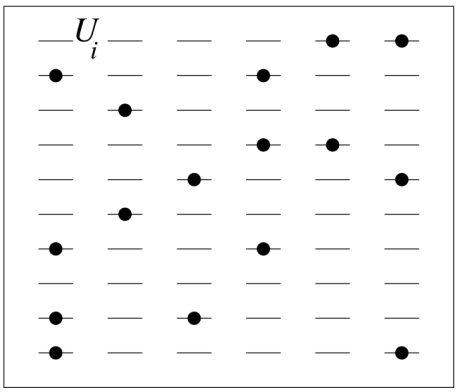

Figure 4.1: Image of the lattice model. Flat lines indicate states, with filled circles representing electrons occupying those states. U_i is the disorder potential (ϕ_i used in text). Figure taken from Ref. [27].

evolve to a more physical state. After the configuration time has passed, the system enters its steady state. The dynamics of the jumps happening after the configuration time is what we wish to study. Therefore the initial jumps needs to be omitted before analyzing the results. The number of jumps required to reach the steady state depends on simulation parameters such as temperature, electric field and localization length. In high temperature cases only the first hundred thousand or so need to be discarded, but a million might be needed at low temperature.

Both the Mott and ES regime can be studied using this model. The only difference is the range of the Coulomb interaction. The Coulomb cut-off range is set to be $L/2$. This prevents an electron from interacting with itself, but means some sites don't interact when they should. This interaction is so small, because those sites are so far away, that it is not significant. The Mott regime is simulated by setting the Coulomb cut-off to be less than site separation. This way no sites will have any interation with one another.

Energy is expressed in units of e^2/κ such that the Coulomb potential between neighboring sites is 1. This makes the Coulomb potential stronger than the disorder potential in ES regime simulations. The strength of the Coulomb interaction relative to the disorder potential is sufficient to produce the Coulomb gap in the density of states.

4.1.0.1 Randomly positioned sites

The theoretical work behind the random resistor network and the VRH laws use sites with random positional disorder. The lattice model is one that is used for it's efficiency, but it is useful to test the effects the lattice model has on conductivity. This can be done by performing a few simulations on samples of randomly distributed sites.

4.1.1 Limitations

The periodic bounary conditions employ a limitation in therms of the Hall effect. There cannot be a buildup of charges on the sides of the system. Therefore the transverse electric field E_y cannot be simulated and the steady state situation depicted in Fig. 3.1(c) cannot be reached. Instead we simulate scenario (b) in Fig. 3.1 and sample those properties. The term steady

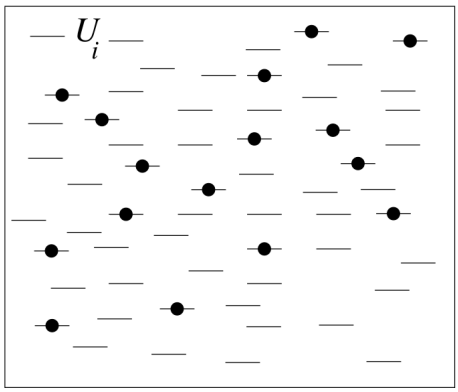

Figure 4.2: Example sample of randomly positioned sites. Flat lines indicate states, with filled circles representing electrons occupying those states. U_i is the disorder potential (ϕ_i used in text). Figure taken from Ref. [27] with personal edits.

state in these simulations refers to the state in Fig. 3.1(b). The Hall effect will be measured through the Hall current and conductivity, not by any transverse electric fields.

4.2 Kinetic Monte Carlo (KMC)

Kinetic Monte Carlo methods are able to simulate the time development of systems using relatively little computation time, and as such is especially useful for dynamic systems. There are many KMC algorithms, but the main concept is to propose and accept kinematics (jumps) based on probability rates.

4.2.1 KMC algorithms

Here is a brief description of some variants of KMC methods. To be considered here is the rejection-free, rejection and dynamic KMC algorithms.

The rejection-free algorithm computes the rate Γ_{ij} from current system state i to every possible next state j and chooses a jump $i \to j$ with probability proportional to Γ_{ij} and performs the jump. The benefit of this algorithm is that no computation time is used on unused jumps. The disadvantage is that all the rates of all the possible jumps has to be calculated at every time step. The rate computation is very costly and takes a long time.

The rejection algorithm chooses the set of sites (i, j) with uniform probability from all sets of sites. The jump is performed with probability proportional to Γ_{ij}. The benefit of the rejection algorithm is that only the one rate Γ_{ij} is calculated at each time. The disadvantage is that very few jumps are accepted at low temperatures.

The dynamic algorithm was first used by Tsigankov et al. [18] to combine the best features of the rejection-free and rejection algorithm. The basis of the dynamic algorithm is the splitting of the jump rate into a transition rate and an acceptance rate. $\Gamma_{ij} = \Gamma^T_{ij}\Gamma^A_{ij}$, with T and A symbolizing transition and acceptance respectively. Jumps are proposed with probability Γ^T_{ij} and accepted with probability Γ^A_{ij}. The key is that the transition rate is *independent* of the current system state. Therefore it can be calculated once, before any time steps are performed.

The acceptance rates should include all the configuration specific calculations and is only calcuated once per step.

The rejection-free and rejection algorithms both scale as $\mathcal{O}(N^3)$, with N being the number of sites in the simuation. The dynamic algorithm only scales as $\mathcal{O}(N^2)$ [18]. The dynamic algorithm has a massive speed advantage over the other algorithms. What the dynamic algorithm can do in less than a minute might take the other others several hours or days for normal hopping conduction. Personal tests show that the rejection algorithm is generally faster than the rejection-free algorithm, but at very low temperature ($T < 0.01$), the rejection-free wins. When including magnetic field corrections the rejection-free algorithm takes weeks to run on a normal computer. The slower algorithms have their advantages as well, the rejection-free algorithm has proven excellent for studying Coulomb glass relaxation effects [21]. It is great at finding the important jumps in the system. This is not vital when studying conductivity where sampling many jumps is more important.

4.2.1.1 Choice of algorithm

The dynamic algorithm is the ideal choice for studying conductivity, however integration with magnetic field dependence becomes problematic. The dynamic agorithm acts by using one transition and one acceptance rate. With the magnetic field corrections, the rate of one electron jumping from site i to site j is

$$\Gamma_{ij}^{\text{total}} = \Gamma_{ij}^{T}\Gamma_{ij}^{A} + \sum_{k}\left(\Gamma_{ikj}^{(0)T}\Gamma_{ikj}^{(0)A} + \Gamma_{ikj}^{(1)T}\Gamma_{ikj}^{(1)A}\right). \tag{4.1}$$

However it is not possible to split the total rate into a single transition rate and a single acceptance rate. That is, $\Gamma_{ij}^{\text{total}} \neq \Gamma_{ij}^{\text{total}(T)}\Gamma_{ij}^{\text{total}(A)}$. A similar issue was tackled by Bergli et al. in Ref. [20] when considering the possibility of simultaneous electron jumps. The solution was to let the algorithm first choose between single and simultaneous jumps, then to use the normal dynamic algorithm with a transition rate and an acceptance rate for each jump mechanism.

Applying the method directly to choose between direct jumps and jump involving three sites becomes problematic because $\Gamma_{ikj}^{(n)}$ is not a jump mechanism, it is just a magnetic field correction to the normal jump rate Γ_{ij}. Additionally, $\Gamma_{ikj} < 0$ if $\mathbf{H}\cdot\mathbf{A} < 0$. A negative transition rate is not physical and cannot be used in the algorithm. Therefore no exact integration of the magnetic field corrections is possible with the dynamic algorithm.

The rejection algorithm is able to use the magnetic field correction equations exactly. This is because the entire rate Eq. 4.1 is calculated at once. The issue with the rejection algorithm is that many jumps are rejected, making it slow. There are some ways the process can be sped up, but despite everything it is much slower than the dynamic algorithm. Low T or small a becomes problematic and impossible to study within the scope of this project with the rejection algorithm

As such we introduce an approximation or "trick" to make it possible to use the dynamic algorithm. The issue is that $\Gamma_{ikj} < 0$ if $\mathbf{H}\cdot\mathbf{A} < 0$, and since it is negative it cannot be treated as a jumping mechanism. The trick is to add a constant, magnetic field-independent term to the correction rate.

$$\Gamma_{ikj}^{(0)T} \propto \mathbf{H}\cdot\mathbf{A} \rightarrow \Gamma_{ikj}^{*(0)T} \propto (1 + \mathbf{H}\cdot\mathbf{A}). \tag{4.2}$$

Now the transition rate is positive as long as $\mathbf{H} \cdot \mathbf{A} < 1$, which can be made sure by controlling the magnetic field. If the intermediate site is occupied then the rate is $\Gamma_{ikj}^{*(1)T} \propto (1 - \mathbf{H} \cdot \mathbf{A})$.

The acceptance rate Γ_{ikj}^{A} is treated as being unchanged. The constant term in Γ_{ikj}^{*T} effectively represents non-magnetic field dependent interference between the different paths. As it is constant, and does not have an area dependence, it should not produce a Hall effect by itself. The constant term does not represent the normal jump rate Γ_{ij}^{T} as it has different intersite distance dependence.

Now that the magnetic field corrections are positive we can use Ref. [20]'s addition to the dynamic algorithm on the problem. For simplicity we introduce the names two and three-site jumps to refer to jumps involving only two sites with rate Γ_{ij} and jumps involving three sites with rate Γ_{ikj}^{*}. The algorithm will first choose between a two or a three-site jump, then find a transition and test it with the corresponding acceptance rate. This procedure ensures that each transition rate is paired up with it's corresponding acceptance rate.

The addition of this constant term should only be thought of as a trick used to gain access to the dynamic algorithm. The trick is quite a heavy approximation, and the ramifications will have to be considered before conclusions about the results can be made.

The idea is to compare the results coming from the two algorithms to determine if the trick is usable approximation. If so, the dynamic algorithm can be used to study qualitative properties while the rejection algorithm can be used to produce the main results.

4.2.2 Dynamic algorithm - algorithm 1

The dynamic algorithm is more complicated than the rejetion algorithm. It is therefore described first. The two algorithms share many similarities, but they also have many differences. A flowchart with an overview of the entire algorithm is presented in Fig. 4.3. The explanation of the steps is given in this section.

Algorithm 1a will refer to the algorithm without the addition of the three-site trick previously described. It is the exact same algorithm used by the authors of Ref. [18]. Algorithm 1b refers to the algorithm with the trick.

Initializing transition rates

The transition rate decreases exponentially as the intersite distance increases. The result being that most jumps don't go very far. Therefore it is safe to introduce a cut-off distance $r_{\text{cut-off}}$ past which jumps aren't considered. Because of the lattice structure, the transition rate is the same for all the sites. The transition rate is calculated going from one site to all other sites inside a $[(2r_{\text{cut-off}} + 1) \times (2r_{\text{cut-off}} + 1)]$ lattice. To initialize the transition rates, the algorithm loops over the lattice and calculates and stores the 2 and three site transition rates.

The cumulative sum of the transition rates is stored for every transition. It will be used by the algorithm to find transitions to test. The final sum of all the rates is also stored for the same reason. One way of doing this is presented below.

The three-site transition rate is calculated for every combination of possible intermediate and

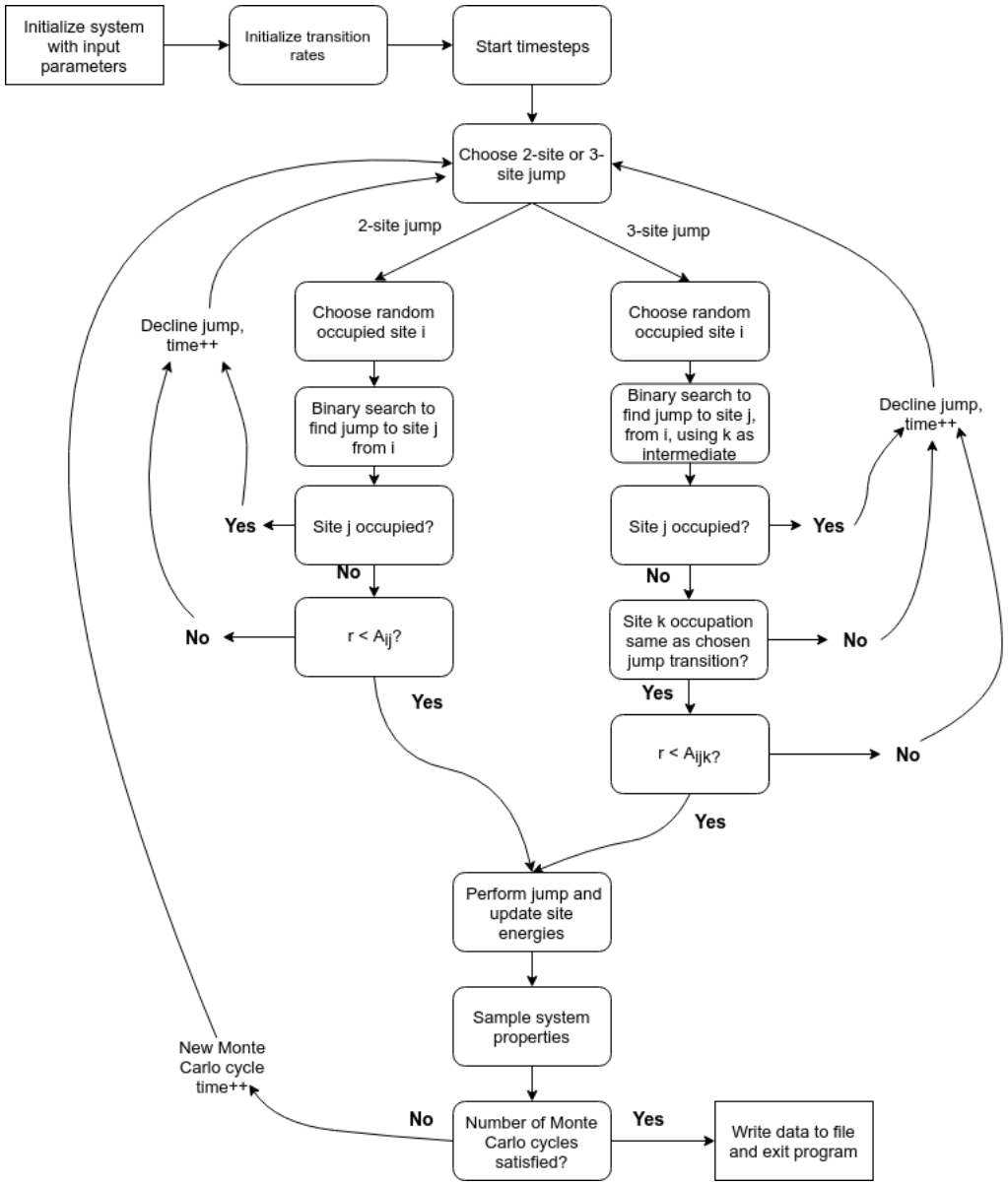

Figure 4.3: Flow chart of algorithm 1b with two and three site jumps. A_{ij} (A_{ikj}) is used in the figure to represent the acceptance rate Γ^A_{ij} ($\Gamma^{(n)A}_{ikj}$), n being the occupancy of site k if a three-site jump is tested). The quantity r is used in the figure to represent a uniformly distributed random number. A new r is generated each time it is used, and it is normalized to the acceptance function it is compared with.

final site. An array is used to store the information about if the intermediate site should be occupied or not when testing the transition rate on the system.

```
n=0;n3=0
gamma=0;gamma3=0;
// (dx,dy)=final site, (dxI,dyI)=intermediate site
for dx in range(-cutoff_distance,cutoff_distance+1):
  for dy in range(-cutoff_distance,cutoff_distance+1):
    if (dx!=0 or dy!=0): // Final site different from initial site
      r_ij = sqrt(dx*dx+dy*dy)
```

```
8
9         gamma += exp(-A*r_ij)
10        gammaT[n] = gamma
11        n++
12        // three site jumps
13        for dxI in range(-cutoff_distance,cutoff_distance+1):
14          for dyI in range(-cutoff_distance,cutoff_distance+1):
15            if (dxI!=0 or dyI!=0): // Intermediate site differenrt from initial
      site
16              if (dx!=dxI or dy != dyI): // Intermediate site different from final
       site
17                area = 0.5*(dx*dyI - dxI*dy)
18                r_ik = sqrt(dxI*dxI+dyI*dyI)
19                r_jk = sqrt((dx-dxI*(dx-dxI) + (dy-dyI)*(dy-dyI))
20
21                onePlusHA  = 1+Hz*area
22                oneMinusHA = 1-Hz*area
23                if (onePlusHA < 0)  onePlusHA  = 0
24                if (oneMinusHA < 0) oneMinusHA = 0
25
26                gamma3 += onePlusHA*(exp(-0.5*A*(r_ij+r_ik+r_jk))
27                gammaT3[n3] = gamma3
28                occupiedIntermediate[n3] = false
29                n3++
30                gamma3 += oneMinusHA*(exp(-0.5*A*(r_ij+r_ik+r_jk))
31                gammaT3[n3] = gamma3
32                occupiedIntermediate[n3] = true
33                n3++
34  totalGamma = gamma
35  totalGamma3 = gamma3
36  probability2SiteJump = totalGamma/totalGamma3
```

Time of one MC jump

The KMC algorithm is used to simulate the time development of a system. The time used by the electron jumps is important to store such that correct measurements of time dependent quantities as current, can be used. The time between jumps is the time in which nothing is happening. The jumps are of known rates and are time-independent, they are Poisson distributed. The probability of an Poisson distributed event not occuring is

$$P(\Gamma_{ij}, 0) = e^{-\lambda}$$

where λ is the expected number of events in an interval. Considering an event occuring with rate Γ_{ij} happening in a time step Δt_{MC}, we find $\lambda = \Gamma_{ij}\Delta t_{MC}$ where Δt_{MC} is the time used by one Monte Carlo step. The probability of no jumps happening is the product of each jump not happening. This quantity we call u,

$$u = \prod_i \prod_{j,j\neq i} P(\Gamma_{ij}) = \exp\left(-\Delta t_{MC} \sum_i \sum_{j,j\neq i} \Gamma_{ij}\right)$$

Solving for Δt_{MC} gives

$$\Delta t_{MC} = \log\left(\frac{1}{u}\right) \left(\sum_i \sum_{j\neq i} \Gamma_{ij}\right)^{-1}.$$

Here, u, is a random number $\in (0,1)$. It represents the fact that real events happen in random time. However, the average of $\log(1/u)$ for $u \in (0,1)$ is 1. For simulations that cover a long time the average time can be computed without any random number, without any meaningful loss of accuracy. The mean value of Δt_{MC} is

$$\langle \Delta t_{MC} \rangle = \left(\sum_i \sum_{j \neq i} \Gamma_{ij} \right)^{-1}. \tag{4.3}$$

The difference between using the Δt_{MC} and $\langle \Delta t_{MC} \rangle$ is negligable. Using the mean value skips the need for generation of random numbers, which can become costly if there are many MC steps performed.

In the system of two and three site jumps, the sum over all the rates is

$$\begin{aligned} \left(\sum_i \sum_{j \neq i} \Gamma_{ij} \right)^{-1} &= \left(\sum_i \sum_{j \neq i} \left(\Gamma_{ij} + \sum_{k,k \neq j,i} \left(\Gamma^{(0)}_{ikj} + \Gamma^{(1)}_{ikj} \right) \right) \right)^{-1} \\ &= \left(N\nu \sum_{j \neq i} \left(\Gamma_{ij} + \sum_{k,k \neq j,i} \left(\Gamma^{(0)}_{ikj} + \Gamma^{(1)}_{ikj} \right) \right) \right)^{-1} \end{aligned}$$

where in the last step we have assumed a lattice model. The implication is that the rate is independent of starting point. The only consideration is whether the starting site is occupied or not. $N\nu$ is the number of occupied sites, and is therefore the number of places the transition can start from.

The number of attempted jumps before one is accepted is noted as n. The time used by the successful jump is

$$t_{\text{jump}} = n \langle \Delta t_{MC} \rangle. \tag{4.4}$$

The dynamic algorithm proposes transitions with the transition rate and accepts them with the acceptance rate. The time between each proposed transition is Eq. 4.3 with the transition rate Γ^T_{ij} instead of the full rate Γ_{ij}. Using n as the number of proposed transitions before one is accepted, the time between accepted jumps in the dynamic algorithm is given by Eq. 4.4.

$\langle \Delta t_{MC} \rangle$ is constant throughout the simulations and only needs to be calculated once.

Performing MC jumps

The algorithm needs a way to pick two or three site jumps to test. The total transition rates for two and three site jumps are defined as

$$\Gamma^{(2)T}_{\text{total}} = \sum_{i,j,j \neq i} \Gamma^T_{ij}, \quad \Gamma^{(3)T}_{\text{total}} = \sum_{\substack{i,j,k,j \neq k \\ j,k \neq i}} \left(\Gamma^{(0)T}_{ikj} + \Gamma^{(1)T}_{ikj} \right). \tag{4.5}$$

A random number $r \in (0,1)$ is chosen, and a two site jump is tested if

$$r < \frac{\Gamma^{(2)T}_{\text{total}}}{\Gamma^{(2)T}_{\text{total}} + \Gamma^{(3)T}_{\text{total}}}. \tag{4.6}$$

If not, a three site jump is tested. The next step is to find the starting point for the jump. In the lattice structure, the symmetry implies that sum of transition rates for each starting site is identical. The result being the starting site of a jump is uniformly distributed. An initial site i is chosen at random, if it is empty then another is chosen until an occupied site is found.

Next, a transition to test is found. Performing an n-site jump, a random number $r \in (0, 1)$ is chosen then multipled with the total rate as $r\Gamma_{total}^{(n)T}$. This quantity represents the transition rate the algorithm will test. The quantity is compared with the array containing the cumulative sum. The interval in which the quantity $r\Gamma_{total}^{(n)T}$ is the transition rate to be tested. Fig. 4.4 is a visualization of this process for a system of only 4 transitions with different rates. In Fig. 4.4, $\sum_i^2 \Gamma_i < r\Gamma_{total}^{(i)T} < \sum_i^3 \Gamma_i$ and so the transition the algorithm will test is the transition with Γ_3. This method ensures that the rate of proposing transition i is proportional to Γ_i. The method used to locate i within the array of sums $\sum_i^n \Gamma_i$ is the binary search method.

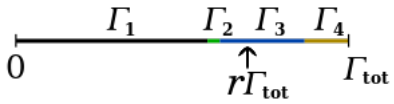

Figure 4.4: System of 4 possible transitions. The KMC algorithm draws a random number r to find what transition to test in the current time step. Transition Γ_3 is chosen in the figure. The figure is taken from Ref. [52] with small edits.

Next the transition is tested. A check is performed to see if the final site is available. If it is occupied, then the transition is discarded. If the algorithm is testing a three site jump, then the transition it is testing requires the intermediate site to be either available or occupied. If the intermediate site is not in the required state then the jump is discarded. If these tests pass, then the acceptance rate $\Gamma^{(n)A}$ is calculated. A random number r is picked. If $r < \Gamma_{ij}^{(i)A}$, the jump is accepted, if not it is discarded and a new two or three site jump is tested.

When a jump is accepted, the occupation numbers of sites i and j are switched. If the ES regime is used then the site energies are recalculated and updated. System properties such as time, energy and electron jump is sampled for every time step. The algorithm continues until a pre-defined number of jumps have been performed.

4.2.3 Dynamic algorithm on random samples - algorithm 1ar

The dynamic algorithm is also extended simulate VRH on sites with positional disorder. The algorithm is very similar to algorithm 1a. Algorithm 1ar is a bit technical to understand, the details are described in appendix A. The algorithm is less efficient and uses more RAM than the algorithm 1a uses on the lattice model. It will only be used to study the impact the lattice model has on the reuslts. Currently the algorithm only performs Mott regime VRH, using the standard dynamic algorithm (only two-site jumps).

4.2.4 Rejection algorithm - algorithm 2

The rejection algorithm is much slower than the dynamic one. As such, only the lattice model will be studied using the rejection algorithm. An attempt at using positional disorder with the

rejection algorithm revealed it to be too slow for it to be used in this thesis.

The main structure of the rejection algorithm is similar to that of the dynamic algorithm. Jumps are proposed and tested. The rejection algorithm requires little initialization because it does not rely on a transition rate. A flow chart is presented in Fig. 4.5 to give an overview of the algorithm. The details are written out in this section.

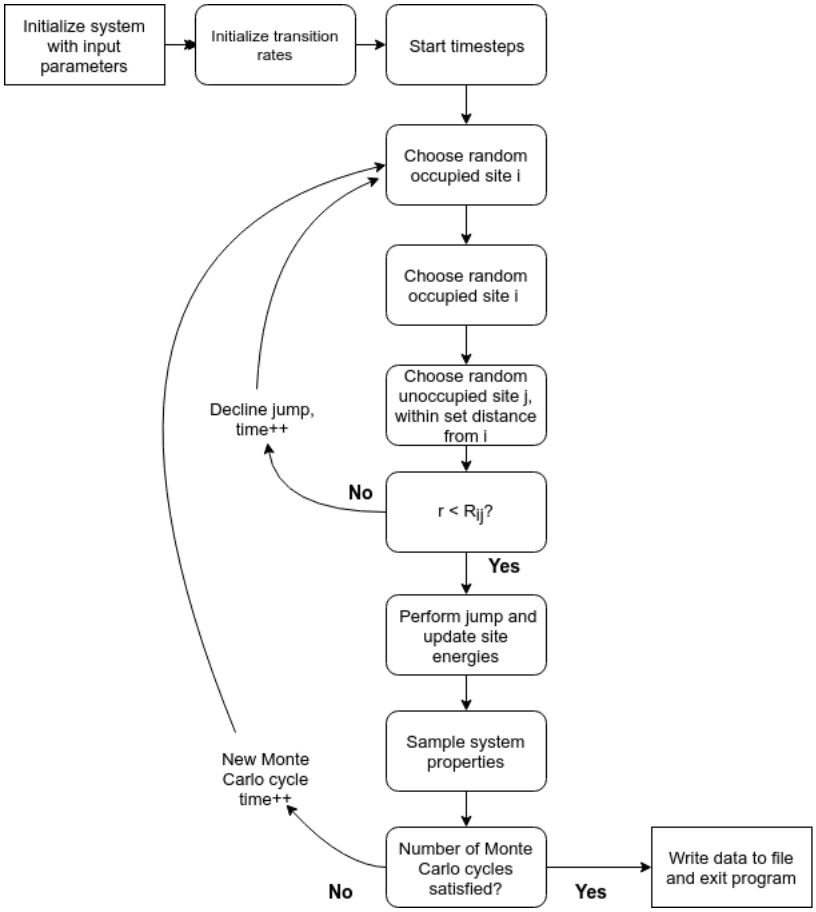

Figure 4.5: Flow chart of the rejection algorithm, algorithm 2. R_{ij} is used in the figure to represent the rate Γ_{ij}. The quantity r is used in the figure to represent a uniformly distributed random number. A new r is generated each time it is used, and it is normalized to the acceptance function it is compared with.

Finding jumps

The first step is to find from what site an electron can jump from and where it will try to jump to. Only occupied sites are considered as initial sites, and only available sites are considered as final sites. Additionally only sites within a specified possible jump region around the intial site are considered as potential final sites. This last step does not cause conflict because the jump rate decreases exponentially with distance such that jumps outside the specified region are unlikely to ever happen. The number of sites within this region is labeled N_j. These considerations are vital for making the rejecion algorithm fast enough to be useable.

Specifically the algorithm uniformly picks random sites until an occupied site i is found. It

will be the initial site. A displacement from i to another site within the possible jump region is randomly uniformly picked. The site j that the displacement from i leads to is checked if it is available or not. If available it is the final site, else another displacement from i is tested. Next, the jump from $i \to j$ is tested to see if it will happen.

Testing jumps

The complete jump rate $\Gamma_{ij}^{\text{total}}$ is calculated according to Eq. 4.1 in this step. A random number $r \in (0, \Gamma_{\text{max}})$ is generated and the jump is accepeted if $r < \Gamma_{ij}^{\text{total}}$. Else it is rejected. $\Gamma_{\text{max}} > \Gamma_{ij}$ for any possible jump is a requirement. The exact value of Γ_{max} can be chosen arbitrarily otherwise. A large Γ_{max} will discard many jumps and make simulations slow, therefore it should be set to a value close but larger than any possible Γ_{ij}.

Summing over all the possible intermediate sites in Eq. 4.1 to calculate the magnetic field correction is a costly operation. There are many costly numeric operations needed per intermediate site. Instead of considering all possible intermediate sites, the process can be sped up by only considering intermediate sites on the path from i to j. This process is visualized in Fig. 4.6. Only sites within the minimal bouncing box including both i and j are considered as intermediate sites when calculating the correction rate. An exception to the rule is made if the dx or dy$= 0$. In that case the bounding box is extended on both sides to make sure triangles with nonzero area are included.

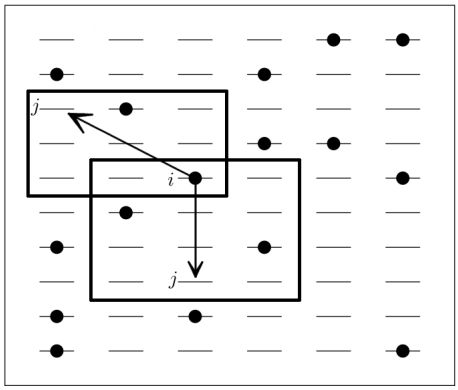

Figure 4.6: Testing a jump from i to j. Only sites within the bounding box are considered as intermediate sites. The bottom bounding box is the special case in which dx$= 0$ requiring the extended box. Figure taken from Ref. [27] with personal edits.

The bounding box method should not have noticable impact on magnetic field dependence as the jump rate depends inverse exponentially on the intersite distances.

If a jump is rejected then nothing happens and a new jump is found to be tested. The number of rejected steps for every accepted step is noted to calculate the time used by the resultant accepted jump.

Performing jumps

When a jump has been accepted the occupation numbers of i and j need to be switched. If Coulomb interaction is considered then all the site potentials need to be updated. The site

potential on site k are simply changed by subtracting $1/r_{ik}$ and adding $1/r_{jk}$. Data such as the electron displacement, time and energy is sampled after every jump has been performed. Those data are written to file for later analysis and calculation of properties such as conductivity.

Time of one jump

The real time used by jumps in the algorithm is calculated by using the number of rejected jumps before a jump was accepted. If the testing of a jump is assumed to happen instantaneously, it is only the proposal and rejection of jumps that needs to be accounted for. The number of jumps that can be found. i is picked among νL^2 sites, and j is picked among $(1-\nu)N_j$ neighboring sites. The number of possible jumps is therefore $N_{\text{tr}} = \nu(1-\nu)L^2N_j$. Once a specific jumps has been picked, the probability of accepting that jump is $P_{ij} = \Gamma_{ij}/r\Gamma_{\max}$. The mean probability of performing a jump in a given time step is

$$\langle P_{ij}\rangle = \frac{1}{N_{tr}}\sum_{ij} P_{ij} = \frac{1}{N_{Tr}\Gamma_{max}}\sum_{ij}\Gamma_{ij} \equiv \Delta t\sum_{ij}\Gamma_{ij},$$

where in the last step we have used the definition of probabilities and rates. $\Delta t = \Delta t_{\text{MC}}$ is the time one proposed jump. Solving for Δt gives

$$\Delta t = \frac{1}{N_{tr}\Gamma_{max}} = \frac{1}{\nu(1-\nu)L^2N_j\Gamma_{max}} \tag{4.7}$$

Δt_{MC} is constant throughout the simulations. Using n as the number of tries jumps tested before a jump is accepted, the time of the succesful jump is

$$t_{\text{jump}} = n\Delta t_{\text{MC}}$$

4.2.5 Energy considerations in ES-regime for magnetic field dependent jumps

These considerations are relevant for both algorithms. Both algorithms also store single particle energies ϵ_i in the same way. For a normal jump $i \to j$ in the ES regime the phonon energy required is $\Delta\epsilon_{ij} = \epsilon_j - \epsilon_i - 1/r_{ij}$. The ϵ's are calculated from the configuration of electrons and sites *before* the jump happens. The program used has these energies readily available. They are updated only after a jump has been performed. The phonon energies in the acceptance rate $\Gamma_{ikj}^{(n)A}$ depends on the energy difference between the three configurations depicted in Fig. 4.7. The jump is from $i \to j$ in the presence of site k. The program only has the ϵ's for

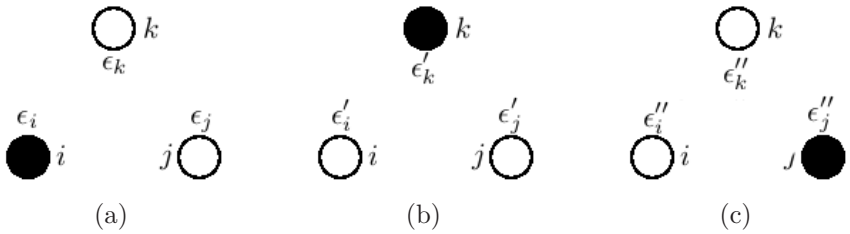

Figure 4.7: The three possible configurations of electrons on sites i, k, j when there intermediate site is unoccupied. The circles represent sites, they are filled if occupied by an electron. The jump orientation is $i \to k \to j$. The site energies ϵ depend on the current configuration.

configuration (a) when the jump is to be tested. The site potentials for the other configurations are calculated by considering the change in Coulomb potential. Take ϵ'_j from configurtion (b) as an example. Starting from configuration (a), the Coulomb interaction from site i has to be removed and added from site k. The result is $\epsilon'_j = \epsilon_j - 1/r_{ij} + 1/r_{jk}$. Using this, the phonon energy to go from configuation (b) to (c) is

$$\Delta\epsilon_{bc} = \Delta\epsilon_{kj} = \epsilon'_j - \epsilon'_k - \frac{1}{r_{kj}} = \epsilon_j - \epsilon_k + \frac{1}{r_{ik}} - \frac{1}{r_{ij}}.$$

The situation is the same for jumps using occupied intermediate sites. The only difference is the configuration between which some jumps happen. For instance, the jump $k \to j$ happens from the initial to the intermediate configuration as illustrated in Fig. 4.8, instead of from the intermediate to the final as with unoccupied three-site jumps. Since this jump starts from the initial configuration there is no need for alterations to the phonon energy required.

$$\Delta\epsilon_{ab} = \Delta\epsilon_{kj} = \epsilon_j - \epsilon_k - \frac{1}{r_{kj}}$$

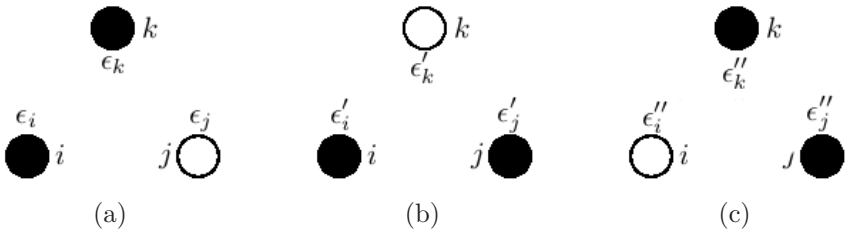

Figure 4.8: The three possible configurations of electrons on sites i, k, j when the intermediate site is occupied. The circles represent sites, they are filled if occupied by an electron. The jump orientation is $i \to k \to j$. The site energies ϵ depend on the current configuration.

4.3 System measurements

The main results from the simulations are the conductivity in x and y-direction as functions of various parameters. A description of conductivity measurements is described below, beginning with measurements of the current.

4.3.1 Current and longitudinal, Hall conductivities

Ammeters are typically used to measure current in certain directions in real materials. ammeters are devices that are inserted into the current, such that they become a part of the circuit. They measure the amount of charge that passes through the ammeter. The current is $I = Q/t$, where Q is the total charge that has passed through the ammeter in time t. Current measurements in the simulation lattice work a bit as if there is an ammeter at every position in the direction of which the current is measured. That is, to measure the x-current, there is an ammeter at every x-position that measures how much charge passes that position, regardless of the y-position of that charge. Likewise to measure the y-current, an ammeter measures the current that passes every y-position regardless of the x-position of that charge.

The way this is done is by storing the electron displacement of every jump during the algorithm. After all the jumps are finished the cumulative sum of x and y-displacement is calculated separately, jump for jump. Every 10000 jumps, the cumulative sums are written to file, along with the simulation time t. Using these quantities, the file contains x and y-charge displacement as function of time.

Consider jumps happening in the i direction. Only one jump happens at each time step s, the displacement of that jump in i direction being $\Delta r_{i,s}$. Let $N_s(t)$ be number of jumps the system has performed after the time t has paassed. The cumulative displacement sum in i direction after a time t is $\sum_s^{N_s(t)} \Delta r_{i,s}$. Multiplying this by the charge q gives us a sort of dipole moment in i-direction $p_i(t) = q \sum_s^{N_s(t)} \Delta r_{i,s}$. It represents the charge that runs through the sample. Current measurement happens at every position in the i-direction. There are L such positions, so to get the correct charge it is needed to normalize by L. The current in i-direction is then

$$I_i = \frac{Q(t)}{t} = \frac{1}{t}\frac{p_i(t)}{L}. \tag{4.8}$$

As will be demontrated later, $p(t)$ is a linear function of time that begins at the origin. Hence dividing by t is the same as differentiating with respect to t. The current is now

$$I_i = \frac{1}{L}\frac{\mathrm{d}p_i}{\mathrm{d}t}. \tag{4.9}$$

The current density is the current divided by the size of the sample. The size is just the cross section of space regarded for the current, therefore it is the sample length L.

$$j_i = \frac{I_i}{L} = \frac{1}{L^2}\frac{\mathrm{d}p_i}{\mathrm{d}t}. \tag{4.10}$$

The first few timesteps in Monte Carlo simulations do not generally describe physical realities because the initial state is drawn from complete randomness. With time, the system will evolve to a state the system is more likely to naturally find itself in. Therefore the first jumps should not be considered as part of the current measurements. We find that using the last 50% produces good results. The time derivative of p_i can be found via the use of linear regression to $p(t)$.

The conducitvity is calculated using the current density according to Ohm's law. In the direction of the electric field, it is $\sigma_x = j_x/E_x$. Similarly the Hall conductivity is using the transverse current, $\sigma_H = j_y/E_x$. The Hall conductivity should depent linearly on H, making it vital to study σ_H/H. The Hall mobility we calculate as $\mu_H = \sigma_H/\sigma_x H$.

4.3.1.1 Error in measurements

The sample the simulations are performed on is generated randomly. The site potentials ϵ are based on the uniformly random disorder potential ϕ. What jumps or paths are likely or unlikely are determined by network formed by the ϕ's. As a result, the measured conductivity will depend on the random site potentials. To minimize this randomness from results the simulations are performed on many different samples for each measurement. For the most part 10 such samples are considered, and the presented values are average quantities based on those samples.

The spread of for instance conductivity between these samples is given by the sample standard deviation, s. On some data set $\{x_1, x_2, ..., x_N\}$ with N data points and mean $\langle x \rangle$, the standard deviation is defined as

$$s = \sqrt{\frac{1}{N-1}\sum_{i=1}^{N}(x_i - \langle x \rangle)^2}. \tag{4.11}$$

The sample standard deviation s is a measure of the spread of how x_i varies between measurements. The standard deviation of the mean, defined as $s/\sqrt{N}$, gives a measure of the uncertainty in the mean value $\langle x \rangle$. This is the uncertainty that will be presented as the error of quantities measured from the algorithm.

The errors and uncertainty above deal only with the spread of measured quantites between samples, but there is also uncertainty in how quantities are measured from each sample. This will be discussed now for the conductivity of the samples.

As a result of the finite size of the sample, each sample has it's own conductance coming from the set of paths opened by the configuration of randomly generated disorder potentials ϕ_i. But there are many variables that impact the measurement of that conductance. The initial configuration has a significant impact on the conductivity at low temperatures. The measured conductivity also depends on how many timesteps are used and what data points are used when making conductivity measurements. This last point is more important at low temperatures as the current might be weak and fluctuate with time. There is also the error in the parameter found by linear regression to the current. This error depends on how linear the current is as a function of time. The current data will be very smooth and linear for high temperatures and the parameter error amounts is negligable. Personal testing finds the parameter error to be no more than 5% for very low temperature measurements of Hall conductivity. For these kinds of measurements there is a much larger uncertainty coming from the spread between samples. Therefore the parameter error is also negligable in these cases. This means that the error of the measurements in the coming result section should be larger than what is presented, but not so large that it will affect how the data can be interpreted.

4.3.2 Measurements of Hall effect parameter

The Hall effect parameter α describes the relationship between the conductivities, σ_x and σ_H. Effectively it gives the relationship of how resistant to temperature changes the conductivies are.

There are some different methods that can be used to determine the value of α from the data. Theoretical predictions are that the Hall mobility, $\mu_H = \sigma_H/\sigma_x H$, should be $\mu_H \propto T^{1-\lambda}\exp(-\alpha(T_0/T)^p)$. T_0 should only be dependent on localization radius a, and whether Coulomb interactions are considered or not. p is the VRH exponent and also depends on if there are Coulomb interactions. If λ is known (method of finding λ will be described later), then plotting $\ln\left(\mu_H T^{\lambda-1}\right)$ on one axis and $1/T^p$ on the other should result in a straight line with slope $-\alpha {T_0}^p$. Likewise, the function form of the x-conductivity σ_x should be $\sigma_x \propto T^{-1}\exp(-(T_0/T)^p)$. Therefore plotting $\ln(\sigma_x T)$ on one axis and $1/T^p$ on the other should produce a straight line with slope ${T_0}^p$. By comparing measurements of the quantity $\alpha {T_0}^p$ from μ_H and the quantity ${T_0}^p$, it is possible to calculate α.

Another method to compare the conductivities, σ_x and σ_H, directly. The Hall conductivity should be on the form $\sigma_H \propto T^{-\lambda}\exp(-(T_H/T)^p)$, where $T_H = (1+\alpha)^{1/p}T_0$. Knowing the value of λ, plotting $\ln\left(\sigma_H T^\lambda\right)$ as function of $1/T^p$ should give a straight line with slope $T_H^{\,p} = (1+\alpha)T_0^{\,p}$. Measuring $T_0^{\,p}$ from σ_x using previously mentioned methods, α can be calculated as

$$\alpha = \frac{T_H^{\,p} - T_0^{\,p}}{T_0^{\,p}}. \tag{4.12}$$

The relationship between the conductivities can also be expressed as $\sigma_H T^\lambda \propto (\sigma T)^{1+\alpha}$. This can also be used to measure α. A plot of $\ln\left(\sigma_H T^\lambda\right)$ vs $\ln(\sigma_x T)$ should result in a linear curve with slope $= 1+\alpha$ that can be measured.

We have three methods that can be used to measure α from the same dataset. If these three methds return the same or similar values then it supports the function form of σ_H that has been theoretically predicted.

4.3.2.1 Error in Hall effect parameter measurements

The error in α, $\Delta\alpha$ depends on the method used to calculate it. Starting with calculating from Eq. 4.12, the error can be calculated from the errors $\Delta T_H^{\,p}$ and $\Delta T_0^{\,p}$. Defining $\alpha = \alpha(T_H^{\,p}, T_0^{\,p})$, we have from Ref. [53] that

$$(\Delta\alpha)^2 = (\Delta\alpha_{T_H^{\,p}})^2 + (\Delta\alpha_{T_0^{\,p}})^2, \tag{4.13}$$

where

$$(\Delta\alpha_{T_H^{\,p}})^2 \equiv \left(\frac{\partial\alpha}{\partial T_H^{\,p}}\right)\Delta T_H^{\,p} \tag{4.14}$$

and likewise for $T_0^{\,p}$. Setting Eq. 4.12 into the above equations returns the final error

$$\Delta\alpha = \sqrt{\left(\frac{\Delta T_H^{\,p}}{T_0^{\,p}}\right)^2 + \left[\left(\frac{T_H^{\,p}}{T_0^{\,p}} + 1\right)\Delta T_0^{\,p}\right]^2}. \tag{4.15}$$

Let us define $T_{\mu_H}^{\,p} = \alpha T_0^{\,p}$ to be the slope measured when plotting $\ln\mu_H$ as function of T^{-p}. Then $\alpha = T_{\mu_H}^{\,p}/T_0^{\,p}$. From [53] the error of this calculation is

$$\Delta\alpha = \alpha\sqrt{\left(\frac{\Delta T_{\mu_H}^{\,p}}{T_{\mu_H}^{\,p}}\right)^2 + \left(\frac{\Delta T_0^{\,p}}{T_0^{\,p}}\right)^2}$$

When using the relation $\ln\left(R_H T^\lambda\right)$ vs $\ln(\sigma_x T)$, the error is simply the parameter error of the linear fitted line.

4.3.3 Density of states

Coulomb interactions manifest themselves physically in the VHR system through density of states (DOS). In the ES regime with Coulomb interactions at $T = 0K$ the DOS is exected to

vanish at the Fermi energy, forming the Coulomb gap. As temperature is increased the gap slowly dissapears, but should still be visible at low temperatures. In the Mott regime the DOS should be constant. The DOS is a good property to measure to ensure test that the Coulomb gap does exist, and that the ES regime is behaving as expected.

The DOS can be measured by writing the single particle energies ϵ_i of all the states to file and binning the data into a histogram. Using just ϵ_i's from a single 100×100 sample will result in noisy data. Concatenating together multiple simulation runs from different samles together into one histogram should reduce this noise.

4.3.4 Current maps

Maps of where current is flowing through the sample can be made in the KMC algorithm. The map can be represented by a matrix M where each matrix element represents a position on the sample. We consider a jump $i \to j$, each site k having positions x_k, y_k. The jump happens with corresponding displacement dx, dy. The current generated in the x-direction is dx and dy in the y-direction. The simplest idea for a current generation map is to add the current generated by that jump to both sites i and j. For an x-current map Mx this is implemented by performing

$$Mx_{x_i,y_i} = Mx_{x_i,y_i} + dx, \quad Mx_{x_j,y_j} = Mx_{x_j,y_j} + dx$$

after every jump. Likewise to produce a y-current generation map My, the map is updated as $My_{x_i,y_i} = My_{x_i,y_i} + dy$ for sites i and j, after every jump. These maps give microscopic view of what is happening in the sample, and will be good tools for later.

The first few jumps in the algorithm should be ignored by the maps such that current generated on non-percolation clusters does not show up.

In the sample it is very likely that there will be some pairs of sites that are close to each other in both position and energy. Between such sites, it is easy to jump in both directions. These kinds of jumps dominate the dynamics happening on the sample at low temperatures. For instance in Ref. [21] it was necessary to make an algorithm that filters out these types of jumps from happening. The good thing about the above detailed procedure of making current generation maps is that these jumps are filtered out. If an electron just jumps back and forwards between two sites, then no net current is generated and it will not show up on the maps.

4.3.5 Algorithm limitations

The algorithm comes with several limitations, with their repective difficulties and solutions.

4.3.5.1 Conductivity in non-percolating clusters

The above mentioned algorithm counts any movement in the system as current. It means current from the finite, non-percolating clusters will be added to the calculated current. (The brown network in Fig. 2.4 is finite and non-percolating.) This is not problematic for DC current as most of the current on these finite networks happen only during the configuration time of the system. Thus the effect is minimized by only using data from after the configuration time.

Current on finite networks becomes significant for systems using AC voltage. Current will travel in finite networks until saturated every time the applied electric field is switched.

4.3.5.2 Choice of magnetic field and negative rates

The magnitude of the magnetic field determines how strong the Hall current will be. As will be seen in the results section, larger magnetic fields give rise to Hall conductivities with smaller variation between samples. The uncertainty also tends to become large at small temperatures. To gain stable measurements, a large magnetic field should therefore be used. By treating the magnetic field corrections as three-site jumps with rate $\propto (1 \pm \mathbf{H} \cdot \mathbf{A})$, it becomes necessary to use fields such that $\mathbf{H} \cdot \mathbf{A} < 1$. If a jump has negative rate it will impact the other jump rates by disturbing the binary search method used in the KMC algorithm. The binary search method assumes the sum of rates is a monotonic increasing sum. There are many jumps that go very far, and have large areas such that $\mathbf{H} \cdot \mathbf{A} < 1$. Such jumps have very small transition rates and would happen very infrequently. The problem is fixed by setting $\mathbf{H} \cdot \mathbf{A} = 1$ if it should be less. The largest area that is performed often enough is jumps with $A = 2$. This sets the requirement for $H < 0.5$.

4.4 Differences between KMC and percolation approaches

To date, the only other simulations on VRH Hall effect are [15–17], all using percolation simulations. An outline of the methods used in [17] is described here. The Mott regime will be described as an example. The sites are created with a random disorder potential ϕ, but the sites are not filled. The electric and magnetic fields are applied to sample. The configuration of ϕ's combined with the external fields is used to calculate the average charge on each site. The percolation parameter ξ is introduced and sites bond by the normal bonding criteria (Eq. 2.9), until a percolating network forms at some ξ_C. The percolating network is analyzed and the currents are calculated to solve Kirchiff's equations, finding the conductivity in x and y-directions. [17] uses a zero-temperature Monte Carlo algorithm to produce a ground state with Coulomb interaction. The resultant ground state is then analyzed with the same percolation methods, produing a static ES regime.

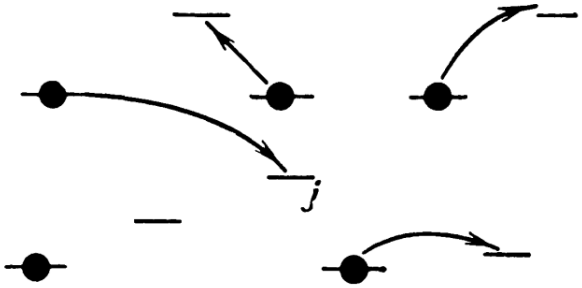

Figure 4.9: A polaron cloud. An electron jumping to site j effectively pushes other electrons away from site j. Figure taken from page 235 of Ref. [25]

KMC simulations are arguably closer to nature than percolation simulations. Effectively, percolation simulations analyze the sample system and gives an estimate for how current would move on the sample. The KMC algorithm physically simulates the sample dynamics by simulating the time evolution, allowing for the measurement of time correlated effects. The

configuration of ϵ's being updated after every MC step is such a time correlation. Another is the polaron cloud effect illustrated in Fig. 4.9. In the ES regime an electron jumping to site j changes the potential on the other sites, making it easier for them to jump away from j. The effect is also present in the Mott regime, the occupancy of site j means electrons on neighboring sites have to find other sites to jump to. Such effects are impossible to add to percolation methods, as it is a time dependent one.

The sources of error are also different between percolation and KMC methods. Percolation methods heavily depend on averaging, that act as a potential source of error. Percolation simulations do not generated random initial positions. The KMC algorithm has errors that depends on the initial configuration of the sample, the random numbers used for finding and testing jumps in the simulation, and the decision of how many steps should be performed before the simulations end. Additionally the question of how long the configuration time (the time it takes for the system to move from it's random initial state to a natural, more physical state), is a source of error when analyzing results.

CHAPTER 5

Results and discussions

The main goal of this section is to present the results of the Hall mobility simulations. The first section is devoted to test the algorithms against Mott's and ES's law for σ_x when simulating using the different VRH regimes. This will be done for all the algorithms. This will include fitting the simulated data to Mott's law exponent of 1/3 and ES's law exponent of 1/2, and testing whether the T_{Mott} or T_{ES} best produces a data collapse.

Similarities and differences between the dynamic algorithms and the rejection algorithm need to be drafted to determine what results can be considered as valid. Then the Hall conductivity and mobility will be studied.

We wish to remind the reader that algorithm 1 is the dynamic algorithm, using 1a to denote the standard algorithm and 1b as the dynamic algorithm with three-site jumps. Algorithm 2 is the rejection algorithm that is able to use the magnetic field rate correction equations exactly.

Distances are presented in unitless form scaled by the lattice constant. A localization radius of $a = 0.5$ means the localization length reaches halfway from one site to it's closest neighbor. T is the thermal energy, and by setting Boltzmann's constant $k_B = 1$, the thermal energy and temperature are identical. Time is always presented in units of the phonon-relaxation time $\tau_0 \approx 10^{-12}s$, defined by Eq. 2.5.

All electric fields considered in this project are aligned along the x-axis. $\mathbf{E} = E_x\hat{\mathbf{x}}$. Likewise, all magnetic fields are aligned along the z-axis. $\mathbf{H} = H_z\hat{\mathbf{z}}$

5.1 Current and conductivity in the x-direction

Input parameters such as suitable temperature range, magnetic and electric fields need to be established before simulations are started. The author of Ref. [27] find that a temperature range $T \in [0.02, 0.50]$ is suitable for simulating variable range hopping. To study just the normal behavior of σ_x, the external magnetic field is set to zero.

The conductivity is measured using the relationship between the current density and the applied electric field. The current density is the gradient of the accumulated charge passed through the sample as function of time.

5.1.1 Accumulated charge

The data saved to file from the simulations is the cumulative sum of electron displacement in x and y directions as function of time. As discussed, this is equivalent to the charge that has passed through the ammeters. The accumulated charge for 10 samples with an external electric field is presented in Fig. 5.1. The data is generated using algorithm 1a, the other algorithms produce accumulated charge behaving in the same manner. The high temperature situation is shown in Fig. 5.1a, and the low temperature in Fig. 5.1b. Each sample is randomly generated, and uses different initial configurations and random numbers.

The variation in accumulated charge between samples is low for high temperatures and high for low temperatures. This can be attributed to the density of paths in the percolating network. At high temperatures there are many available paths, and so the differences between two samples is small. For low temperatures there are few paths, and the dynamics are determined by the characteristics of some important paths. Therefore the spread is large from sample to sample.

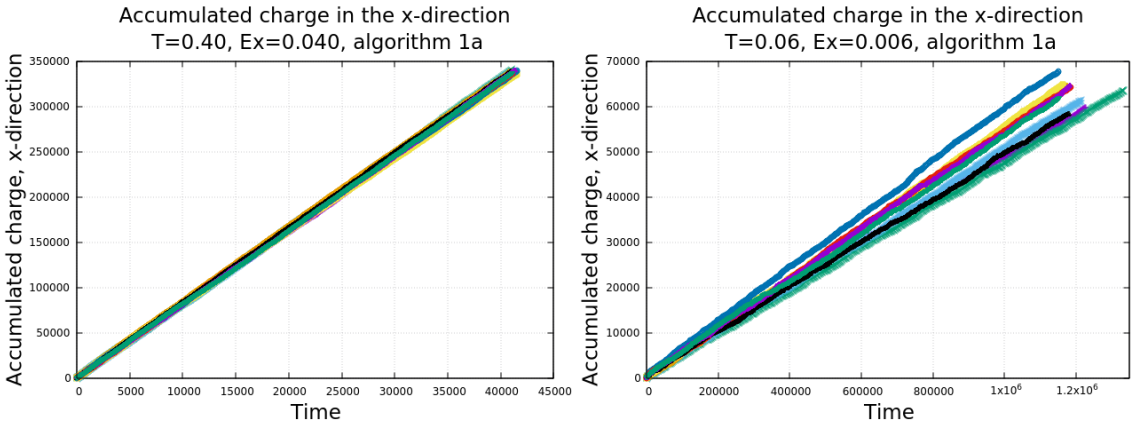

(a) (b)

Figure 5.1: Accumulated charge in the x-direction measured in simulations as function of time for 10 different samples. (a) is for a high temperature $T = 0.40$ and (b) is for low temperature $T = 0.06$. Both figures are simulated using $a = 2/3$. The graphs show the expected linear behavior.

The accumulated charge is observed to be linear as expected. At low temperature there are some visible deviations, especially in the early jumps performed by the system. The decision is made to *only* consider the 50% last jumps of the system when sampling properties. A linear fit is made to each samples' accumulated charge to find the current. The current is combined with the external electric field to give the conductivity.

Changing the localization length has a large impact on the rate of acceptation of steps. Keeping all other parameters constant and changing the localization length from $a = 2/3$ to $a = 2/6$ changes Fig. 5.1b to B.1. As seen, smaller localization length makes the current less stable and introduces larger variance between samples.

The number of jumps decided to use for these simulations should be of the order of 10^6 to 10^7, depending on temperature and localization lengths. Smaller temperature and smaller

localization length requires more jumps to create accumulated charge from which meaningful conductivities can be extracted. For very low localization lengths 10^8 jumps might be needed. The acceptance rate of jumps decreases exponentially with decreasing localization lengths, meaning simulation time is exponentially increasing.

Based on these observations, and from the results of Ref. [17], this project will look at $a \in (1, 0.2)$. These are localization lengths which are small enough to produce VRH dynamics, and large enough that simulations are possible.

5.1.2 Ohmic region of electric fields

Ohm's law, $\sigma_x = j_x/E$, is only an accurate model for small electric fields. If large electric fields are applied, then the conductivity becomes non-Ohmic and has different properties (see [27]). Therefore it is necessary to classify what electric fields will produce Ohmic conditions. This is done by simulating the conductivity, calculated using Ohm's law, for constant temperature over a spectrum of electric fields. Ohmic conductivity should be constant with E. Simulated results are presented in Fig. 5.2.

Figs. 5.2a and 5.2b show the conductivity simulated by algorithms 1a and 1b respectively. σ_x in Fig. 5.2a is approximately constant for small electric fields and increasing slowly when E is large. The conductivity increases more for small temperatures than large temperatures. For $T = 0.2$, $\sigma_x \approx$ constant for $E <= 0.025$. For $T = 0.3$ and $T = 0.4$ it is approximately constant for much longer. Up to about $E = 0.05$ for $T = 0.3$ and $T = 0.4$ shows no deviation from constant behavior.

Algorithm 1b results shows similar yet different behavior. $T = 0.2$ is initially decreasing before increasing again as E is increased. The same behavior is observed for $T = 0.3$ but is less apparent. $T = 0.4$ displays a decreasing tendency. Despite the different behavior, σ_x is $\approx$ constant for about the same region of E for both versions of the dynamic algorithm.

Algorithm 2 produces seemingly the exact same dependence of j_x and σ_x on E simulated as algorithm 1a. This is shown in Fig. B.2.

As seen, the choice of electric field affects the measured conductivity. The system only obeys Ohmic behavior for small electric fields. When simulating the conductivity it is therefore important to use electric fields small enough such that they are Ohmic. It is also observed that fluctuations become large for very small fields. Therefore fields that are sufficiently small but not too small are required. The region of Ohmic fields is observed to increase with temperature. Ref. [27] made similar observations and decided to use $E = T/10$ for simulations. We decide to do the same.

The exact cause of non-Ohmic behavior in this model is still a disputed topic. One idea is that large electric fields heat up the system, thereby increasing the conductivity. Ref. [27] find evidence supporting this idea at low temperatures. The three-site algorithm differs from the standard algorithm in that there are regions where σ_x is decreasing with increasing E. The decrease is not expected and is likely un-physical behavior added through the use of the three-site jump trick.

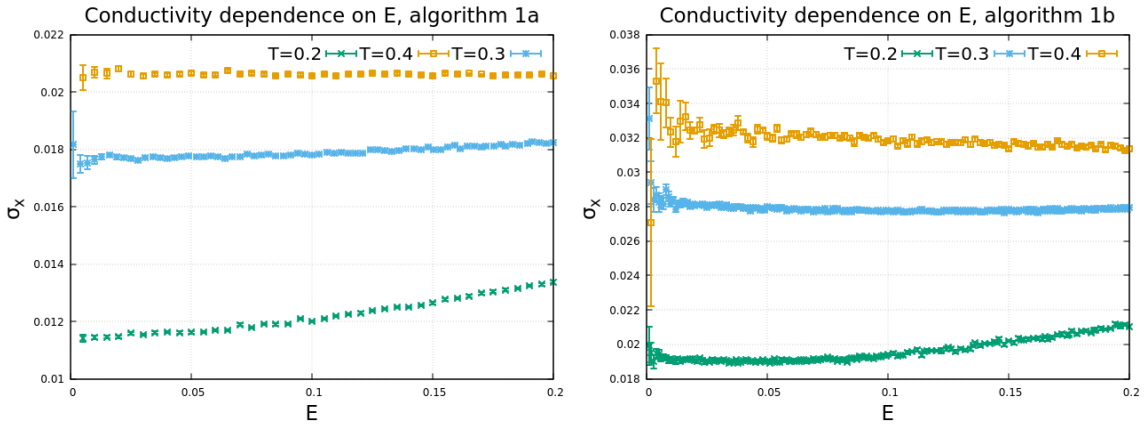

(a) (b)

Figure 5.2: Longitudinal conductivity σ_x dependence on applied electric field E for algorithms 1a (a) and 1b (b). The data is an average of 30 samples.

5.1.3 Mott regime simulations

This section covers results from all the algorithms simulating the Mott regime conductivity, one algorithm at a time. Algorithms 1a and 2 with $H = 0$ have been used by other scientific work and are already known to work. Algorithm 1b needs to be tested see if it is able to reproduce Mott's and ES's laws for σ_x. There is a comparison and summary at the end. σ_x is simulated using $E = T/10$, for a range of temperatures and for some localization lengths a.

5.1.3.1 Algorithm 1a

The simulated results are presented in Fig. 5.3. The figures use $T_{\text{Mott}} = a^{-2}$. The fitting and plotting is done without the theoretical value of C_{Mott} (defined in section 2.3.3). Doing so allows measurements of C_{Mott} to be made from simulations. If a figure shows a linear behavior it is an indication that it follows the respective law it is plotted as.

Fig. 5.3a shows Mott regime generated data fitted to Mott's law. For each localization length, the data shows a linear behavior within itself for low and medium temperatures while falling off for high temperatures ($T \gtrapprox 0.30$). The slope of the linear section should be equal to a constant $C_{\text{Mott}}^{1/3}$. The measured slopes are presented in table 5.2 and has a systematic decrease with decreasing a. This aspect be discussed in section 5.1.3.5.

Fig. 5.3b instead shows Mott regime generated data plotted using 1/2 as exponent instead of 1/3. The red dotted line is the linear fit to the $a = 2/3$ data points. The data is clearly not linear on this axis. The trend over all the localization lengths is an upwards curve instead of a linear slope. Looking at the $a = 2/4$ or $a = 2/6$ it is possible to see that the individual curves are not linear themselves but feature an upwards curve.

Comparing Figs. 5.3a and 5.3b it is possible to determine that 1/3 as exponent fits the data much better than 1/2. The data collapse in Fig. 5.3a becomes worse at smaller a, but each localization length produces a linear curve when the exponent is 1/3. A way of testing the linearity is to plot the difference between the linear fit and the data points. This is done for both exponents and the data is presented in in Figs. 5.3c and 5.3d. The error in Fig. 5.3d

clearly follows a systematic behavior, meaning there is some extra behavior not picked up by the linear fit. The error seems to be more random in Fig. 5.3c, indicating that all the behavior is included and the errors are just fluctuations. Clearly 1/3 as exponent fits the data better than 1/2.

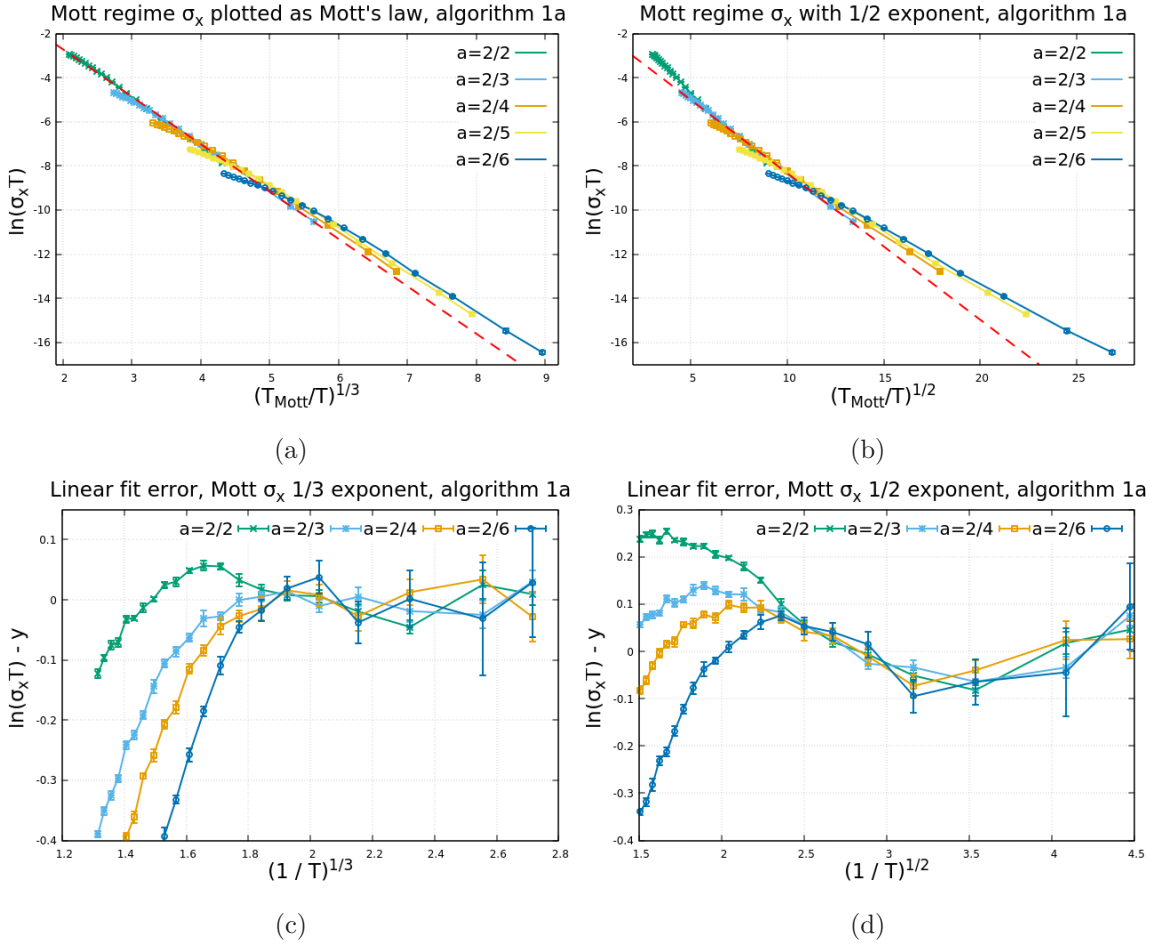

Figure 5.3: Temperature dependence of Mott regime simulated σ_x. (a) tests with Mott's law and (b) tests with 1/2 exponent. The difference between the linear fitted line to low temperatures and the simulated σ_x using exponent 1/3 (c) and 1/2 (d). 1/3 exponent fits the data better than 1/2.

5.1.3.2 Algorithm 2

Mott regime generated data fitted to Mott's law is presented in Fig. 5.4 for $T \in (0.12, 0.44)$ for each a. The dotted line in Fig. 5.4 is the linear fit to the linear part of the $a = 2/3$ data. As seen, there is a general deviation from the line for the other localization lengths. The deviation is consistent with observations made from the algorithm 1a data for the given temperature range.

Numerical values of the slopes in Fig. 5.4 are presented in table 5.2. The slopes in table 5.2 shows that algorithms 1a and 2 do produce the same results.

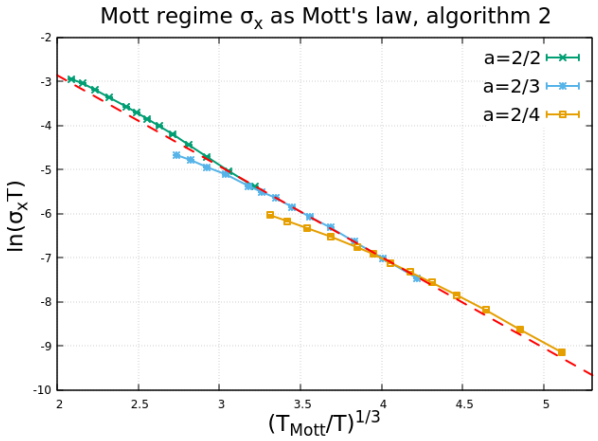

Figure 5.4

Figure 5.5: Mott regime σ_x plotted as Mott's law using algorithm 2. The result show similar behavior to that of algorithm 1a in Fig. 5.3a, but over a smaller temperature range.

5.1.3.3 Algorithm 1b

Mott regime simulation data from algorithm 1b is plotted as Mott's law is presented in Fig 5.6. Fig. 5.6b shows the same as Fig. 5.6a, but zoomed in on the large localization lengths and high (T_{Mott}/T).

Fig. 5.6a shows that the different localization lengths approximately collapse on the same line. The dotted red line is the linear fit to the linear section of the $a = 2/4$ data. Fig. 5.6b shows that the collapse does not work between the large localization lengths. There is a vertical shift especially noticeable between $a = 2/2$ and $a = 2/3$ in Fig. 5.6b. The vertical shift seems to shrink and become negligible between the smaller a. The measured values of the slopes in Fig. 5.6a are presented in table 5.2. Algorithm 1b measures the same problems as the others, the slope does not appear to be independent of a.

The collapse discontinuity in Fig. 5.6b might be attributed to the large number of three-site jumps used by algorithm 1b for these a. As the localization length is decreased, fewer three-site jumps are used and the collapse seems to work in the same manner as for algorithm 1a. Even when there are very few three-site jumps there is a clear difference in slopes between algorithms 1a and 1b (see $a = 2/6$ slopes in table 5.2).

The lack of collapse for large a in Fig. 5.6 might indicate that there is some extra a dependence not being accounted for by the standard σ_x equation. Changing σ_x by including an a dependence such as

$$\sigma_x \propto \frac{a^{\gamma_x}}{T} \exp\left(-\left(\frac{T_{\text{Mott}}}{T}\right)^{1/3}\right), \tag{5.1}$$

we find a data collapse using $\gamma_x = 2$ that can be seen in Fig. 5.7a. The $\gamma_x = 2$ data collapse fits better for high a, but worse for small a. As such, it will not be possible to find a value of γ_x that will produce a perfect data collapse. Do note that the slopes are independent of the value of γ_x.

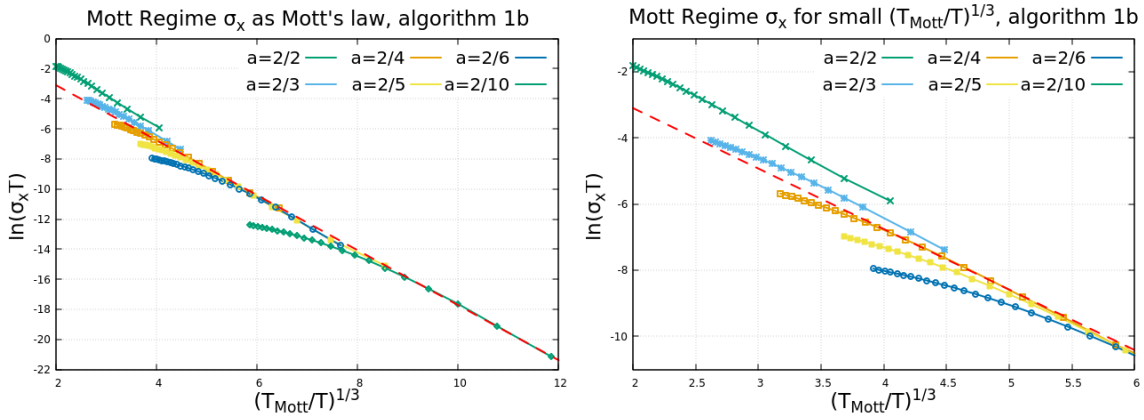

(a) (b)

Figure 5.6: Mott simulated data using algorithm 1b compared with Mott's laws. (b) shows that there are some problems happening at large localization lengths, but (a) the collapse works well for the lower ones.

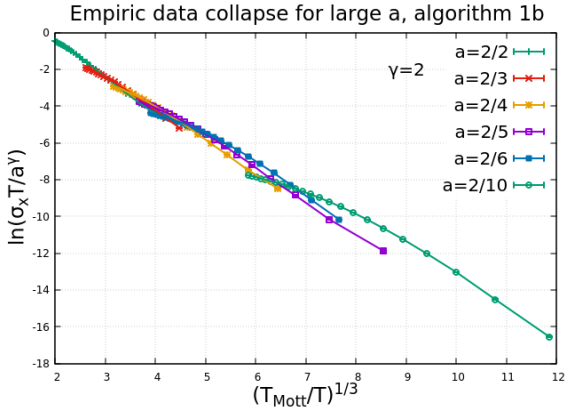

(a)

Figure 5.7: Empirical relation for Mott regime σ_x simulated by algorithm 1b. Adding an a^{γ_x} proportionality to σ_x improves the data collapse for large a, but worsens it for small$a$.

Comparison with algorithm 1a

The impact of the "trick" used to design algorithm 1b needs to be studied closely before conclusions about it can be made. Therefore a comparison with algorithm 1a, that is known to be producing working results, will be useful.

Looking at Fig. 5.3a, we see that $\ln(\sigma_x T)$ is linear or close to linear with respect to $T^{-1/3}$ for low temperatures. A comparison of the linearity between algorithms 1a and 1b is done in section C. The conclusion is that it looks like there is systematic behavior simulated by algorithm 1b, not picked up by Mott's law, but not critical such that Mott's law is still a good approximation. Similar extra systematic behavior is arguably also present in algorithm 1a simulations, but to a lesser degree.

Table 5.1 shows how the probability of the algorithm choosing to *test* a three-site jump, P_3,

changes with localization length. P_3 is large for large a but decreases quickly as a decreases. Using $a = 2/6$ and $T = 0.40$, only 7% of jumps are three-site jumps. The percentage of performed three-site jumps is also decreasing with decreasing temperature (not shown). Even so the few three-site jumps have a significant impact on the conductivity, especially at low temperatures (see Fig. C.1g).

From this it is possible to see that algorithm 1b has some differences but also many similarities to algorithm 1a. The differences do not seem to vanish as the number of three-site jumps in algorithm 1b is lowered by decreasing a.

Table 5.1: Three-site jumps in algorithm 1b. P_3 is the probability of algorithm 1b choosing to test a three-site jump in a given MC cycle. n_3 is the percentage of three-site jumps performed by the algorithm at $T = 0.40$.

a	P_3	n_3
2/2	0.85	0.70
2/3	0.67	0.45
2/4	0.46	0.26
2/6	0.16	0.07
2/10	0.01	0.004

5.1.3.4 Algorithm 1ar - samples of randomly positioned sites

Mott regime conductivity is also simulated using sites with positional disorder. The same input parameters of electric field and temperature as earlier are used. The result is presented in Fig. 5.8. The simulated conductivities for different localization lengths all converge together to a single universal curve.

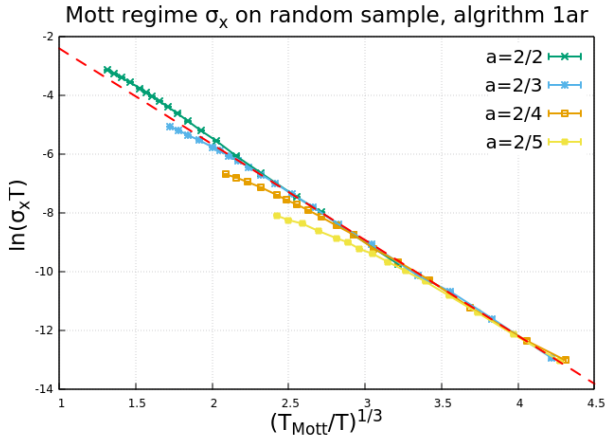

Figure 5.8: Mott regime longitudinal conductivity σ_x simulated on randomly positioned sites using algorithm 1ar. The conuductivity using different localization lengths collapse together well. The dashed red line is a linear fit with slope -3.26 ± 0.03.

5.1.3.5 Measured Mott slopes

Table 5.2 presents the slopes of the curves in Mott regime σ_x fitted to Mott's law for the different algorithms.

The errors presented in table 5.2 is the error of the slope given by the linear regression method. There is another error coming from what data points are included in the linear regression. As such is it should be noted that the errors of measured slopes should be larger by some percent, but not significantly.

The values in table 5.2 are made using a linear fit to the curves within a specified temperature range. If the temperature range is limited to include only low temperatures in the Mott regime, say $T \in (0.04, 0.12)$, then the same systematic a dependence is observed.

When using the same temperature range, algorithm 1a and algorithm 2 produce almost exactly the same slopes. This is a strong indication that the algorithms simulate the same dynamics. It is safe to say that algorithm 2 would produce the same results as algorithm 1a, if given enough time to simulate low temperatures.

The slope measured by algorithm 1b is consistently smaller than that of algorithm 1a. This can be explained by considering the definition of the VRH temperature constant. For the Mott regime it is,

$$T_{\text{Mott}} = \frac{C_{\text{Mott}}}{a^2}, \quad C_{\text{Mott}} \propto n_C \tag{5.2}$$

where n_C is the critical concentration that will produce a percolating cluster. The introduction of the three-site jumps introduces a new criteria for two sites to be part of the same cluster. Three-site jumps therefore change the dynamics of the infinite cluster, hence the critical concentration will be changed. Adding another jump mechanism should simply lower the percolation criteria, lowering n_C and also T_{Mott}. This explains the reduced slope when three-site jumps are added to the dynamic algorithm.

According to Mott's law, the slopes of the data in Figs. 5.3a, 5.4 and 5.6a should be $C_{\text{Mott}}^{1/3}$ and independent of a. The measured slopes from algorithm 1a, 1b and 2 do however clearly have a systematic a dependence. All the slopes in table 5.2 decrease with decreasing a. The algorithm using sites with positional disorder does produce $C_{\text{Mott}}^{1/3}$ independent of a, in agreement with theory. This means that lattice effects are the reason why the other algorithms are unable to produce a σ_x data collapse to a universal curve.

Table 5.2: Value of $C_{\text{Mott}}^{1/3}$ measured from Mott regime generated temperature dependence of σ_x for all three algorithms. The specified temperature range is the range used for making the measurement of the slope.

a	Algorithm 1a		Algorithm 2	Algorithm 1b
	$T \in (0.04, 0.24)$	$T \in (0.12, 0.24)$	$T \in (0.12, 0.24)$	$T \in (0.04, 0.24)$
2/2	3.67 ± 0.01	3.76 ± 0.02	3.73 ± 0.02	3.30 ± 0.02
2/3	3.41 ± 0.01	3.35 ± 0.02	3.33 ± 0.03	3.06 ± 0.03
2/4	3.29 ± 0.02	3.10 ± 0.03	3.06 ± 0.06	2.95 ± 0.02
2/6	3.13 ± 0.02	-	-	2.90 ± 0.04
Algorithm 1ar $C_{\text{Mott}}^{1/3}$ converges to 3.26 ± 0.03 for all a				

5.1.4 ES regime simulations

This section is structured in the same manner as the Mott regime section. There is a description of the results coming from each algorithm, with a table of measured slopes at the end. All the results in this section are simulated using electric fields $E = T/10$. We begin with a measurement of the DOS to check if the Coulomb gap is correctly produced in ES regime simulations.

5.1.4.1 Density of states

Fig. 5.9 shows the DOS when dynamic electron-electron interactions are considered in simulations. The DOS histogram is made by concatenating 10 simulation together, using the single particle energies ϵ_i after 10^7 jumps. Fig. 5.9 shows a clear Coulomb gap present at $\epsilon = 0$. The measured Coulomb gap does not reach $g(\epsilon = 0) = 0$, that is only expected to happen at $T = 0$. The Coulomb gap becomes deeper as the temperature is lowered from $T = 0.05$ to $T = 0.03$ hinting it may reach zero at $T = 0$. For Mott regime simulations, the measured DOS is a completely constant function of ϵ (not shown).

In two-dimensions the Coulomb gap DOS is expected to be a symmetric linear function of ϵ close to $\epsilon = 0$ at $T = 0$. The behavior of $g(\epsilon)$ at $T = 0.03$ in Fig. 5.9 immediately around $\epsilon = 0$ seems to be more parabolic than linear. This is not an issue as the linear prediction of $g(\epsilon)$ is made at $T = 0$.

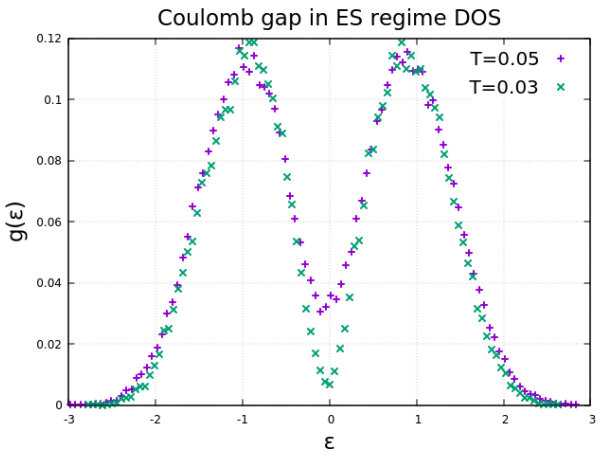

Figure 5.9: DOS measured from ES regime simulations for $T = 0.05$ and $T = 0.03$, using $a = 2/2$. The figure shows a clear Coulomb gap. The simulations are performed using algorithm 1a. There are no visual changes in the DOS when using other algorithms.

5.1.4.2 Algorithm 1a

Fig. 5.10a presents ES regime generated data fitted with ES's law. We use the definition $T_{\mathrm{ES}} = a^{-1}$. The plots of the different localization lengths seem to collapse together at the very low temperatures. Only the smallest temperatures $T = 0.06 - 0.05$ are close to the line of best fit for $a = 2/6$. Fig. 5.10b shows ES regime data plotted to $1/3$ exponent, showing little visual difference from the $1/2$ exponent in Fig. 5.10a. It seems like it is easier to differentiate between $1/3$ and $1/2$ exponents for Mott regime data, than it is in the ES regime.

The linearity can be tested by looking at the deviation from the linear fitted line for different exponents. This is done in Fig. 5.10d and Fig. 5.10c. It is difficult to draw solid conclusions because the ES regime data only becomes linear at low temperatures. From Figs. 5.10d and 5.10c it is arguably possible to see that 1/2 fits the data better than 1/3.

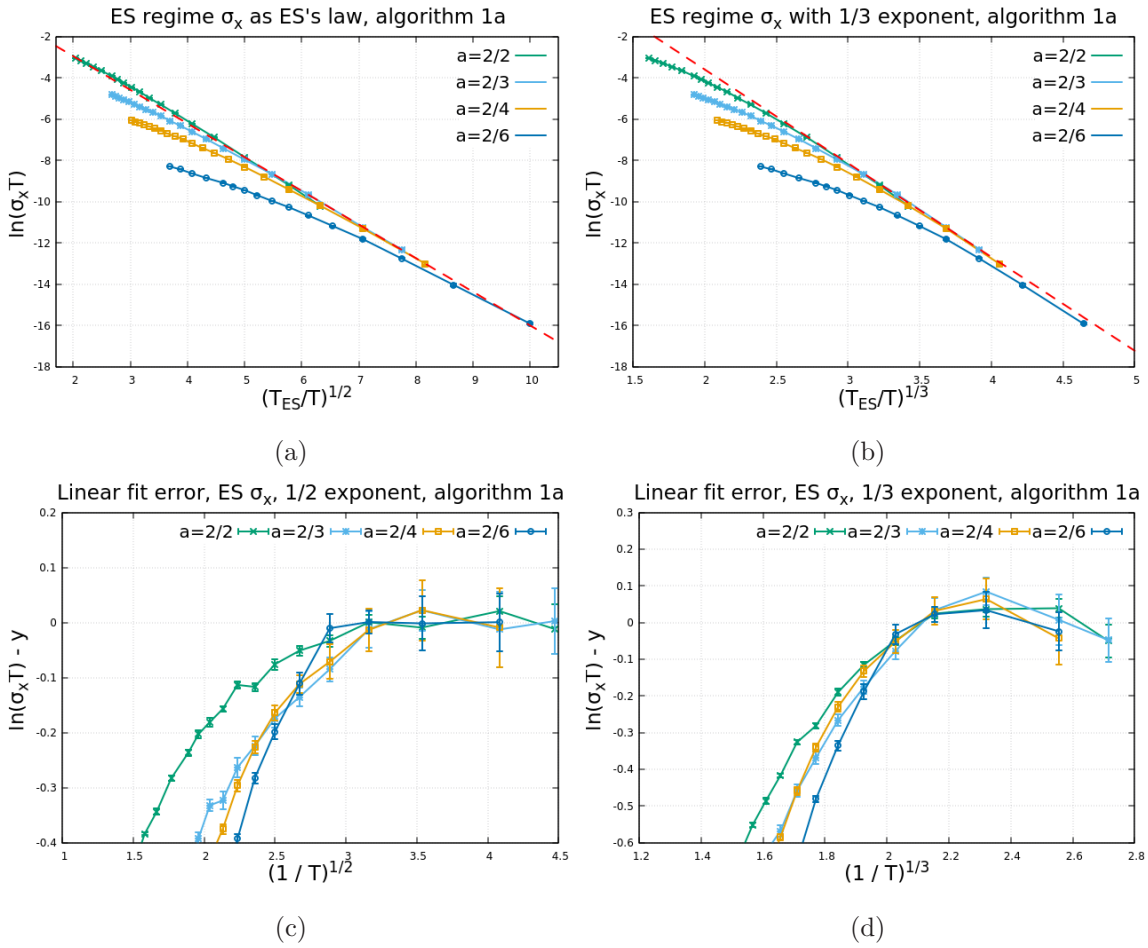

Figure 5.10: Temperature dependence of ES regime simulated σ_x using algorithm 1a. (a) tests with ES's law and (b) with 1/3 exponent. The difference between the linear fitted line and the simulated σ_x using exponents 1/2 (c) and 1/3 (d). Exponent 1/2 arguably fits the data better.

5.1.4.3 Algorithm 2

Fig. 5.11a shows the simulated ES regime σ_x simulated by algorithm 2 tested with ES's law. Fig. 5.11a shows close to linear behavior for only very small temperatures. Smaller a require even lower temperatures before linear regime appears.

The slopes from Fig. 5.11a are presented in table 5.3. Comparing with algorithm 1a, algorithm 2 produces the same results just as in the Mott regime.

5.1.4.4 Algorithm 1b

Fig. 5.11b shows the σ_x simulated by algorithm 1b in the ES regime. The data in Fig. 5.11b shows a linear behavior at low temperatures. Small a data seems to converge to the linear

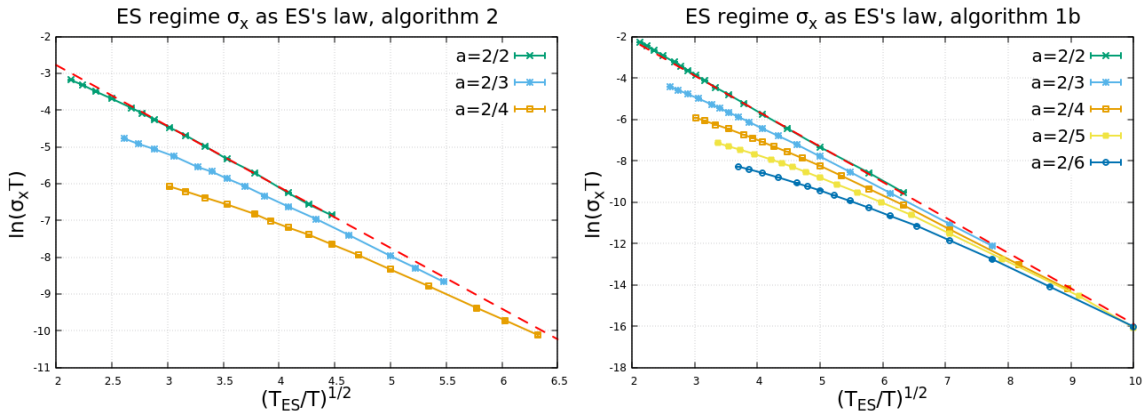

(a) (b)

Figure 5.11: Temperature dependence of simulated ES regime σ_x for algorithms 2 (a) and 1b (b). The data is tested against ES's law and seem to follow it. The temperature range in (a) is limited by the speed of algorithm 2, but the results are very similar to that of algorithm 1a over the same temperature range.

behavior of the others, but only outside the simulated temperature range.

The slopes from Fig. 5.11b are noted in table 5.3.

5.1.4.5 Measured ES slopes

Table 5.3 presents the slopes of the curves in ES regime data fitted to ES's law for the different algorithms. Slopes for $a = 2/6$ data is omitted from table 5.3 because too few data points are available at low temperatures to see if there is a linear behavior or not. As with Mott's law in section 5.1.3.5, the slope slopes in Figs. 5.10a, 5.11a and 5.11b should be constant $C_{\mathrm{ES}}^{1/2}$ and independent of a. Just as in the Mott regime with the lattice model, a systematic a dependence is measured in the constant $C_{\mathrm{ES}}^{1/2}$. This a dependence very likely has the same cause as that of the Mott regime; it is a consequence of using the lattice model. We don't have an algorithm that implements Coulomb interaction with randomly positioned sites. Results of ES regime σ_x from such an algorithm would likely measure C_{ES} independent of a.

As observed in the Mott regime, algorithm 1a and algorithm 2 measure almost the same slope for the ES regime when measurements are made using the same temperature range. There is a small discrepancy for $a = 2/4$, the two algorithms are 0.02 outside the range of each-other's error range. The difference is so small, and the data seems to follow the same trend, and they were very close for the Mott regime, so it is acceptable and it is possible to say that the two algorithms also produce the same results for the ES regime.

Likewise for the Mott regime, the slopes measured from algorithm 1b are smaller than that measured from algorithm 1a. This has the same explanation. Three-site jumps change the network properties, lowering the critical percolating concentration n_C. The ES temperature constant is $T_{\mathrm{ES}} = C_{\mathrm{ES}}/a \propto n_C$. Therefore lowering n_C lowers the measured C_{ES}.

Table 5.3: Value of $C_{\mathrm{ES}}^{1/2}$ measured from ES regime generated temperature dependence of σ_x for all three algorithms. The specified temperature range is the range used for making the measurement of the slope.

a	Algorithm 1a		Algorithm 2	Algorithm 1b
	$T \in (0.04, 0.24)$	$T \in (0.12, 0.24)$	$T \in (0.12, 0.24)$	$T \in (0.04, 0.24)$
2/2	2.49 ± 0.01	2.38 ± 0.01	2.36 ± 0.03	2.42 ± 0.01
2/3	2.25 ± 0.02	2.06 ± 0.01	2.08 ± 0.02	2.18 ± 0.01
2/4	2.16 ± 0.03	1.95 ± 0.01	1.90 ± 0.02	2.08 ± 0.03

5.1.5 Hills method results

Hills method can be used to extract the exponent the from the data itself. The results of doing so on σ_x measured for both regimes using algorithms 1a and 1b is presented in table 5.4. The method is not applied to algorithm 2 as only low temperature points are usable for this method. As algorithm 1a gave the same results as algorithm 2 for measured temperature constants, we expect algorithm 2 to measure the same exponents as algorithm 1a.

There is a consistent behavior of the slope to decrease with decreasing a. This is in disagreement with experimental works [4]. The exponents in table 5.4 do not fall exactly on 1/3 for Mott regime and 1/2 for ES regime. For the Mott regime the values lie mostly around 0.40 while for the ES regime they lie between $0.60 - 0.40$. The measured exponent is systematically decreasing with decreasing a. This could be an effect of using the lattice model.

The measured ES regime exponent are consistently larger than that of the Mott regime. This is in agreement with theoretical predictions.

Table 5.4: Exponent measured from data using Hills method detailed in section 2.3.4. Only temperatures $T \leq 0.16$ are used for making the exponent estimate.

	Mott regime		**ES regime**	
a	Algorithm 1a	Algorithm 1b	Algorithm 1a	Algorithm 1b
2/2	0.41 ± 0.01	0.53 ± 0.02	0.56 ± 0.01	0.59 ± 0.01
2/3	0.40 ± 0.01	0.39 ± 0.01	0.49 ± 0.01	0.50 ± 0.01
2/4	0.38 ± 0.01	0.38 ± 0.01	0.46 ± 0.01	0.47 ± 0.01
2/6	0.38 ± 0.01	0.33 ± 0.01	0.41 ± 0.01	0.42 ± 0.01

5.1.6 x-current generation map

A map showing x-current generated in a sample is presented in Fig. 5.12. The map clearly shows that current is being generated along many paths that connect the left and right sides of the sample. The random resistor network (discussed in section 2.3.1) is solved using the assumption that current only travels through a single percolating path. It means that under the conditions in Fig. 5.12, that assumption is very wrong. There is a large amount of current traveling through the sample using many paths.

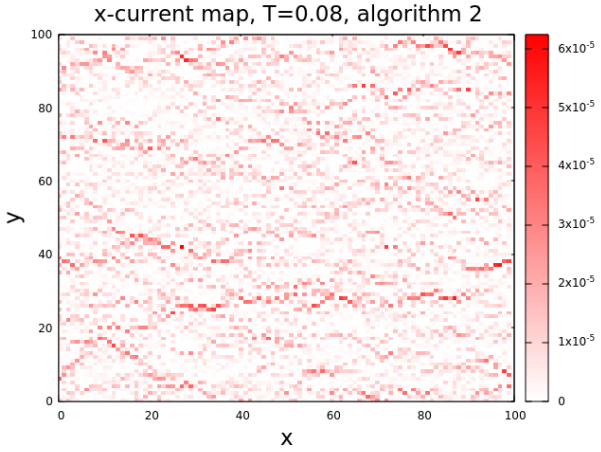

Figure 5.12: x-current generation map of a simulation sample. The simulations are done at $T = 0.08$ with $E = 0.016$. The electric field is aligned in the positive x-direction (to the right). The color red represents current traveling to the left. The map is made using $5 * 10^7$ jumps, ignoring the first 10^6.

5.1.7 Comparison with other simulations

There are not many published articles that study the values of T_0 for either the Mott or ES regime using KMC simulations. To our knowledge there are no studies done on the conductivity data collapse when using different localization lengths.

Ref. [30] use a parallelized version of the rejection algorithm to simulate ES regime VRH conductivity using the lattice model. Their result using localization length $a = 2/2$ is $C_{\mathrm{ES}} = 6.2$. They also find $\sigma_0 = 2.7/T$. Using algorithm 1a with $a = 2/2$, we find $C_{\mathrm{ES}} = 6.20 \pm 0.05$ and $\sigma_0 = (2.7 \pm 0.4)/T$). The results from algorithm 1a are in perfect agreement with that of Ref. [30]. Ref. [30] do not look at any variations in localization length.

In contradiction to the results of Ref. [30] and of this thesis, Tsigankov and Efros find $C_{ES} = 5.8$ using $a = 2/2$ in Ref. [32]. Tsigankov and Efros use the dynamic KMC algorithm on the lattice model as described in Ref. [32], but use a different acceptation function. They do not add any uncertainties to their measurement, so it is possible their C_{ES} at $a = 2/2$ is consistent with Ref. [30] and of this thesis for the lattice model. They also measure $C_{Mott} = 13.0/g(\mu)$ using Mott regime simulations.

The DOS $g(\epsilon)$ in the Mott regime is determined by the randomly assigned disorder potential ϕ. As ϕ is a uniformly distributed random number in $(-1, 1)$, the Mott DOS is a constant $g(\epsilon) = 0.5$. Using this DOS and the value of C_{Mott} at $a = 2/2$ from table 5.2 measured by algorithm 1a, we find $C_{\mathrm{Mott}} = (6.18 \pm 0.02)/g(\mu)$.

The difference in C_{Mott} measurements between our thesis and that of Ref. [32] is puzzling. The only difference should be acceptation criteria for jumps, which should not have such a significant impact on C_{Mott}.

Additionally it is unexpected that the measured value of $g(\epsilon)C_{\mathrm{Mott}}$ and C_{ES} are the same. For $a = 2/2$ we found $g(\epsilon)C_{\mathrm{Mott}} = 6.18 \pm 0.02$ and $C_{\mathrm{ES}} = 6.20 \pm 0.05$. In fact, using the

measured values of C_{Mott} and C_{ES} found in tables 5.2 and 5.3, $g(\epsilon)C_{\text{Mott}}$ and C_{ES} are found to be consistent, or very close to consistent, with one another for all values of a.

5.1.8 Concluding thoughts on σ_x results

It is observed to be difficult to determine if the data fits Mott or ES's exponent better. It seems to be easier to tell that Mott data does not follow ES exponent than it is the other way around. The data is only expected to follow VRH law at low temperatures, and it was seen that ES regime σ_x starts to follow ES's law at a lower temperature than when Mott's regime σ_x starts to follow Mott's law. As such, even lower temperatures are needed for the ES regime to study the section of σ_x that should be linear.

However plotting ES data with T_{Mott} or vice versa fails to produce any sort of data collapse. This can be seen in Fig. B.3. The lack of collapse makes it clear that Mott regime data needs T_{Mott} and ES regime data needs T_{ES}. Therefore while difficult to determine the correct exponent, the correct a dependence of the temperature constant is a good tool to distinguish between the regimes. This holds for all algorithms.

The exponents measured using Hill's method contain systematic a dependence, but the exponent of ES regime is always larger than that of the Mott regime in agreement with VRH laws. The exact values are not as they theoretically should be, but Hill's method is only an approximate and it is not expected to get exact results.

Algorithm 1b seems to work at producing σ_x almost in accordance with the VRH regimes. While the data only collapses for small a, large localization lengths produce nice looking curves themselves. The three-site jumps change the percolating network properties and therefore change the temperature constant. These properties of algorithm 1b need to be considered when analyzing results of Hall currents and conductivity.

There are many crude approximations and assumptions used to derive the VRH laws. For instance an assumption that goes into the derivation of Mott's and ES's law is that $na^d \ll 1$, where n is the concentration and d is the dimension. This assumption is clearly not correct in these simuations, the localization lengths used are too large. Additionally an assumption about current only traveling through the single percolating path is made to solve the random resistor network. This is also clearly not the case, as seen in Fig. 5.12. These assumptions do cause large impacts on simulation results. The lattice model however does. Using the lattice model, the simulated conductivity does not collapse to the universal Mott's or ES's law curve for different localization lengths. This is however achieved for the Mott regime using sites with random positions. This shows that the assumption of positional disorder is necessary for the conductivity to follow VRH laws closely.

Based on the results of this section, it is possible to conclude that the KMC algorithms are able to simulate both the Mott and ES VRH conductivity in accordance with known VRH laws. There is a defined Coulomb gap (see Fig. 5.9) that occurs only when dynamic electron-electron interaction is considered. We do find that it is possible to distinguish between the regimes by the dependence of the temperature constant on a. This can be used when studying results of Hall conductivity for the different regimes. Importantly we also find that the lattice model impacts measurements of VRH regime constants C_{Mott} and C_{ES}. A consequence of using the

lattice model is that C_{Mott} and C_{ES} have systematic a dependencies. This will be important when studying the Hall conductivity, as the same property should be present there.

5.2 Current and conductivity in the y-direction

The model used in simulations uses periodic boundary conditions. As such, the Hall effect causes no charge buildup on material boundaries. And there is no transverse electric field to measure. Instead the Hall effect is measured through the accumulated charge, current, in the y-direction, when there is an electric field in the x-direction and a magnetic field in the z-direction.

This section covers the properties of the accumulated charge in the y-direction, when an external magnetic field is present. Positional disorder simulations will *not* be covered in this section. We do not have an algorithm available that can be used in this thesis to simulate Hall conductivity with positional disorder. Only the lattice model will be covered. As algorithm 1a does not consider any magnetic fields, it will also not be covered in this section.

As with the longitudinal conductivity, the dependence of the Hall conductivity σ_H on electric field needs to be studied. Additionally the dependence on magnetic fields needs to be known. Then, the temperature dependence of the σ_H can be tested to find the function form that best fits the simulated results.

5.2.1 Accumulated charge in y-direction

The accumulated charge in the y-direction as function of time is plotted in Fig. 5.13 for high and low temperature, for algorithms 1b and 2. Fig. 5.13a shows high temperature accumulated charge in the y-direction for algorithm 2. The behavior is close to linear, as with the x-direction but with more spread. Comparing Figs. 5.13a and 5.1a, it appears the y-direction current varies more between samples. At the lower temperature, see Fig. 5.13b, the behavior is much less linear and the difference between samples is large. Still there is a clear favored direction for the current.

The high temperature case for algorithm 1b (Fig. 5.13c) looks similar to the algorithm 2 result. Perhaps algorithm 2 is more linear and has less pronounced fluctuations in time. The lower temperature case in Fig. 5.13d is much more difficult to analyze. The behavior is somewhat linear, but with large time fluctuations. The spread between samples is also large, one sample is accumulating charge in the opposite direction to the others. Still, the data in Fig. 5.13d is going more up than down.

The large difference between samples indicates that the correlation length for the network of conduction paths is larger for σ_H than σ_x, in agreement with predictions from Ref. [7]. It seems that the y-current produced by algorithm 1b has a larger correlation length than algorithm 2.

It does also seem like the two algorithms produce j_y with different correlation lengths. Looking at Figs. 5.13b and 5.13d, for the same external parameters algorithm 1b produces j_y with much larger differences between samples than algorithm 2.

As observed in for j_x, decreasing a leads to larger differences between samples and larger

fluctuations in time. Since the correlation length for $j_y >$ the correlation length for j_x, these effects are expected to also be larger. Therefore the range of localization length a that can realistically be studied with meaningful results is smaller for Hall properties.

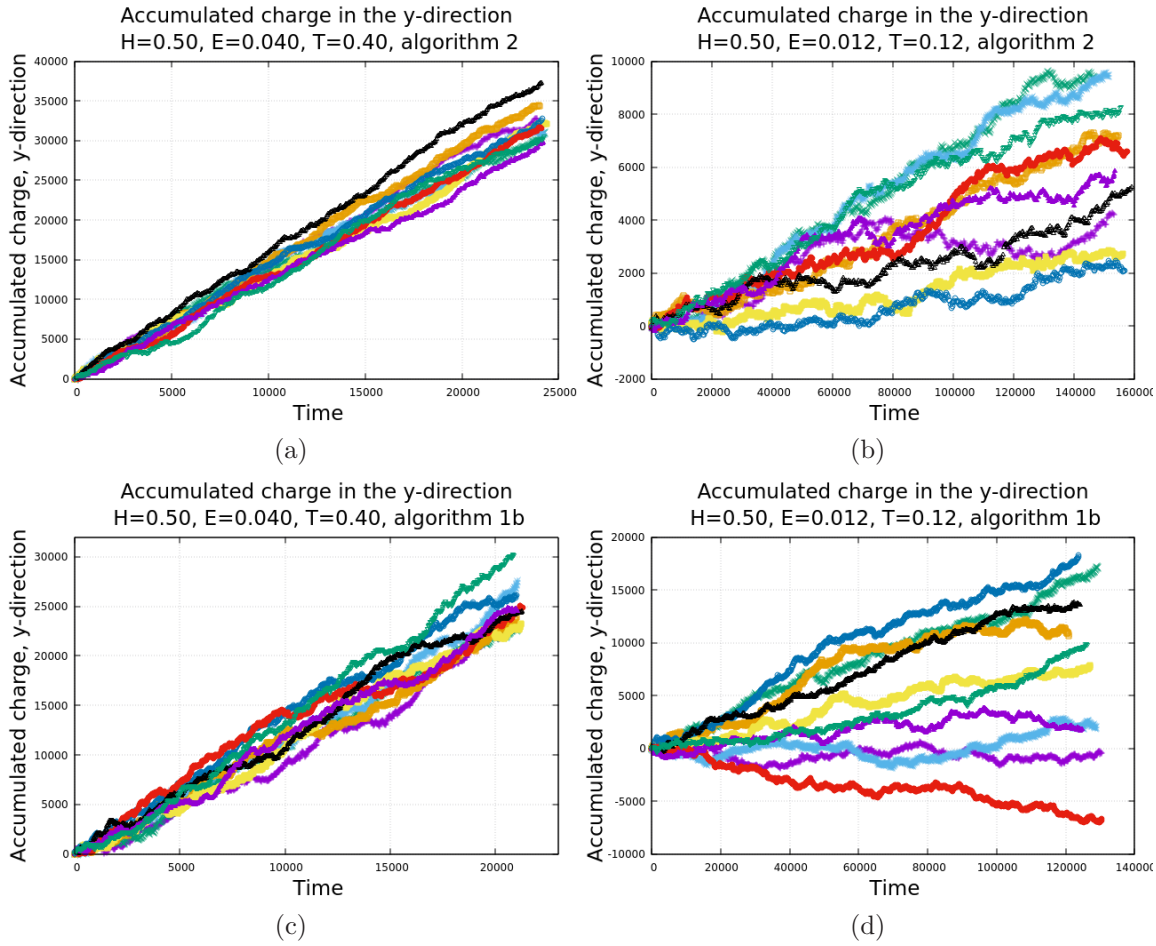

Figure 5.13: Accumulated charge in the y-direction measured in simulations as function of time for 10 different samples. (a) and (b) show the high and low temperature y-current simulated by algorithm 2. And (c) and (d) show the high and low-temperature y-current simulated by algorithm 1b.

We see that the accumulated charge behaves in similar manner for both x and y-directions. It is apparent that the conductivity in the y-direction experiences larger variation from sample to sample than the longitudinal conductivity. But it is possible to conclude that the algorithms produce a current in the y-direction.

If either H or E is set to zero then the accumulated charge in Fig. 5.13 loses it's systematic behavior and looks more like random noise. This is the expected behavior for an algorithm simulating Hall current.

5.2.2 Dependence on electric field

The dependence of σ_H on E is studied in this section. The results using both algorithm 1b and algorithm 2 are presented in Fig. 5.14. The Hall conductivity σ_H has a close to constant

behavior for E. Using small electric fields does however produce large fluctuations in σ_H for both algorithms.

Comparing Figs. 5.2a and 5.14a, it is possible to see that the behavior of σ_H from algorithm 2 is very similar to the behavior of σ_x produced by algorithm 1a. σ_H seems to be constant for small E, and slowly increasing for large E. Likewise for algorithm 1b, simulated σ_x and σ_H have similar dependence on E (see Figs. 5.2b and 5.14b).

It appears that σ_H shows a constant behavior for a larger range of electric fields than σ_x does. This can be observed for both algorithms. The result of this is that perhaps it will be possible to use larger electric fields to study σ_H, than what was possible for σ_x, while still simulating Ohmic behavior. This becomes very useful, as the spread of σ_H between samples is much larger than that of σ_x, and using larger E allows for more precise measurements. Using $E = T/10$ as for σ_x should guarantee Ohmic conductivity, but it is likely possible to use larger fields to reduce the uncertainty. From Fig. 5.14 it can be argued that Ohmic electric fields can be even larger for algorithm 1b than for algorithm 2. This will be tested further later.

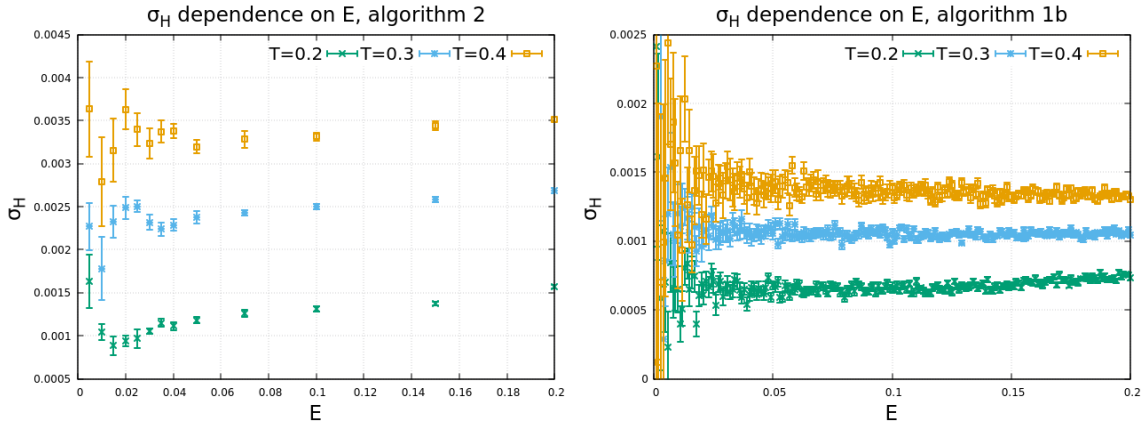

(a) (b)

Figure 5.14: y-current (a,c) and Hall conductivity (b,d) and its dependence on applied electric field for algorithm 1b (top row) and algorithm 2 (bottom row). The behavior of j_y is linear for both algorithms, and the behavior of σ_H has slight differences between the algorithms. All figures use $H = 0.5$.

5.2.3 Dependence on magnetic field

Using the electric field $E = T/10$ for $T = 0.2, 0.3, 0.4$, the dependence of σ_H/H on H is simulated for $H \in (0, 1)$. The results are plotted in Fig. 5.15 for both algorithm 1b and 2. The two algorithms produce similar results.

The behavior of σ_H/H in Fig. 5.15 is constant for small-medium H, but decreasing for large H for both algorithms. There are large fluctuations for in σ_H/H when H is very small. This is observed for both algorithms, but the decrease in σ_H/H is more significant when $T = 0.4$ in algorithm 1b than in algorithm 2 for the same temperature.

It seems the dependence of σ_H/H on H is similar to the dependence of σ_x on E. This is the expected result and indicates that the algorithms are able to simulate a normal working Hall

effect.

In the initialization process of algorithm 1b, the transition rate Γ^T_{ikj} is set to zero if $(1 + \mathbf{H} \cdot \mathbf{A}_{ikj}) < 0$ to avoid problems with negative rates affecting the algorithm. What happens if nothing is done to remove these negatives rates is discussed in section D. The results sets an upper bound of $H = 0.5$ for simulations using algorithm 1b.

Negative rates are not a concern for algorithm 2 for the values of H looked at in this project. Algorithm 2 considers Eq. 4.1 in it's entirety, and $\Gamma_{ij} \gg \sum_k \Gamma_{ikj}$ should be true for very small fields. As seen in Fig. 5.14a, very small fields cause large fluctuations in σ_H, and so to produce reliable results larger fields need to be used meaning $\Gamma_{ij} > \sum_k \Gamma_{ikj}$. A small issue is that $\sum_k \Gamma_{ikj}$ falls off more slowly with intersite distance than Γ_{ij}. Therefore jumps with large intersite distances might have $\sum_k \Gamma_{ikj} > \Gamma_{ij}$. For example, using $H = 0.2$ jumps with a distance of 4 units have rates typically $\in (10^{-4} - 10^{-6})$. The size of $\sum_k \Gamma_{ikj}$ might be $0.2 - 10$ times larger than Γ_{ij}. However these jumps are selected only a few times during simulation time such that it should not be an issue. For jumps of length 1, $\sum_k \Gamma_{ikj}/\Gamma_{ij} \approx 0.1$. There are already a lot of approximations put into the algorithm when simulating normal VRH conductivity. The theoretical framework of lightly doped semiconductors is made in the region where $na^{1/2} \ll 1$, but that is clearly not the case for our simulations. Still, the results of section 5.1.1 show that the algorithm does a good job simulating the dynamics. Therefore, we don't expect the requirement $\Gamma_{ij} \gg \sum_k \Gamma_{ikj}$ to strictly required to get results of a VRH Hall effect.

Based on the above arguments and results, we decide to use a constant magnetic field of $H = 0.2$ for the rejection algorithm, algorithm 2. The value of H expected to produce linear behavior should not be temperature dependence as H connects only directly with the distance relationships. For algorithm 1b, $H = 0.4$ will be used for the simulations.

The σ_x dependence on H is studied shortly in section E. The result is that σ_x is largely independent of H, but is slightly increasing for large fields only for algorithm 2. This behavior is not seen in experiments as magnetoresistance takes place and is much more significant. This is not expected to have a meaningful impact on results.

From Figs. 5.14 and 5.15 we see that the simulated j_y has a linear dependence on both E_x and H_z. This is the expected behavior if the algorithm was simulating Hall conductivity. It is a strong indication that the algorithm is working correctly. Additionally, (not shown) the direction of j_y reverses if the sign of either E_x or H_z is reversed.

5.2.4 Sign of the Hall effect

The dependence of σ_H and σ_x on ν (ratio of electrons to sites) is presented in Fig. 5.16. The conductivities are simulated for $\nu \in [0.02, 0.88]$. The longitudinal conductivity σ_x in Fig. 5.16b seems to be completely symmetric about $\nu = 0.5$. The Hall conductivity σ_H in Fig. 5.16a is more noisy, but also seems to be symmetric about $\nu = 0.5$.

When $\nu < 0.5$, holes are the important charge carrier. And when $\nu > 0.5$ electrons are the dominant charge carrier. The result that σ_H is symmetric about $\nu = 0.5$ means that holes and electrons produce Hall current of the same sign, and of the same magnitude. σ_H does not undergo any changes in sign, in agreement with theoretical predictions in section 3.2.2. The

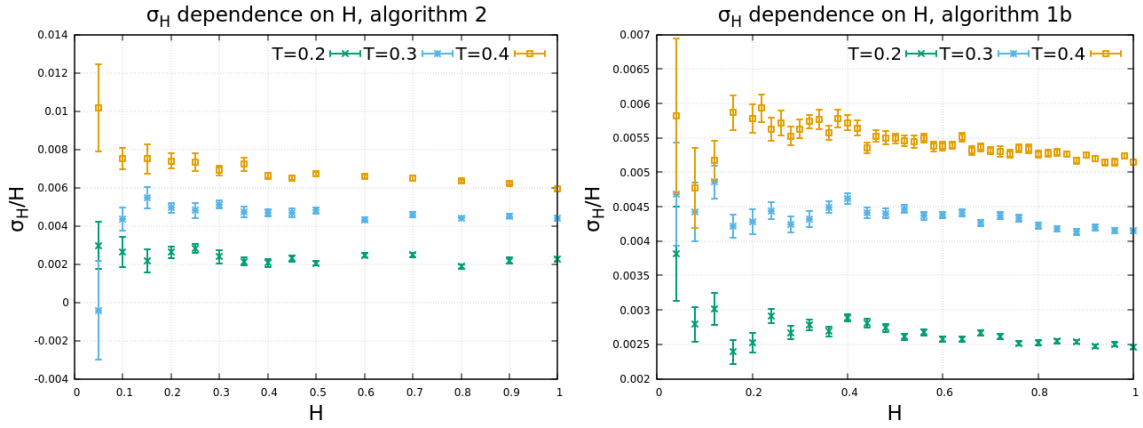

(a) (b)

Figure 5.15: σ_H/H dependence on applied magnetic field for algorithms 2 (a) and 1b (b). σ_H/H shows a constant behavior for small H that is only valid for H up to ~ 0.4 for algorithm 1b and ~ 0.2 for algorithm 2.

simulated σ_H is in the negative y-direction, as expected when defining the vector area to be positive when it is anticlockwise. Changing the vector area definition would switch the Hall effect sign.

The temperature dependence of σ_H should be investigated at constant ν. The absolute error in σ_H is largest for ν around 0.5. But the relative error seems to be independent of ν (not shown). Therefore $\nu = 0.5$ will be used to have results with the largest possible Hall effect.

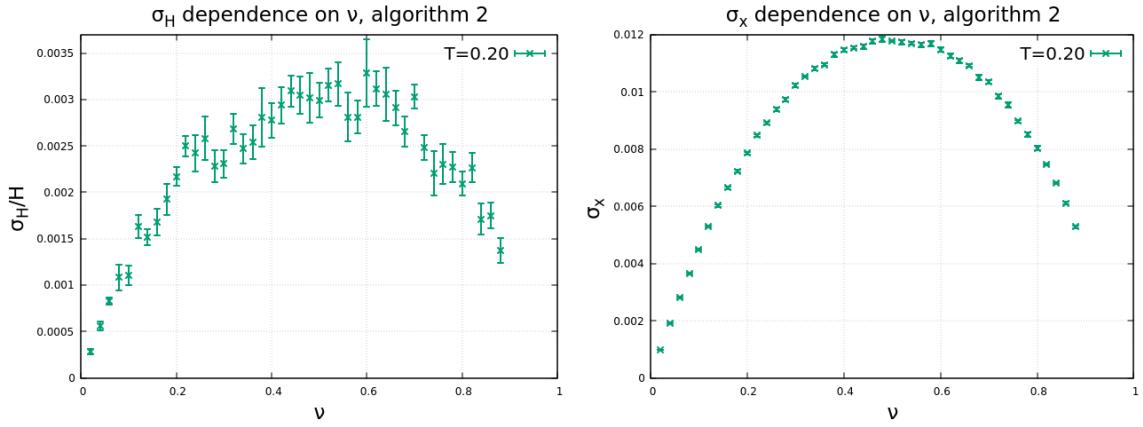

(a) (b)

Figure 5.16: σ_H and σ_x dependence on ν (ratio of electrons to sites in the system). The simulation is done using $H = 0.20, E = 0.04$ and $T = 0.20$.

5.2.5 Mott regime simulations of σ_H

This section covers Mott regime results of the σ_H for both algorithms, one at a time.

5.2.5.1 Algorithm 2

Based on trial and error, we find that using electric fields $E = T/5$ does not produce any non-Ohmic behavior for σ_H. The σ_H simulated using algorithm 2 in this section uses $E = T/5$. Using these electric fields (instead of $E = T/10$) leads to smaller uncertainties and more stable currents.

Based on theoretical and experimental results discussed in section 3.2.3-3.2.5, Mott regime Hall conductivity σ_H is expected to be on the form

$$\sigma_H \propto \frac{a^\gamma}{T^\lambda} \exp\left(-(1+\alpha)\left(\frac{T_{\text{Mott}}}{T}\right)^{1/3}\right). \tag{5.3}$$

Where parameters such as γ and λ need to be determined. Testing the Hall conductivity with different values of λ finds $\lambda = 1$ produces gives the best fit. Setting $\lambda = 1$ gives the Hall conductivity the same temerature dependence as the longitudinal conductivity. Therefore we plot σ_H in the same way that σ_x was plotted earlier, the only difference the $\propto a^\gamma$ dependence. The result is shown in Fig. 5.17a. The figure shows a data collapse similar what was found for σ_x for the same algorithm (see Fig. 5.3a). The best data collapse is found using $\gamma = 1$. The value of γ changes the vertical position of the σ_H curves in Fig. B.8a, it does not affect the slope. See Fig. B.8 for plots with $\gamma = 0$. The value of γ is chosen visually, any value between 0.75 and 1.25 produces a good collapse for Mott regime σ_H.

In section 5.1.3.3 it was seen that adding a^γ to σ_x made it possible to produce a better data collapse for large a. However the data collapse become worse for small a. Since we cannot realistically simulate small a for σ_H, it is not possible to determine if the empirical data collapse 5.17a is valid for small a as well.

The slopes from Fig. B.8a are presented in table 5.6. Similar dependence on a as was found for σ_x slope is observed, but it is more difficult to get accurate measurements of the Hall temperature constant due to more noisy current.

Simulating using $a < 2/4$ does not produce currents stable enough to produce meaningful σ_H over a wide enough temperature range. Therefore only $a \in (2/2, 2/4)$ is looked at here.

5.2.5.2 Algorithm 1b

Observations about the Ohmic region of electric fields E for the Hall conductivity σ_H were made earlier in section 5.2.2. It was seen that the range of electric fields that will produce an Ohmic behaving σ_H is larger than for the longitudinal conductivity. Further yet it was seen that the algorithm 1b σ_H can be Ohmic for even larger E than the algorithm 2 σ_H.

We find a set of "optimal E" that are large enough to produce good measurements while still being Ohmic. The electric fields used to measure σ_H are presented in table 5.5. The method used to determine the Ohmic electric fields was a matter of trial and error. If an electric field is seen to cause non-Ohmic behavior (see last data points of Fig. B.6) then a smaller electric field is tried until Ohmic behavior is found.

Due to the ability to use Ohmic behavior using larger electric fields for algorithm 1b than algorithm 2, it is also possible to simulate σ_H for smaller a. Empirically we find a down to $2/6$

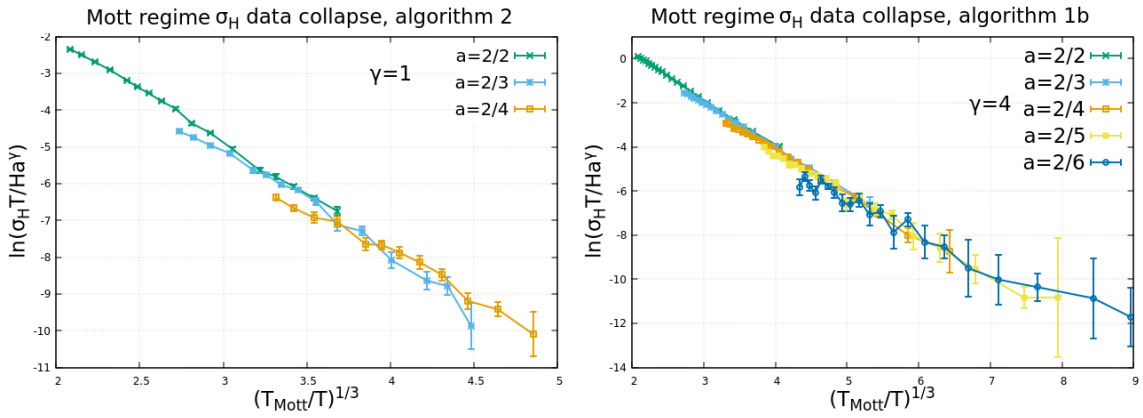

(a) (b)

Figure 5.17: Simulated Mott regime Hall conductivity σ_H empirically fitted to Eq. 5.3 by varying γ for algorithm 2 (a) and algorithm 1b (b). The algorithm's σ_H produce best data collapse with $\gamma = 1$ and $\gamma = 4$ respectively. Note that the value of γ does not change the slope of the curves.

to produce σ_H without too much noise.

Table 5.5: Choice of "optimal" electric fields for different temperatures used for simulating Ohmic σ_H with algorithm 1b with lowest possible uncertainty.

T	E_x
≥ 0.10	0.1
0.08	0.05
0.06 - 0.05	0.015
0.04 - 0.03	0.010

The Mott regime Hall conductivity simulated by algorithm 1b is also expected to follow Eq. 5.3. $\lambda = 1$ gives the best data collapse along with $\gamma = 4$. The result is presented in Fig. 5.17b. All the data curves in Fig. 5.17b fall on top of each other, but with changing slopes. The slopes are presented in table 5.6. There is the same kind of a dependence in C_{Mott} previously mentioned, likely caused by lattice effects.

5.2.5.3 Measured slopes from Mott regime σ_H

Table 5.6 presents the slopes measured from simulated Mott regime σ_H. The slopes feature much more error for the Hall conductivity than they had for the longitudinal conductivity. The uncertainties in table 5.6 represent the parameter error given by the linear regression method. There is another error depending on what data points are and are not included when making measurements. This is demonstrated in Fig. B.7. The linear fit should only be applied to the linear part of Fig. 5.17a, and when there is a lot of noise it becomes difficult to determine what is linear and what is not. Therefore the actual uncertainty is much larger than what is presented in table 5.6.

According to Eq. 5.3, the slope in Fig. 5.17 should be equal to $(1+\alpha)C_{\text{Mott}}^{1/3}$. The uncertainty in measurements is much larger for the Hall conductivity σ_H than it was for the longitudinal conductivity σ_x. Even with these large uncertainties, it seem slike there is a systematic localization length dependence on the measurements in table 5.6. This systematic dependence is very similar as that seen in σ_x when using the lattice model. It therefore most likely has the same origin, lattice effects. This cannot be explicitly confirmed at present, as we do not have an algorithm available that can simulate the Hall conductivity on sites with positional disorder.

Comparing the values of the slopes measured from σ_H in table 5.6 with those measured from σ_x in table 5.2, the Hall conductivity slopes are consistently measured to be larger. This suggests $\alpha > 1$, in accordance with expectations. This aspect will be returned to later when measurements of α are made in section 5.6.

Table 5.6: Value of $(1+\alpha)C_{\text{Mott}}^{1/3}$ measured from simulated σ_H. The temperature range is chosen such as the data seems to be most linear.

a	Algorithm 2	Algorithm 1b
2/2	4.65 ± 0.06	3.45 ± 0.03
2/3	4.5 ± 0.2	3.19 ± 0.05
2/4	4.4 ± 0.3	3.22 ± 0.08
2/5	-	3.06 ± 0.17
2/6	-	2.4 ± 0.2

The $\sigma_H \propto a^\gamma$ dependence was tested and found different values of γ for the different algorithms. Algorithm 2 collapsed with $\gamma = 1$ while algorithm 1b collapsed with $\gamma = 4$. These values will likely be the same if simulations were done on sample with positional disorder, because there were no such changes between the lattice model and the positional disorder samples for the longitudinal conductivity.

How the a^γ factor changes the data collapse for lower data collapse is unknown as results from such simulations have too large uncertainties and fluctuations. It possible that the value of γ chosen only makes the data collapse better for the large a studied, and makes it worse for smaller a.

5.2.6 ES regime simulations of σ_H

This section covers ES regime results of the Hall conductivity σ_H for both algorithms, one at a time.

5.2.6.1 Algorithm 2

The ES regime Hall conductivity is expected to be on the function form

$$\sigma_H \propto \frac{a^\gamma}{T^\lambda} \exp\left(-(1+\alpha)\left(\frac{T_{\text{ES}}}{T}\right)^{1/2}\right). \tag{5.4}$$

Where values of γ and λ do not necessarily need to be the same as they were in the Mott regime. Testing finds $\lambda \approx 1$ to be a good fit, giving the ES regime Hall conductivity the same

as in the Mott regime and of the longitudinal conductivity. Therefore it is plotted in the same manner. The result is shown in Fig. 5.18a. The best data collapse was found using $\gamma = 2$. The data points in Fig. 5.18a feature very large uncertainties. The actual spread of Hall conductivity between samples is the same as in the Mott regime, but in the ES regime σ_H is much smaller. This leads to large relative errors, which are visible in FIg. 5.18a.

The ES regime Hall conductivity collapses for medium and low temperatures in Fig. 5.18a, but this is likely largely due to significant uncertainties. σ_H in Fig. 5.18a appears to be linear up to low temperatures, where it flattens out for all a. This flattening out at low temperatures looks a lot like non-Ohmic behavior. It might be that smaller localization lengths require lower electric fields for the Hall conductivity to be Ohmic. Using smaller electric fields leads to much larger uncertainty, which would make it difficult to draw conclusions.

Linear regression is applied to the linear sections of data in Fig. 5.18a. The values are presented in table 5.7. **Maybe just remove?**

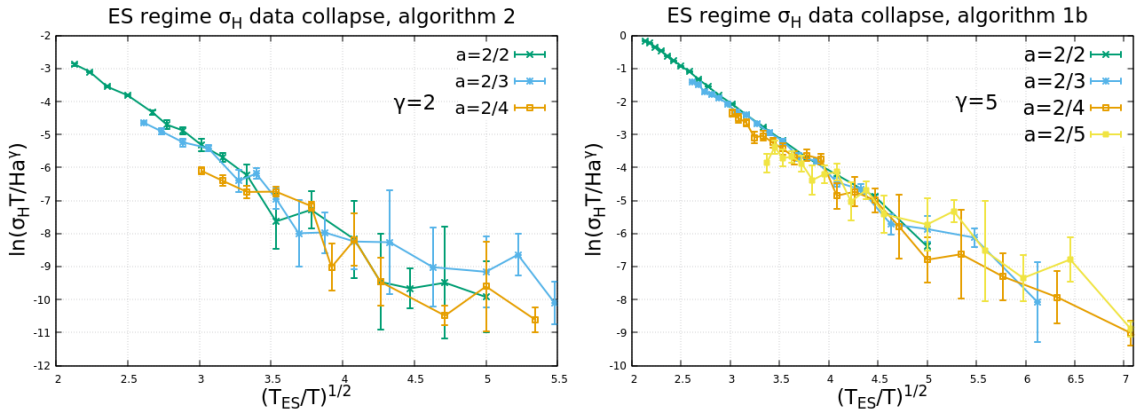

(a) (b)

Figure 5.18: ES regime σ_H empirically fitted to Eq. 5.4 by varying γ for algorithm 2 (a) and algorithm 1b (b). The algorithm's σ_H produce best data collapse with $\gamma = 2$ and $\gamma = 5$ respectively.

5.2.6.2 Algorithm 1b

ES regime σ_H is simulated using algorithm 1b. The results are fitted to Eq. 5.4. The results are shown in Fig. 5.18b. The best data collapse is found using $\gamma = 5$ and $\lambda = 1$. The σ_H curves are very linear for high a, and large and medium temperatures. The curves flatten out at low localization lengths and low temperatures. This flattening out at low temperatures looks like non-Ohmic behavior.

The slopes from Fig. 5.18b are presented in table 5.7 and feature a clear systematic decrease with a.

5.2.6.3 Measured slopes from ES regime σ_H

The slopes from Figs. 5.18a and 5.18b are meaured using linear regression and presented in table 5.7. From a theoretical standpoint, the slope should be $(1 + \alpha)C_{\mathrm{ES}}^{1/2}$. The uncertainties

in measurements are much larger in the ES regime than they were in the Mott regime. The measured σ_H slope varies greatly depending on the temperature range of data points included in the linear regression. For instance the slope for $a = 2/4$ using algorithm 2 varies between 1.0 ± 0.6 and 2.0 ± 0.7. The data points included are chosen visually based on where the results appear linear. Despite large errors it is possible to see a systematic a dependence in measured σ_H slope in both algorithms. This is likely the same lattice effect previously documented.

Table 5.7: Value of $(1+\alpha)C_{\mathrm{ES}}^{1/2}$ measured from ES regime σ_H simulated data.

a	Algorithm 2	Algorithm 1b
2/2	4.04 ± 0.11	3.07 ± 0.03
2/3	2.76 ± 0.16	2.72 ± 0.06
2/4	1.8 ± 0.7	2.39 ± 0.10
2/5	-	2.01 ± 0.10

5.2.7 Hall current generation map

A map of y-current generated in the presence of a magnetic field is presented in Fig. 5.19a. The map is made using Mott regime simulations, there are no visual differences in the ES regime. The figure shows paths of y-current being generated on diagonal paths. The main direction of the electron movement is in the negative x-direction. The red dots in Fig. 5.19a represent electrons moving down, blue dots representing electrons moving up. Fig. 5.19a features a lot of noise, but it is possible to see red diagonals representing paths for electrons to move down and blue diagonals representing paths for electrons to move up. These paths are paths where it is easy for the electron to move either up or down. Fig. 5.19a seems to show that Hall current is generated almost homogeneously throughout the sample. There are some paths where positive Hall current is being generated, and some paths where negative Hall current is being generated.

The theory of Galperin et al. [7] predicts there to be some optimal triangles that generate exponentially more Hall current than others. It should be so dominant that Hall current generated by other triangles is negligible. If that were to be the case in the simulations then Fig. 5.19a should feature one or a few areas with much much more Hall current than others. That does not seem to be the case in these simulations.

The definition of optimal triangles does however require sites to be positionally close to each other in accordance with certain bonding criteria. This aspect is not considered in the lattice model, as all sites are equally spaced. Percolation simulations of VRH Hall effect by Shumilin and Stepina in Ref. [17] use sites with positional disorder, and do not find any evidence of optimal triangles.

5.2.8 Concluding thoughts on σ_H simulations

The simulated Hall conductivity σ_H features more uncertainty than the longitudinal conductivity did. ES regime measurements of σ_H have much more noise than Mott regime σ_H. This makes it difficult to see differences in VRH exponents, whether it should be 1/2 or 1/3. The differences between plots when changing just the exponent is very slight, and with uncertain data it becomes impossibl to see a difference. However the a dependence of T_{Mott} and T_{ES} gives a clear and simple to read difference. Just as it did for σ_x. The Mott regime σ_H is plotted using

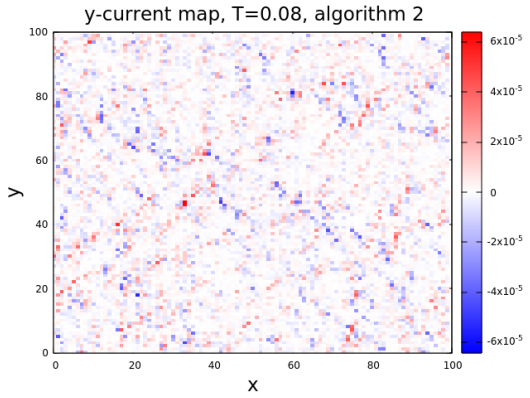

(a)

Figure 5.19: Mott regime Hall current generation map of a simulation sample. ES regime maps show no visual difference. The simulations are done at $T = 0.08$ with $E = 0.016$ and $H = 0.2$. The red current represents current moving in the negative y-direction. The map is made using $5 * 10^7$ jumps, ignoring the first 10^6.

T_{ES} and 1/2 exponent in Fig. 5.20a. It shows no data collapse. Adding a $\sigma_H \propto a^\gamma$ dependence in Fig. 5.20a can improve it, but all three curves will not collapse together. ES regime σ_H is plotted using T_{Mott} and 1/3 exponent in Fig. 5.20b. The figure shows no data collapse, and is very similar to ES regime σ_x plotted in the same manner (see Fig. B.3d). From this it looks like Mott regime σ_H does follow the function form of Eq. 5.3. While much more uncertain, it also looks like ES regime σ_H follows Eq. 5.4.

The uncertainty in measurements is much greater in the ES regime than in the Mott regime for algorithm 2. This implies a large difference in the correlation length of the Hall effect between the VRH regimes. The reason for this is not fully known. The authors of Ref. [17] do not find such large difference in uncertainty between the regimes when using percolation simulations.

The theory of optimal triangles predicts the Hall conductivity to be largely controlled by some key sites in the sample [7]. These combinations of sites would be much more efficient at producing Hall current than other combinations. Therefore the theory predicts large mesoscopic fluctuations in the Hall conductivity. The theory is developed for both the Mott and ES regime, with the same prediction. If the optimal triangle theory is true, there would be large uncertainty in measurements of σ_H. Which is seen, but only in the ES regime. There are no visual differences in Mott and ES regime Hall current maps (in Fig. 5.19a). The homogeneousness was used as an argument to say there are no optimal triangles. Likely the large errors in the ES regime have other causes.

When doing simulations one should always be vary of code or simulation mistakes. It is difficult to determine if an unexected result is interesting or worrying. While nothing wrong can be found in the simulation code, it cannot be ruled out that there might be something wrong with the Coulomb interaction implementation. If this is the case, then likely the mistake lies in either the math or the implementation of Coulomb interaction within triangles (discussed in section 4.2.5).

It was found that $\lambda = 1$ ($\sigma_H \propto T^{-\lambda}$) worked best for both algorithms and both VRH regimes.

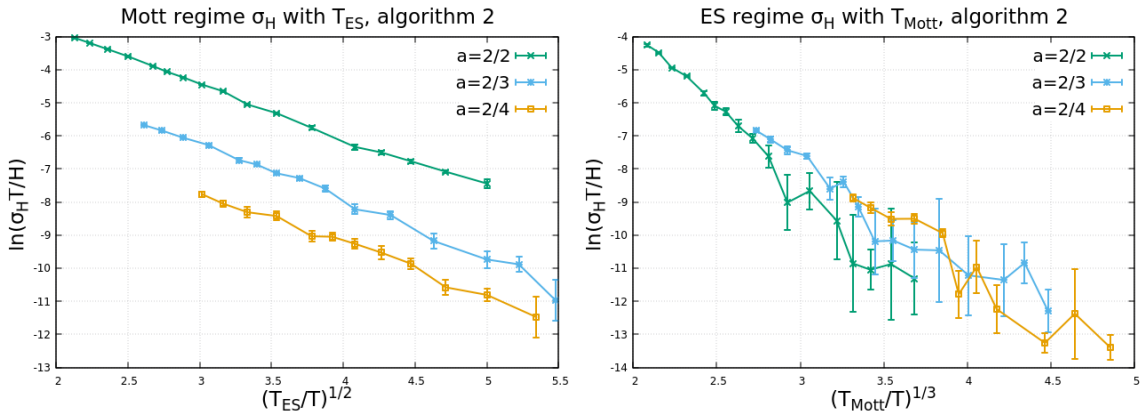

(a) (b)

Figure 5.20: Regime generated σ_H plotted using switched a dependency in T_0. (a) is Mott σ_H plotted with T_{ES} and (b) shows ES σ_H plotted with T_{Mott}. No data collapse is possible for these relations.

The value of γ ($\sigma_H \propto a^{\gamma}$) however changes from algorithm to algorithm, VRH regime to VRH regime. For algorithm 2, $\gamma = 1$ was found for the Mott regime and $\gamma = 2$ for the ES regime. Algorithm 1b σ_H fits best with $\gamma = 4$ in the Mott regime and $\gamma = 5$ in the ES regime. It is interesting that the two algorithms find different γ values. The difference in γ value between algorithms needed for data collapse tells us that the two algorithms simulate Hall conductivities with entirely different properties. The results from algorithm 2 should clearly be trusted more, as it is an exact implementation of magnetic field equations. The trick done to produce algorithm 1b makes it able to simulate a Hall effect that shares many qualities with algorithm 2, but with some different properties.

There is not much data to compare these values with. Most experiments find $\lambda = 0$. However experiments are often severely limited in temperature range which makes it difficult to see any difference between $\lambda = 0$ or $\lambda = 1$. Percolation simulations in Ref. [17] find $\lambda = 1$, in accordance with present results. Ref. [17] is the only reference we have for the value of γ. They find $\gamma = 2$ in both Mott and ES regime simulations, and also on experiments of arrays of quantum dots.

Limitations of the lattice model affect simulations in the localization length dependence. It is possible that the value of γ would change for simulations done on samples with positional disorder. Longitudinal conductivity effectively had $\sigma_x \propto a^{\gamma_x}$ with $\gamma_x = 0$. There were no differences in γ_x between the lattice and random sample model.

In this section it was seen that the algorithms 1b and 2 do produce systematic Hall conductivity in presence of magnetic fields. In the Mott regime the Hall conductivity followed the same general function form as the longitudinal conductivity. In the ES regime the uncertainty became very large and it became difficult to determine the behavior of the Hall conductivity. Still it seems like the ES regime σ_H has similar behavior as ES regime σ_x.

5.3 Hall mobility

In this section we cover the behavior of the Hall mobility $\mu_H = \sigma_H/\sigma_x H$. As will be seen, the uncertainty in Hall mobility is quite large, making it difficult to directly measure the slope as done for σ_x and σ_H.

5.3.1 Algorithm 2

According to the VRH laws for longitudinal conductivity, and Eqs. 5.3 and 5.4, the VRH Hall mobility should be on the form

$$\mu_H = \frac{\sigma_H}{\sigma_x H} \propto \frac{a^\gamma}{T^{\lambda-1}} \exp\left(-\alpha \left(\frac{T_0}{T}\right)^p\right). \tag{5.5}$$

Where $T_0 = T_{\text{Mott}}$ and $p = 1/3$ represents the Mott regime and $T_0 = T_{\text{ES}}$ and $p = 1/2$ represents the ES regime. The values of λ and γ have already been measured by studying the Hall conductivity in section 5.2.

Mott regime μ_H simulated by algorithm 2 is presented in Fig. 5.21a. The figure uses $\gamma = 1$, as found in section 5.2. The curves collapse well, but with large fluctuations at low temperatures.

Fig. 5.21b shows ES regime μ_H. This figure uses $\gamma = 0$, in contradiction with $\gamma = 2$ found earlier. Using $\gamma = 0$ gives the best collapse for μ_H. Using $\gamma = 2$ instead does not make the σ_H curves overlap. That result can be seen in Fig. B.10a. This inconsistent measurement of γ is strange. It can be interpreted as the function form of the simulated ES regime σ_H not following Eq. 5.4. If it did, then the same γ value should be needed for a data collapse.

Measurements of the Hall mobility slopes from Figs. 5.21a and 5.21b are presented in table 5.8. Measurements are relatively easy to make in the Mott regime. The fluctuations are not too large. In the ES regime however the fluctuations are very large. This makes measurements precise measurements impossible. An attempt is made using only the data points in the seemingly linear regions of μ_H at high temperature. The results are presented in table 5.8, but the fluctuations are too large for them to be reliable.

5.3.2 Algorithm 1b

Calculating the Hall mobility requires both the Hall and longitudinal conductivities. Algorithm 1b found a different set of electric fields (see table 5.5) to produce Ohmic behaving σ_H than that of σ_x. The electric fields used for σ_H therefore simulate non-Ohmic σ_x. As the function form Eq. 5.5 is developed using Ohmic assumptions, it is necessary to compare Ohmic σ_H with Ohmic σ_x. Therefore σ_H with the "optimal" electric fields will be combined with σ_x using standard $E = T/10$ electric fields to calculate the Hall mobility. The actual impact of doing this is not significant, but it does produce more linear behaving curves and measurements with smaller uncertainty.

When studying the longitudinal conductivity simulated by algorithm 1b, it was found that the data collapse using standards Mott's law did not work very well for large a. An empirical a^{γ_x} proportionality to Mott's law σ_x. Using $\gamma_x = 2$ the data collapse improved for large a, but became worse for small a. The result can be seen in Fig. 5.7a.

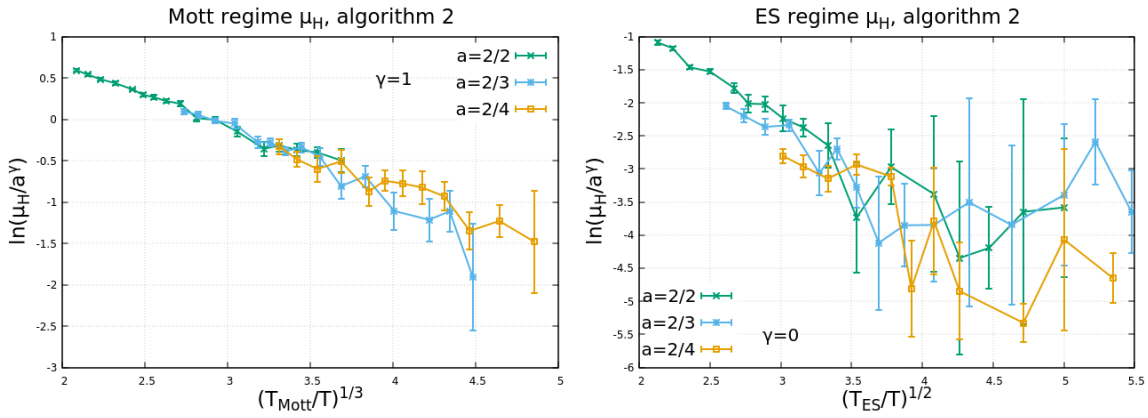

(a) (b)

Figure 5.21: Mott (a) and ES (b) regime Hall mobility μ_H simulated by algorithm 2. Each regime μ_H is plotted as the respective regime law given by Eq. 5.5.

If the longitudinal conductivity σ_x simulated by algorithm does have an a^2 proportionality, then it should reflect in the Hall mobility as $\mu_H \propto \sigma_x^{-1} \propto a^{-\gamma_x}$. The value $\gamma = 4$ was found previously when studying the Hall conductivity. Using these parameters μ_H is plotted in Fig. 5.22a. The result does not show the data collapse expected. The μ_H curves for different localization length do not fall on top of each other. The $a = 2/3$ curve lies on top of the $a = 2/2$ curve, which does not look right considering all the previous results. Tweaking with other values of γ and γ_x we are unable to find a data collapse with any significant improvement from 5.22a.

No empiric $\sigma_x \propto a^{\gamma_x}$ dependence was needed in the ES regime for algorithm 1b. ES regime Hall mobility is plotted in Fig. 5.22b. The figure uses $\gamma = 2.5$, the one that gave the best visual data collapse.The value of γ found from ES regime σ_H using algorithm 1b was $\gamma = 5$. Using $\gamma = 5$ does not produce anything resembling a data collapse. That result is shown in Fig. B.10b. The inconsistent value of γ likely means the simulated μ_H and σ_H do not follow Eqs. 5.5 and 5.4 closely in the ES regime.

Measurements of Hall mobility slopes are made and presented in table 5.8. The data features large fluctuations, making it difficult to make measurements. Only the seemingly linear section for high-medium temperatures are included in the linear regression.

5.3.3 Measured Hall mobility slopes

Measurements of Hall mobility slopes are presented in table 5.8. Measurements are made in the Mott and ES regime using both algorithm 1b and 2. According to Eq. 5.5 the slopes should respectively be equal to $\alpha_{\text{Mott}} C_{\text{Mott}}^{1/3}$ and $\alpha_{\text{ES}} C_{\text{ES}}^{1/2}$. The slopes measured from algorithm 1b is *increasing* with decreasing a for both regimes. In the case of algorithm 2 the slope is not systematically changing in the Mott regime but *decreasing* with decreasing a in the ES regime.

The same systematic localization length a dependence that has been measured previously should also be present here as the lattice model is used. The results show instead different systematic a dependence, and some non-systematic a variations. This indicates that there is

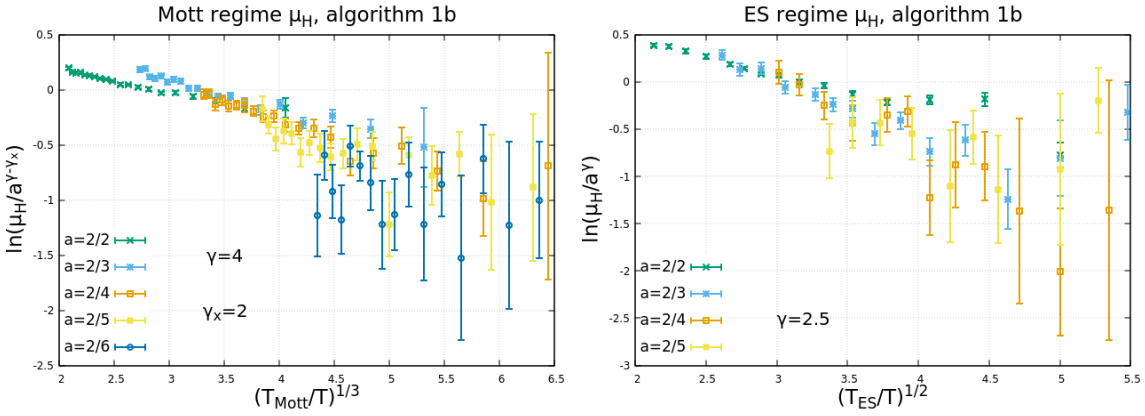

(a) (b)

Figure 5.22: Mott (a) and ES (b) regime Hall mobility μ_H simulated by algorithm 1b. μ_H is plotted as according to Eq. 5.5. The values of γ are the ones that give the best visual data collapse.

also an a dependence in α. This will be studied more in detail later.

Table 5.8: Value of $\alpha_{\text{Mott}} C_{\text{Mott}}^{1/3}$ for Mott regime data and $\alpha_{\text{ES}} C_{\text{ES}}^{1/2}$ for ES regime data, measured by applying linear regression to $\ln(\mu_H)$.

Mott regime		
a	Algorithm 2	Algorithm 1b
2/2	0.74 ± 0.03	0.16 ± 0.01
2/3	0.82 ± 0.11	0.28 ± 0.02
2/4	0.67 ± 0.17	0.35 ± 0.02
ES regime		
a	Algorithm 2	Algorithm 1b
2/2	1.32 ± 0.13	0.50 ± 0.01
2/3	0.7 ± 0.2	0.64 ± 0.06
2/4	0.4 ± 0.3	0.70 ± 0.17

5.4 Relation between longitudinal and Hall conductivity

As explained in section 3.2.3, the Hall conductivity is expected to be related to the longitudinal conductivity as

$$\frac{\sigma_H T^\lambda}{H a^\gamma} \propto (\sigma_x T)^{1+\alpha} \tag{5.6}$$

This relationship can be tested. According to Eq. 5.6, a plot of the LHS vs the RHS in a log-log plot should produce a collapse to a straight line with slope $(1+\alpha)$. The method of plotting the conductivities against one another according to Eq. 5.6 does not assume any a dependence in T_{Mott} or T_{ES}. If the result from such plots is a straight line then it implies that σ_H and σ_x have the same such a dependence. The exponential part of $\sigma_x \propto \exp(-(T_0/T)^p)$ must therefore be the same for σ_H.

In section 5.2 $\lambda = 1$ was found to give a good description of σ_H for all algorithms and VRH regimes. The value of γ varied on the VRH regime being simulated and the algorithm used. The value of γ also varied depending on what was being tested. For instance $\gamma = 2$ was found from looking at σ_H from algorithm 2, but $\gamma = 0$ was better when looking at μ_H for the same algorithm and same VRH regime. This inconsistent γ value should also be reflected when testing Eq. 5.6.

When using algorithm 1b, larger electric fields have been used to study σ_H to reduce the uncertainty in measurements. It was found that this did not cause non-Ohmic σ_H, but would cause non-Ohmic σ_x. As such, considering the theoretical frameworks in section 3.2.3 always consider Ohmic σ_x, it will be more correct to compare σ_H with the "optimal" electric fields (see table 5.5) with σ_x calculated using the normal field sizes $E = T/10$. The impact of doing this is more linear looking curves, with smaller uncertainty but with approximately the same result.

As for algorithm 2, σ_x was previously simulated using $E = T/10$ while σ_H has been simulated using $E = T/5$. The difference in σ_x between using $E = T/10$ and $E = T/5$ is small and will not cause σ_x to become strongly non-Ohmic. Therefore the conductivities σ_H and σ_x simulated by algorithm 2 will be compared both using $E = T/5$.

5.4.1 Mott regime

Studying Mott regime σ_x using algorithm 1b found $\sigma_x \propto a^{\gamma_x}$ to improve the data collapse for large values of a. Inserting this dependency into Eq. 5.6 gives

$$\frac{\sigma_H T}{H a^{\gamma}} \propto \left(\frac{\sigma_x T}{a^{\gamma_x}}\right)^{1+\alpha}. \tag{5.7}$$

Algorithm 2 σ_x does not need any such dependence and effectively has $\gamma_x = 0$.

The conductivity relationship Eq. 5.7 for the Mott regime is plotted in Fig. 5.23. A straight line is indeed produced in Fig. 5.23a using algorithm 2. The straight line holds for all the localization lengths looked at, and only with $\gamma = 1$ and $\gamma_x = 0$. The relationship is plotted in Fig. 5.23b using $\gamma = 4$ and $\gamma_x = 2$ for algorithm 1b. For algorithm 1b the curves do fall approximately on a line, but there are deviations in the gradient underway. The last data points for small a also seem to fall off the line quite systematically. This is likely the effect of using $\gamma_x = 2$, it makes the data collapse worse for small a.

The slopes from Fig. 5.23 are presented in table 5.9. For algorithm 2, all the measured slopes are within the uncertainty of each other, making it possible that the slope is independent of localization length a. For algorithm 1b, it is clear that the slopes change with a, but no systematic a dependence is found.

5.4.2 ES regime

No $\sigma_x \propto a^{\gamma_x}$ was found in the ES regime for any algorithm. Using Eq. 5.7, Figs. 5.24a and 5.24b are created. Algorithm 2 requires $\gamma = -1$ to produce something that follows a straight line. The best result for algorithm 1b is found using $\gamma = 2$, but the data does not follow much of a straight line.

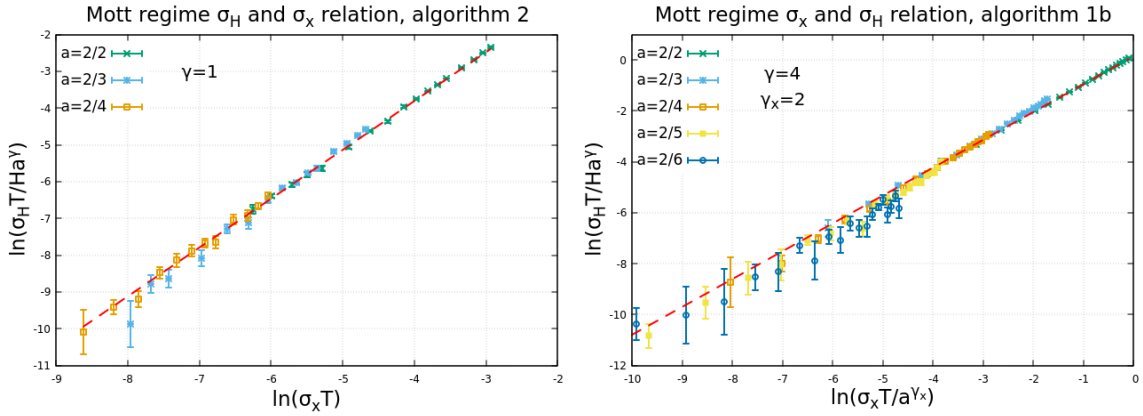

(a) (b)

Figure 5.23: Relation Eq. 5.7 for algorithm 2 (a) and algorithm 1b (b). The subsequent slopes measured are presented in table 5.9.

Table 5.9: Measured slopes from Fig. 5.23. The slope is equal to $(1 + \alpha_{\text{Mott}})$ according to Eq. 5.67.

a	Algorithm 2	Algorithm 1b
2/2	1.33 ± 0.03	1.10 ± 0.01
2/3	1.44 ± 0.07	1.14 ± 0.01
2/4	1.43 ± 0.07	1.22 ± 0.01
2/5	-	1.12 ± 0.05
2/6	-	0.94 ± 0.08

Contrary to previous findings, $\gamma = -1$ is needed for the data produce by algorithm 2 to produce a data collapse. By fitting σ_H earlier it was found $\gamma = 2$ to give best collapse. Using $\gamma = 2$ in Eq. 5.6 produces no data collapse, the results can be seen in Fig. B.4a. Likewise from algorithm 1b, $\gamma = 5$ was found to give a good collapse when studying σ_H. But $\gamma = 2$ seems to give a good collapse in Fig. 5.24b, while using $\gamma = 5$ does not (seen Fig. B.4b.

The slopes in Fig. 5.24 should be equal to $(1 + \alpha_{\text{ES}})$ and are presented in table 5.10. The measured slope for algorithm 2 does not see any systematic a dependence, but the error is very large in the ES regime. All the measured values are within the error of each other. For algorithm 1b the measured slopes have clear changes with a, but it is not possible to see any systematic a dependence.

5.5 Comments on inconsistent γ values

Through Hall mobility and Hall conductivity data collapses as well as the relationship between the conductivities, inconsistent values of γ have been found. The only consistent γ value has been measured in the Mott regime of algorithm 2. $\gamma = 1$ has consistent been found for all data collapses and straight lines from Mott regime algorithm 2. In the ES regime of algorithm 2, γ values of $-1, 0$ and 2 were found for different types of collapses and straight lines. ES regime simulated by algorithm 1b found γ values of $2, 2.5$ and 5.

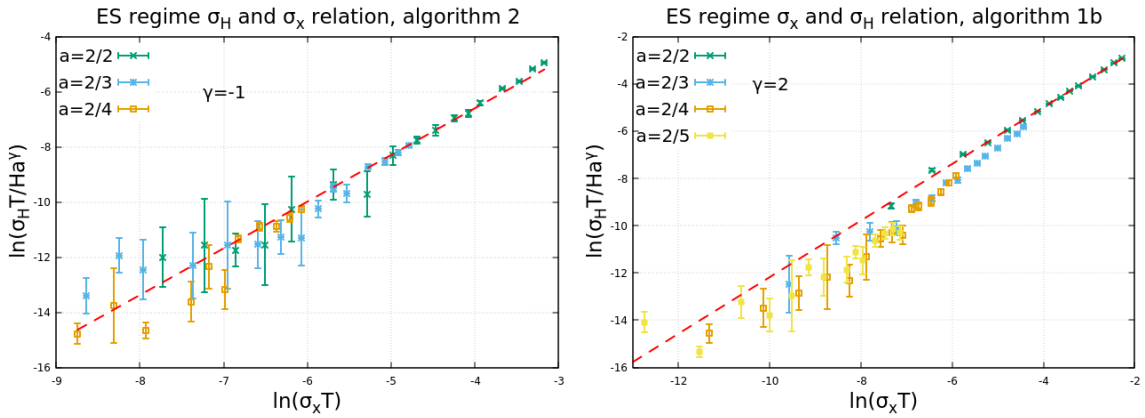

(a) (b)

Figure 5.24: Relation Eq. 5.6 for algorithm 2 (a) and algorithm 1b (b). Both figures use $\gamma_x = 0$. The subsequent slopes measured are presented in table 5.9.

Table 5.10: Measured slopes from Fig. 5.23. The slope is equal to $(1 + \alpha_{\mathrm{ES}})$ according to Eq. 5.6.

a	Algorithm 2	Algorithm 1b
2/2	1.87 ± 0.05	1.16 ± 0.01
2/3	1.8 ± 0.1	1.39 ± 0.04
2/4	2.0 ± 0.3	1.07 ± 0.02
2/5	-	0.92 ± 0.08

Mott regime conductivities simulated by algorithm 1b did find consistent values of γ to produce the best data collapse. But even the best possible data collapse found for the Hall mobility was different from expectations, and the other results.

We are confident in the function form of the longitudinal conductivity for both regimes using algorithm 2. The same cannot be said for algorithm 1b σ_x, as discussed from Fig. 5.7a. These inconsistent γ values are therefore interpreted as the Hall conductivity *not* following Eq. 5.4 in the ES regime for both algorithms, and Mott regime algorithm 1b σ_H *not* following Eq. 5.3. Only Mott regime σ_H from algorithm 2 has been seen to follow Eq. 5.3.

Thus far only algorithm 2 is able to produce σ_H in accordance with theoretical and experimental results, and only for the Mott regime. ES regime results, and Mott regime for algorithm 1b, all show inconsistencies when compared with the theoretical and experimental function form of σ_H.

5.6 Measurements of VRH Hall effect parameter

The Hall effect parameter α gives the relationship of how susceptible the longitudinal and Hall conductivities are to temperature changes. As described in section 4.3.2 there are three methods that will be used to measure the Hall effect parameter α from the data sets. One way is to measure the slopes from both σ_x and σ_H, and use the relationship between them (in Eq.

4.12) to calculate α. Another to compare slopes measured from μ_H and σ_x. And the last is to use the relation Eq. 5.6 to extract α.

These three methods all test the function form of σ_H and σ_x in different ways. If the simulations had measurements with no uncertainty then all the methods should give the same α. We do have uncertainty in measurements, but measurements of α should be consistent. Within the uncertainty of each other. The methods weigh data points of σ_H and σ_x differently, leading to some difference in results. If the α results are inconsistent then it might mean the function form assumed to derive the α measurement methods is wrong or incomplete.

In sections 5.1.1 it was seen that the effect of using the lattice model is the measured values of C_{Mott} and C_{ES} have an extra a dependence. This means that the a dependence in T_{Mott} and T_{ES} in the lattice model does not fit the data perfectly. Instead of inputting an assumption about the a dependence in these temperature constants, it is better to compare them *a priori* of a dependence. This means using measured T_{Mott} instead of C_{Mott} from the longitudinal conductivity when measuring α. All these values have been measured from all conductivities and algorithms and can be seen in table B.1.

Simulating on a lattice as compared to samples with positional disorder affects the measured VRH temperature constants by introducing a dependence on localization length. This is observed for both σ_x and σ_H. If the lattice effects are exactly the same, then measurements of α will be independent of a. If they are different, then α will depend on a. As will be seen, the case is the latter. As we don't have an algorithm to simulate Hall conductivity on samples with positional disorder, we will not be able to give a final result for α.

5.6.1 Mott regime

Mott regime α calculated using the values in tables B.1 and 5.9 is presented in table 5.11. The α_{Mott} measured from algorithm 2 is consistent between the three methods of measurements. The values from all methods is always within the uncertainty of the others. It does seem like maybe α_{Mott} is increasing with decreasing a, but the uncertainty is too large to determine if it is constant or varying.

α_{Mott} measured from algorithm 1b simulation data does experience clear changes with a. The behavior is not consistent and a systematic trend is not possible to find. The results between the different methods are not always consistent with one another.

Measurements from algorithm 2 are consistent whereas the ones from algorithm 1b are not. The fact that there is consistency for algorithm 2 supports the claim that the Hall conductivity follows Eq. 5.3. And it means that σ_H simulated by algorithm 1b likely does not follow Eq. 5.3 as closely as one might have hoped when designing the algorithm. Algorithm 2 has only been used to simulate three values of a, and it is unknown if α_{Mott} measurements would be consistent for lower a.

5.6.2 ES regime

α_{ES} calculated using values in tables B.1 and 5.10 are presented in table 5.12. There is some inconsistency in measured α_{ES} values from both algorithms. There are clear changes in α_{ES} with a, but no systematic behavior is found for either algorithm. As already seen in section

Table 5.11: α_{Mott} measured from algorithms 2 and 1b simulations using different methods. The error is calculated using methods from section 4.3.2.1.

a	**Algorithm 2**		
	μ_H and σ_x	σ_H and σ_x	$\sigma_H T \propto (\sigma_x T)^{1+\alpha}$
2/2	0.33 ± 0.02	0.33 ± 0.03	0.33 ± 0.03
2/3	0.42 ± 0.07	0.38 ± 0.08	0.44 ± 0.07
2/4	0.44 ± 0.08	0.41 ± 0.13	0.43 ± 0.07
a	**Algorithm 1b**		
	μ_H and σ_x	σ_H and σ_x	$\sigma_H T \propto (\sigma_x T)^{1+\alpha}$
2/2	0.08 ± 0.01	0.14 ± 0.02	0.08 ± 0.01
2/3	0.14 ± 0.02	0.14 ± 0.03	0.14 ± 0.01
2/4	0.21 ± 0.02	0.17 ± 0.03	0.23 ± 0.01
2/5	0.14 ± 0.06	0.06 ± 0.05	0.12 ± 0.06
2/6	-0.11 ± 0.09	-0.14 ± 0.07	0.1 ± 0.1

5.2, the uncertainty in measurements from simulated σ_H are large such that it is difficult to draw conclusions about the functional behavior of ES regime σ_H.

Measuring α_{ES} simulated by algorithm 2 for $a = 2/3$ using different methods produces inconsistent results. The inconsistency can be interpreted as σ_H not following Eq. 5.4 closely. There is some behavior not accounted for by the equations. The value of α_{ES} for $a = 2/2$ and $a = 2/4$ are consistent with one another. But with the very large relative uncertainty it does not have to be meaningful if results are consistent with one another.

There are many inconsistencies in α_{ES} when using algorithm 1b. This is not a surprise as σ_x simulated by algorithm 1b was already found to have some extra behavior not accounted for by the VRH laws. And σ_H was found to display similar behavior.

Table 5.12: α_{ES} measured from algorithm 2 simulations using different methods.

a	**Algorithm 2**		
	μ_H and σ_x	σ_H and σ_x	$\sigma_H T \propto (\sigma_x T)^{1+\alpha}$
2/2	0.78 ± 0.09	0.73 ± 0.09	0.87 ± 0.05
2/3	0.52 ± 0.08	0.4 ± 0.1	0.8 ± 0.1
2/4	0.8 ± 0.4	1.0 ± 0.4	1.0 ± 0.3
a	**Algorithm 1b**		
	μ_H and σ_x	σ_H and σ_x	$\sigma_H T \propto (\sigma_x T)^{1+\alpha}$
2/2	0.29 ± 0.01	0.21 ± 0.04	0.16 ± 0.01
2/3	0.41 ± 0.03	0.24 ± 0.05	0.39 ± 0.04
2/4	0.2 ± 0.1	0.13 ± 0.05	0.07 ± 0.02
2/5	0.06 ± 0.06	-0.1 ± 0.1	-0.08 ± 0.08

5.6.3 VRH Hall effect parameter dependence on H

The theoretical studies on VRH Hall effect discussed in section 3.2.3 are developed in the limit of small magnetic fields. Many experimental works [10, 11] measure α to depend on the applied field. Some authors try to extrapolate α to $H = 0$ when presenting a final result [10].

There were some inconsistencies in measurements of α_{ES}, therefore we will only look at how α_{Mott} varies with applied magnetic field.

The dependence of temperature constants on magnetic field measured from Mott regime algorithm 2 simulations is located in table B.3 for $a = 2/2$ and in table B.5 for $a = 2/3$. The tables show that all the temperature constants do depend on magnetic field, and decrease systematically with it.

Before calculations of α are done, let us briefly discuss the appropriate σ_x to calculate with. It was seen earlier that σ_x *increases* with magnetic field for algorithm 2. Theoretical works do not consider any changes to σ_x with the magnetic field. Real materials would experience magnetoresistance effects, and *decreasing* σ_x with magnetic field. As the impact of magnetic fields on σ_x is on a different nature in simulations to experiments and theoretical works, $\sigma_x(H = 0)$ should reflect more on experiments. Both cases will be looked at, with σ_x as function of applied field and with constant σ_x at $H = 0$.

The extrapolation procedure is difficult because there are no theoretical predictions of how α should depend on H. The authors of Ref. [10] assume a linear dependence with decent results. The authors of [11] do not find a linear dependence to fit well with their results, and do not find a way of extrapolating to zero field. The dependence of calculated α_{Mott} for $a = 2/2$ and $a = 2/3$, when considering both σ_x with and without dependence on H is presented in Fig. 5.25.

α_{Mott} has a very clear linear dependence in Fig. 5.25b when $a = 2/2$ and $\sigma_x(H = 0)$ is considered. In the other cases the linear model works well, but it is less clear. Extrapolated results of α_{Mott} to $H = 0$ is presented in table 5.13. As seen, the value of α_{Mott} does not change much whether $\sigma_x(H)$ or $\sigma_x(H = 0)$ is used in calculations.

Table 5.13: Extrapolated α_{Mott} to $H = 0$. Extrapolation is seen in Fig. 5.25.

a	Using $\sigma_x(H)$	Using $\sigma_x(H = 0)$
2/2	0.36 ± 0.02	0.37 ± 0.02
2/3	0.48 ± 0.09	0.45 ± 0.08

5.6.4 Concluding thoughts on VRH Hall effect parameter values

The α parameter was found to vary with localization length in all cases. In the ES regime this was expected as it has already been seen that the function form of simulated σ_H does not follow Eq. 5.4. Therefore the measurements of α have little physical meaning, and are difficult to interpret for the ES regime. The Mott regime simulated by algorithm 2 is the only σ_H that is behaving as predicted by theory. Even so, it experienced variations in α_{Mott} with localization

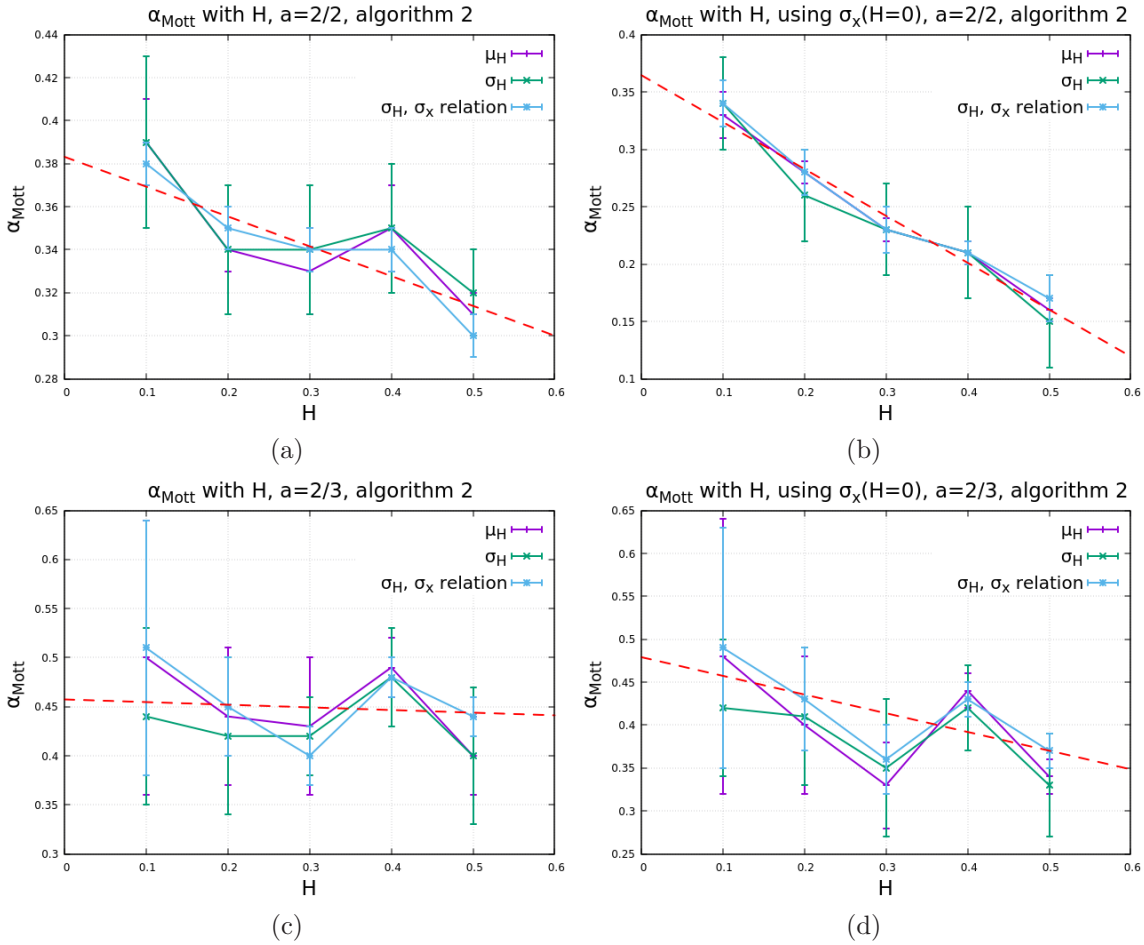

Figure 5.25: α_{Mott} variations with H for $a = 2/2$ (top row) and $a = 2/3$ (bottom row) calculated with σ_x with H dependence (left column) and σ_x at $H = 0$ (right column). The values in the figures are also presented in tables B.2, B.4 and B.6.

length. This is likely caused by lattice effects, as σ_H simulated on sites with positional would most likely converge to a universal curve as it did for σ_x (see Fig. 5.8)

The values of α_{Mott} measured from algorithm 2 generally coincide with experimental values. The measured α_{Mott} lies somewhere between 0.30 and 0.50, same as most experimental results covered in table 3.2. Simulations of σ_H with positional disorder would most likely find an α value somewhere in this range.

By measuring α_{ES} using different methods on the same data set we found results inconsistent with one another. This suggests that σ_H simulated by algorithm 2 is *not* on the function form we have assumed. Therefore whether any values of α_{ES} coincide with any theoretical or experimental results is of little importance. This is in agreement with the inconsistent values found for γ in the ES regime. The inconsistent γ values were interpreted as the function form of simulated ES regime Hall conductivity not following Eq. 5.4.

5.7 Comparison with percolation simulations

The rejection algorithm, algorithm 2, seems to do an excellent job at simulating both σ_x and σ_H in the Mott regime. With the exception of small localization deviations, which are shown to stem from lattice effects, everything is according to theory. Here it is useful to compare with the percolation simulations of Shumilin and Stepina in Ref. [17]. They use sites with positional disorder and do therefore not experience any lattice effects. Their result for Mott regime longitudinal conductivity σ_x seems to have the exact same qualities as found by the KMC algorithm with positional disorder (Fig. 5.8).

The Mott regime Hall conductivity result was also very similar. Here the difference of lattice effects comes in, as that could not be taken care of in this thesis. The value of γ (from $\sigma_H \propto a^\gamma$) was found to be $\gamma = 2$ in Ref. [17], and $\gamma = 1$ in this thesis. The value $\gamma = 1$ was found consistently for all methods used to test σ_H. The lattice only directly affects the simulation through the localization length. Therefore it is not unthinkable that KMC simulations of σ_H using positional disorder would find $\gamma = 2$, or some other γ. But there is also no evidence to explicitly think that.

The percolation simulations of Ref. [17] were also able to simulate the ES regime of σ_x and σ_H. The result found in Ref. [17] were according to theory. Shumilin and Stepina found the ES regime Hall conductivity to be on the form of Eq. 5.4. The KMC results of this thesis featured large amounts of fluctuations. Inconsistent values of γ and α were measured such that despite the large fluctuations it was possible to see that the simulated σ_H does not follow Eq. 5.4. This is unexpected. And the function form, if there is one, of the simulated ES regime σ_H is not known.

5.8 Final comments on results and algorithms

The algorithms made in this thesis have largely been succesful at simulating Hall conductivity. Algorithm 2 is the one that given the best results, which was expected as it has exact incorporations of magnetic field equations. When comparing with experiments or other results, this is the algorithm that makes sense to use. The approximative trick done to create algorithm 1b did have a large impact on the simualted results. It changes the a dependency of the Hall conductivity, and the α values were completely different from that of algorithm 2.

The largest success of this thesis has been algorithm 2's result for Mott regime Hall conductivity. It behaves very well according to theoretical, experimental and previous simulation results. It produces consistent results for γ ($\sigma_H \propto a^\gamma$) and α when tested in multiple ways. There are differences in γ values between this thesis and the results of Ref. [17], but there is no established value of γ that should be correct. The only discrepancy seen in Mott regime σ_H is very likely caused by lattice effects. Simulations of Hall conductivity using positional disorder would take too long for it to be completed within this thesis. As result of this, no definite α value is presented. The results did find α to be in the range 0.30 to 0.50, in excellent agreement with experimental, theoretical and percolation results.

The biggest problem in this thesis has been the ES regime Hall conductivity. It features large fluctuations, and it's function form does not follow Eq. 5.4. This was concluded from inconsistent γ measurements and inconsistent α measurements. There are experimental results,

theoretical predctions and percolation simulations that all find σ_H to follow Eq. 5.4 in the ES regime. Therefore it is unlikely that the unexpected results of the KMC simulations is new physics. Most likely there is physics either missing or incorrectly coded into the simulations. As the only discrepancy found is in ES regime σ_H, it is likely the way Coulomb interaction is calculated in the magnetic field dependence of jumps where something is missing or wrong. Careful double and tripe checks finds no logical mistakes in the math or the code. Perhaps there is some interaction that has not been considered or thought of. When doing simulations there is also always the possibility of something being wrong in the code. While nothing can be found, the prospect cannot be ruled out.

A final test that could be done for ES regime σ_H should be to run simulations for longer time and for larger samples. These results would very likely have smaller fluctuations. But the issue is that algorithm 2 scales as $\mathcal{O}(N^3)$, with N being number of sites in the sample. These simulations would take far too long for them to be completed within the scope of this thesis.

CHAPTER 6

Conclusion

The aim of this thesis was to develop an algorithm able to simulate the time evolution of the Hall current in variable range hopping conduction. This was found possible using a rejection type kinetic Monte Carlo algorithm. Unfortunately, exact incorporation of magnetic fields was not found to be possible with the much faster dynamic algorithm of Tsigankov et al. [18]. Using some rough approximations it was possible to modify the dynamic algorithm to make an algorithm able to reproduce some qualities of the VRH Hall effect.

Both the rejection algorithm and the modified dynamic algorithm produce systematic Hall current when in the presence of an external magnetic field. In the Mott regime using the exact algorithm, the simulated Hall conductivity follows same general function form as theoretically predicted and experimentally tested results. The approximative algorithm's Mott regime Hall conductivity behaved mostly similarly to expectations, but with some deviations. In the ES regime, the simulated Hall conductivity features large errors, making it difficult to draw precise conclusions. Inconsistent results were found in the ES regime by testing the Hall conductivity with different methods. These inconsistent results are interpreted as the simulated ES regime Hall conductivity *not* following the same function form predicted by theoretical works and found by experiments. This holds for both algorithms.

The main simulations were done using the standard lattice model. It was chosen for it's efficiency. It was seen that using the lattice model affects the results through the dependence on localiation length. Values that should be constant had systematic dependencies on localization length. A type of dynamic algorithm was written to include positional disorder. In this case the constants had no dependence on localization length. No simulations were performed for the Hall conductivity with positional disorder. An algorithm using exact incorporation of magnetic fields with positional disorder would be too inefficient for simulations to be done within the scope of this thesis.

The main result of this thesis is that the exact KMC algorithm found the Mott regime Hall conductivity to be on the same function form as predicted by theoretical works, and as tested by experimental results and percolation simulations. The same did not work for the ES regime. When doing simulations one should always be vary of unexpected results. Is it caused by coding errors? Is there something missing or wrong in the physics coded into the simulations? Or is it new physics? The latter is unlikely to be the case. Probably there is something happening with the Coulomb interaction inside triangles, that has not been properly adressed in the smulation code.

The future work possible is very clear. Write a rejection algorithm with exact incorporation of magnetic fields and with positional disorder. The Mott regime case should be tested first. Simulations could be sped up by making a paralellized version, using the scheme developed by the authors of Ref. [30]. Use this algorithm to simulate the Hall conductivity for a range of temperatures and localization lengths. A plot of simulated $\ln(\sigma_H T/Ha^\gamma)$ vs $(T_{\text{Mott}}/T)^{1/3}$ should show a convergence to a universal curve. The value of γ will need to be determined, likely it is $\gamma = 1$ or $\gamma = 2$. Then measure the slope of the universal curve and use it to calculate the Hall effect parameter α. The value will likely lie in the range 0.30 to 0.50.

A different aspect of the VRH Hall effect could also be studied using KMC simulations. If rigid walls were used on the y-boundaries instead of periodic conditions then it should be possible to see an accumulation of charges on simulation boundaries. Measurements of charge density as function of y-position could be used to calculate the transverse electric field usually associated with the Hall effect.

The anomalous VRH Hall effect (AHE) is also something that has become of interest in recent years. Theoretical predictions by Xiong-Jun Liu et al. in Ref. [54] predict the anomalous Hall conductivity, σ_H^{AH} to be $\sigma_H^{AH} \propto \sigma_x^{1+\alpha}$ where $1.33 \leq \alpha \leq 1.76$. The sign of the AHE has also been measured to change sign with temperature [13, 55]. Ref. [56] find the sign of the AHE to change depending on the temperature at which the lattice is grown. Ref. [44] predicts the AHE sign to depend on the derivative of the DOS at the Fermi energy.

It might be interesting to study the sign of the AHE numerically, using KMC simulations similar to this project. The first difficulty in such a project would be the implementation of ferromagnetic behavior into the lattice model. The Ising model could likely be used for this. The Ising spin interaction would then act to change site potentials, affecting what jumps are likely/unlikely to happen. The AHE is expected [54] to act similarly in both the Mott and ES regime, so the Mott regime without Coulomb interaction but with Ising spin interaction should be the first situation to study. The studies should focus on temperatures at which the Ising sample is ferromagnetic, but it would also be interesting to study what happens to the conductivities around the ferromagnetic to paramagnetic transition happening at the critical temperature [57].

Such studies should study if different samples produce AHE with different sign, and if the change in sign was associated with changes to the DOS derivative. This could then be compared with the predictions of [44].

Bibliography

[1] N. F. Mott, "On the transition to metallic conduction in semiconductors," *Can. J. Phys.*, vol. 34, no. 12A, pp. 1356–1368, Dec. 1956.

[2] E. M. Conwell, "Impurity Band Conduction in Germanium and Silicon," *Phys. Rev.*, vol. 103, no. 1, pp. 51–61, Jul. 1956.

[3] O. Entin-Wohlman, Y. Gefen, and Y. Shapira, "Variable-range hopping conductivity in granular materials," *J. Phys. C: Solid State Phys.*, vol. 16, no. 7, pp. 1161–1167, Mar. 1983.

[4] A. I. Yakimov, A. V. Dvurechenskii, V. V. Kirienko, Y. I. Yakovlev, A. I. Nikiforov, and C. J. Adkins, "Long-range Coulomb interaction in arrays of self-assembled quantum dots," *Physical Review B*, vol. 61, no. 16, pp. 10 868–10 876, Apr. 2000.

[5] T. Holstein, "Hall Effect in Impurity Conduction," *Phys. Rev.*, vol. 124, no. 5, pp. 1329–1347, Dec. 1961.

[6] M. Gruenewald, H. Mueller, P. Thomas, and D. Wuertz, "The hopping hall mobility — A percolation approach," *Solid State Communications*, vol. 38, no. 11, pp. 1011–1014, Jun. 1981.

[7] Y. M. Gal'perin, E. P. German, and V. G. Karpov, "Hall effect under hopping conduction conditions," *Sov. Phys. JETP*, vol. 72, no. 1, pp. 193–200, 1991.

[8] H. Böttger and V. V. Bryksin, "A Theory of the Hall Effect in the Hopping Region in Disordered Systems. II. Random Resistor Network and Hall Effect," *physica status solidi (b)*, vol. 81, no. 1, pp. 97–106, 1977.

[9] R. Németh and B. Mühlschlegel, "Hopping Hall conductivity in disordered and granular systems," *Solid State Communications*, vol. 66, no. 9, pp. 999–1001, Jun. 1988.

[10] D. W. Koon and T. G. Castner, "Variable-range hopping and the hall coefficient in Si:As," *Solid State Communications*, vol. 64, no. 1, pp. 11–14, Oct. 1987.

[11] A. Roy, M. Levy, X. M. Guo, M. P. Sarachik, R. Ledesma, and L. L. Isaacs, "Hall coefficient of insulating n-type CdSe," *Phys. Rev. B*, vol. 39, no. 14, pp. 10 185–10 191, May 1989.

[12] Y. Zhang, P. Dai, I. Kam, and M. P. Sarachik, "Empirical relation between longitudinal and transverse transport in insulating n-CdSe," *Phys. Rev. B*, vol. 49, no. 7, pp. 5032–5033, Feb. 1994.

[13] R. M. Qiao, S. S. Yan, T. S. Xu, M. W. Zhao, Y. X. Chen, G. L. Liu, W. L. Yang, R. K. Zheng, and L. M. Mei, "Anomalous Hall Effect in Variable Range Hopping Regime: Unusual Scaling Law and Sign Reversal with Temperature," *arXiv:1406.5672 [cond-mat]*, Jun. 2014.

[14] Y. Kajikawa, "Hall factor for hopping conduction in n- and p-type GaN," *physica status solidi c*, vol. 14, no. 1-2, p. 1600129, 2017.

[15] P. N. Butcher and J. A. Mcinnes, "The Hall mobility of carriers hopping in an impurity band," *Philosophical Magazine B*, vol. 44, no. 5, pp. 595–601, Nov. 1981.

[16] P. N. Butcher, J. A. Mcinnes, and S. Summerfield, "The Hall mobility of carriers hopping in an impurity band," *Philosophical Magazine B*, vol. 48, no. 6, pp. 551–560, Dec. 1983.

[17] A. V. Shumilin and N. P. Stepina, "Hall effect in two-dimensional systems with hopping transport and strong disorder," *Phys. Rev. B*, vol. 98, no. 11, p. 115303, Sep. 2018.

[18] D. N. Tsigankov, E. Pazy, B. D. Laikhtman, and A. L. Efros, "Long time relaxation of interacting electrons in the regime of hopping conduction," *Physical Review B*, vol. 68, no. 18, Nov. 2003.

[19] M. Caravaca, A. Voje, J. Bergli, M. Ortuño, and A. M. Somoza, "Non-linear conductivity in Coulomb glasses," *Annalen der Physik*, vol. 18, no. 12, pp. 873–876, Dec. 2009.

[20] J. Bergli, A. M. Somoza, and M. Ortuño, "Effects of many-electron jumps in the relaxation and conductivity of Coulomb glasses," *Phys. Rev. B*, vol. 84, no. 17, p. 174201, Nov. 2011.

[21] M. Kirkengen and J. Bergli, "Slow relaxation and equilibrium dynamics in a two-dimensional Coulomb glass: Demonstration of stretched exponential energy correlations," *Phys. Rev. B*, vol. 79, no. 7, p. 075205, Feb. 2009.

[22] C. Hepburn, "Basic Semiconductor Physics, Britney Spears' Guide To Semiconductor Physics," http://britneyspears.ac/physics/basics/basics.htm.

[23] M. A. Green, "Intrinsic concentration, effective densities of states, and effective mass in silicon," *Journal of Applied Physics*, vol. 67, no. 6, pp. 2944–2954, Mar. 1990.

[24] C. Kittel, *Introduction to Solid State Physics*, 8th ed. Hoboken, NJ: Wiley, Nov. 2004.

[25] B. I. Shklovskii and A. L. Efros, *Electronic Properties of Doped Semiconductors*, ser. Springer Series in Solid-State Sciences. Berlin Heidelberg: Springer-Verlag, 1984.

[26] N. P. Stepina, A. V. Nenashev, and A. V. Dvurechenskii, "Hall effect in hopping conduction in an ensemble of quantum dots," *JETP Letters*, vol. 106, no. 5, pp. 308–312, Sep. 2017.

[27] A. Voje, "Non-Ohmic Variable Range Hopping in Lightly Doped Semiconductors," Master's thesis, University of Oslo, Jun. 2009.

[28] N. F. Mott, "Conduction in Non-Crystalline Materials," *Philosophical Magazine*, vol. 19, no. 160, pp. 835–852, 1969.

[29] A. Miller and E. Abrahams, "Impurity Conduction at Low Concentrations," *Phys. Rev.*, vol. 120, no. 3, pp. 745–755, Nov. 1960.

[30] E. E. Ferrero, A. B. Kolton, and M. Palassini, "Parallel kinetic Monte Carlo simulation of Coulomb glasses," *AIP Conference Proceedings*, vol. 1610, no. 1, pp. 71–76, Aug. 2014.

[31] A. L. Efros and B. I. Shklovskii, "Coulomb gap and low temperature conductivity of disordered systems," *J. Phys. C: Solid State Phys.*, vol. 8, no. 4, pp. L49–L51, Feb. 1975.

[32] D. N. Tsigankov and A. L. Efros, "Variable Range Hopping in Two-Dimensional Systems of Interacting Electrons," *Phys. Rev. Lett.*, vol. 88, no. 17, p. 176602, Apr. 2002.

[33] R. M. Hill, "On the observation of variable range hopping," *physica status solidi (a)*, vol. 35, no. 1, pp. K29–K34, 1976.

[34] A. G. Zabrodskii, "Hopping conduction and density of localized states near the Fermi level," *Soviet Physics Semiconductors-USSR*, vol. 11, no. 3, pp. 345–347, 1977.

[35] E. H. Hall, "On a New Action of the Magnet on Electric Currents," *American Journal of Mathematics*, vol. 2, no. 3, pp. 287–292, 1879.

[36] T. Holstein, "Sign of the hall coefficient in hopping-type charge-transport," *Philosophical Magazine*, vol. 27, no. 1, pp. 225–233, Jan. 1973.

[37] H. Frietzsche, "Electronic Properties of Amorphous Semiconductors," in *Amorphous and Liquid Semiconductors*, J. Tauc, Ed. Springer US, 1974.

[38] P. G. L. Comber, D. I. Jones, and W. E. Spear, "Hall effect and impurity conduction in substitutionally doped amorphous silicon," *The Philosophical Magazine: A Journal of Theoretical Experimental and Applied Physics*, vol. 35, no. 5, pp. 1173–1187, May 1977.

[39] D. Emin, "The sign of the Hall effect in hopping conduction," *The Philosophical Magazine: A Journal of Theoretical Experimental and Applied Physics*, vol. 35, no. 5, pp. 1189–1198, May 1977.

[40] B. Movaghar, B. Pohlmann, and D. Wurtz, "The Hall mobility in hopping conduction," *J. Phys. C: Solid State Phys.*, vol. 14, no. 33, pp. 5127–5137, Nov. 1981.

[41] H. Böttger and V. V. Bryksin, "A Theory of the Hall Effect in the Hopping Region in Disordered Systems. III. DC Hall Effect," *physica status solidi (b)*, vol. 81, no. 2, pp. 433–441, 1977.

[42] L. Friedman, "Hall effect in the dielectric regime of granular metal films," *Phys. Rev. B*, vol. 25, no. 6, pp. 3512–3518, Mar. 1982.

[43] L. Friedman and M. Pollak, "The Hall effect in the variable-range-hopping regime," *Philosophical Magazine B*, vol. 44, no. 4, pp. 487–507, Oct. 1981.

[44] A. A. Burkov and L. Balents, "Anomalous Hall Effect in Ferromagnetic Semiconductors in the Hopping Transport Regime," *Physical Review Letters*, vol. 91, no. 5, Jul. 2003.

[45] L.-F. Arsenault, B. Movaghar, P. Desjardins, and A. Yelon, "Magnetotransport in the insulating regime of Mn-doped GaAs," *Phys. Rev. B*, vol. 78, no. 7, p. 075202, Aug. 2008.

[46] L. Friedman and M. Pollak, "Hall mobility due to hopping-type conduction in disordered systems," *Philosophical Magazine B*, vol. 38, no. 2, pp. 173–189, Aug. 1978.

[47] M. Rohde and H. Micklitz, "Indication of universal behavior of Hall conductivity near the metal-insulator transition in disordered systems," *Physical Review B*, vol. 36, no. 14, pp. 7572–7575, Nov. 1987.

[48] L. Essaleh, S. M. Wasim, and J. Galibert, "Hall coefficient and Hall mobility in the variable range hopping conduction regime in n-type CuInSe2," *Materials Letters*, vol. 60, no. 16, pp. 1947–1949, Jul. 2006.

[49] M. Amitay and M. Pollak, *J. Phys. Soc. Jpn.*, vol. 21, no. 3, pp. 549–549, Mar. 1966.

[50] R. S. Klein, "Investigation of the Hall effect in impurity-hopping conduction," *Phys. Rev. B*, vol. 31, no. 4, pp. 2014–2021, Feb. 1985.

[51] E. I. Levin, V. L. Nguen, B. I. Shklovskii, and A. L. Efros, "Coulomb gap and hopping electric conduction. Computer simulation," *Sov. Phys. JETP*, vol. 64, no. 4, pp. 842–848, 1987.

[52] "Kinetic Monte Carlo," *Wikipedia*, May 2019, page Version ID: 896123246.

[53] G. L. Squires and S. G. L, *Practical Physics*. Cambridge University Press, Aug. 2001.

[54] X.-J. Liu, X. Liu, and J. Sinova, "Scaling of the anomalous Hall effect in the insulating regime," *Physical Review B*, vol. 84, no. 16, Oct. 2011.

[55] L. N. Oveshnikov, V. A. Kulbachinskii, A. B. Davydov, B. A. Aronzon, I. V. Rozhansky, N. S. Averkiev, K. I. Kugel, and V. Tripathi, "Berry phase mechanism of the anomalous Hall effect in a disordered two-dimensional magnetic semiconductor structure," *Scientific Reports*, vol. 5, no. 1, Dec. 2015.

[56] W. Allen, E. G. Gwinn, T. C. Kreutz, and A. C. Gossard, "Anomalous Hall effect in ferromagnetic semiconductors with hopping transport," *Phys. Rev. B*, vol. 70, no. 12, p. 125320, Sep. 2004.

[57] L. Onsager, "Crystal Statistics. I. A Two-Dimensional Model with an Order-Disorder Transition," *Phys. Rev.*, vol. 65, no. 3-4, pp. 117–149, Feb. 1944.

Appendices

APPENDIX A

Algorithm 1a with positional disorder algorithm 1ar

Algorithm 1a is also extended to simulate VRH dynamics on samples with randomly positioned sites. We call this algorithm 1ar. There are many similarities between algorithms 1a and 1ar. This section only covers the differences.

A.1 Initialization process

Algorithm 1a uses the lattice structure to reuse properties such as neighbors, distances and rates for all the sites. This is not possible for the random sample, and the properties for each site has to be stored individually. This makes the initalization process more complicated. The algorithm uses a cutoff jump distance, labeled maxJL.

```
1  // N is the number of sites in the sample
2  for (i=0; i<N; i++){ // Assign random positions to sites
3    randomNumber = RNG(0,1) // random number between 0 and 1
4    sitePositions[i][0] = L * randomNumber; // x position of site i
5    randomNumber = RNG(0,1) // random number between 0 and 1
6    sitePositions[i][1] = L * randomNumber; // y position of site i
7  }
8
9  for (i=0; i<N; i++){
10   for (j=0; j<N; j++){  // Calculate distanceMatrix and calculate number of
       neighbors for each site
11     dx = sitePositions[j][0] - sitePositions[i][0];
12     dy = sitePositions[j][1] - sitePositions[i][1];
13
14     // Periodic boundary conditions
15     if      (dx > L/2) dx -= L;
16     else if (dx < -L/2) dx += L;
17
18     if      (dy > L/2) dy -= L;
19     else if (dy < -L/2) dy += L;
20
21     distanceMatrix[i][j] = sqrt(dx*dx + dy*dy);
22     if (distanceMatrix[i][j] < maxJL) nNeighbors[i]++;
23   }
24   GammaT[i]      = new double[nNeighbors[i]];
25   final2Site[i] = new int    [nNeighbors[i]];
26   dxNeighbor[i] = new double[nNeighbors[i]];
```

```
27    dyNeighbor[i] = new double[nNeighbors[i]];
28
29  }
30
31  // Calculate all transition rates
32  for (i=0; i<N; i++){  // Initial site
33    gamma  = 0.0;
34    n  = 0;
35    for (j=0; j<N; j++){ Final site
36      overlap_ij = distanceMatrix[i][j];
37      if (overlap_ij < maxJL){  // If final site is a neighbor of initial site
38        if (i != j){
39          // n represents what neighbor site j is to site i.
40
41          finalSite[i][n] = j;
42
43          dxNeighbor[i][n] = sitePositions[j][0] - sitePositions[i][0];
44          dxNeighbor[i][n] = sitePositions[j][1] - sitePositions[i][1];
45
46          if      (dxNeighbor[i][n] >  L/2) dxNeighbor[i][n] -= L;
47          else if (dxNeighbor[i][n] < -L/2) dxNeighbor[i][n] += L;
48
49          if      (dyNeighbor[i][n] >  L/2) dyNeighbor[i][n] -= L;
50          else if (dyNeighbor[i][n] < -L/2) dyNeighbor[i][n] += L;
51
52          gamma += exp(-A*overlap_ij);
53          GammaT[i][n] = gamma;
54
55          n++;
56        }
57        else { // Rate of going to itself is zero
58          GammaT[i][n] = gamma;
59          n++;
60        }
61      }
62    }
63    totalGammatoSitei[i] = gamma;
64    totalTotalGamma += gamma;
65    cumulativeTotalTotalGamma[i] = totalTotalGamma;
66  }
```

A.2 Time of one Monte Carlo cycle

The derivation of the time of one Monte Carlo cycle $\langle \Delta t_{\mathrm{MC}} \rangle$ is the same as for the lattice model up to Eq. 4.3. In the lattice model $\sum_{j \neq i} \Gamma_{ij}^T$ is independent of site i, because the lattice is homogeneous. This is not the case in the random sample. Instead, the double sum in $\sum_{j \neq i} \Gamma_{ij}^T$ is simply computed. The Monte Carlo time step becomes

$$\langle \Delta t_{\mathrm{MC}} \rangle = \left(\nu \sum_i \sum_{j \neq i} \Gamma_{ij}^T \right)^{-1}, \tag{A.1}$$

where ν is the ratio of sites with electrons able to move. The sum $\sum_i \sum_{j \neq i} \Gamma_{ij}^T$ is equivalent to "totalTotalGamma" in the code snippet in the initialization process.

A.3 Performing MC jumps

Algorithm 1ar performes jumps on a random lattice in a very similar manner to how algorithm 1a does it on the lattice model. The only difference is in finding the choice of initial and final site.

The algorithm first has to find an initial site where a jump can start. The lattice model picks this uniformly as all the sites have equal transition rates. The random sample algorithm instead uses the binary search method on the sum of transition rates for each site. If the site found is empty then the binary search method is applied again until an occupied site is found.

The sum of transition rates from site i is $\sum_{j\neq i}\Gamma_{ij}^{T}$, and the sum of all the transition rates is $\sum_i\sum_{j\neq i}\Gamma_{ij}^{T}$. A uniformly distributed random number $r \in (0,1)$ is generated. This random number is then compared with the sum of transition rates to find the appropriate initial site. For example, if $r\sum_i\sum_{j\neq i}\Gamma_{ij}^{T}$ lies between the sum of transition rates for sites $i=2$ and $i=3$, as $\sum_{j\neq 2}\Gamma_{2j}^{T} < r\sum_i\sum_{j\neq i}\Gamma_{ij}^{T} < \sum_{j\neq 3}\Gamma_{3j}^{T}$, then site number 3 is tested to be the initial site. If it is occupied then it will be chosen, if it is empty the binary search method is applied again.

The next step is to find a final site j the jump from i can hop to. This is done in the same manner as algorithm 1a. The only difference is that the transition rate from site i, and the number of neighbors close to i, has to be used. Else everything is the same.

Now that the transition $i \to j$ has been found, it has to be tested. This is done in the same exact way as algorithm 1a.

APPENDIX B

Additional results

In this appendix we present some additional results that were not in the main text.

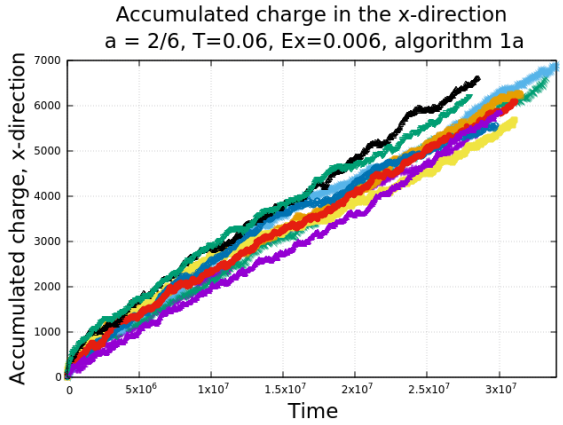

Figure B.1: Accumulated charge in the x-direction over 10 samples using localization length $a = 2/6$, $T = 0.06$ and $Ex = 0.006$. The graph shows linear tendency, but the small localization length causes large differences between samples. This leads to larger error in results when the localization lenght is small.

Table B.2: Calculated α_{Mott} for $a = 2/2$ using different methods with variable magnetic field. The presented values are calcualted from the temperature constants in table B.3.

H	μ_H and σ_x	σ_H and σ_x	$\sigma_H T \propto (\sigma_x T)^{1+\alpha}$
0.1	0.39 ± 0.02	0.39 ± 0.04	0.39 ± 0.02
0.2	0.34 ± 0.01	0.34 ± 0.03	0.34 ± 0.01
0.3	0.33 ± 0.02	0.34 ± 0.03	0.34 ± 0.02
0.4	0.35 ± 0.02	0.35 ± 0.03	0.36 ± 0.01
0.5	0.31 ± 0.01	0.32 ± 0.02	0.31 ± 0.01

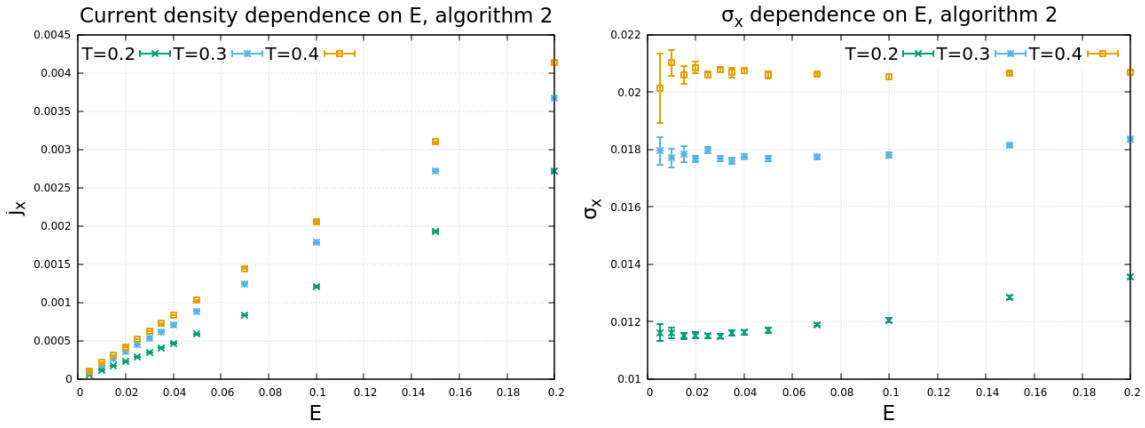

(a) (b)

Figure B.2: The dependence of j_x (a) and σ_x (b) on electric field E simulated by algorithm 2. These results are found to be in exact accordance with the results of algorithm 1a for the simulated points, found in Fig. 5.2. This supports the claim that algorithm 1a and algorithm 2 produce exactly the same results.

Table B.1: Temperature constants measured from simulations using various algorithms. $H = 0.2$ was used for algorithm 2 and $H = 0.4$ was used for algorithm 1b. Subscript H means the value was measured from simulated σ_H. Subscript μ_H means the value was measured from simulated μ_H. M - Mott regime, ES - ES regime.

a	Algorithm 1b					
	$T_{\mathrm{M}}^{1/3}$	$T_{\mathrm{M,H}}^{1/3}$	$\alpha_{\mathrm{Mott}} T_{\mathrm{M},\mu_H}^{1/3}$	$T_{\mathrm{ES}}^{1/2}$	$T_{\mathrm{ES,H}}^{1/2}$	$\alpha_{\mathrm{ES}} T_{\mathrm{ES},\mu_H}^{1/2}$
2/2	3.03 ± 0.03	3.46 ± 0.03	0.25 ± 0.01	2.44 ± 0.02	2.96 ± 0.05	0.70 ± 0.02
2/3	3.66 ± 0.03	4.18 ± 0.07	0.50 ± 0.06	2.68 ± 0.03	3.33 ± 0.07	1.11 ± 0.07
2/4	4.35 ± 0.04	5.08 ± 0.09	0.9 ± 0.1	2.96 ± 0.04	3.33 ± 0.05	0.6 ± 0.3
2/5	5.02 ± 0.07	5.3 ± 0.2	0.7 ± 0.3	3.13 ± 0.07	2.7 ± 0.2	0.2 ± 0.2
2/6	5.7 ± 0.1	4.9 ± 0.3	-0.6 ± 0.5	-	-	-
a	Algorithm 2					
	$T_{\mathrm{M}}^{1/3}$	$T_{\mathrm{M,H}}^{1/3}$	$\alpha_{\mathrm{Mott}} T_{\mathrm{M},\mu_H}^{1/3}$	$T_{\mathrm{ES}}^{1/2}$	$T_{\mathrm{ES,H}}^{1/2}$	$\alpha_{\mathrm{ES}} T_{\mathrm{ES},\mu_H}^{1/2}$
2/2	3.49 ± 0.02	4.63 ± 0.06	1.16 ± 0.06	2.31 ± 0.01	4.0 ± 0.2	1.8 ± 0.2
2/3	4.28 ± 0.03	5.9 ± 0.3	1.8 ± 0.3	2.50 ± 0.03	3.4 ± 0.2	1.3 ± 0.2
2/4	4.80 ± 0.07	6.7 ± 0.4	2.1 ± 0.4	2.55 ± 0.01	5 ± 1	2 ± 1

Table B.3: Dependence of temperature constants on applied magnetic field using $a = 2/2$. The values are used to calculate the α_{Mott} values in table B.2.

H	$T_{\mathrm{M}}^{1/3}$	$T_{\mathrm{M,H}}^{1/3}$	$\alpha T_{\mathrm{M},\mu_H}^{1/3}$
0.1	3.53 ± 0.03	4.91 ± 0.04	1.38 ± 0.06
0.2	3.44 ± 0.02	4.63 ± 0.06	1.17 ± 0.05
0.3	3.37 ± 0.02	4.50 ± 0.06	1.12 ± 0.06
0.4	3.28 ± 0.02	4.42 ± 0.06	1.14 ± 0.05
0.5	3.19 ± 0.01	4.21 ± 0.04	0.98 ± 0.03

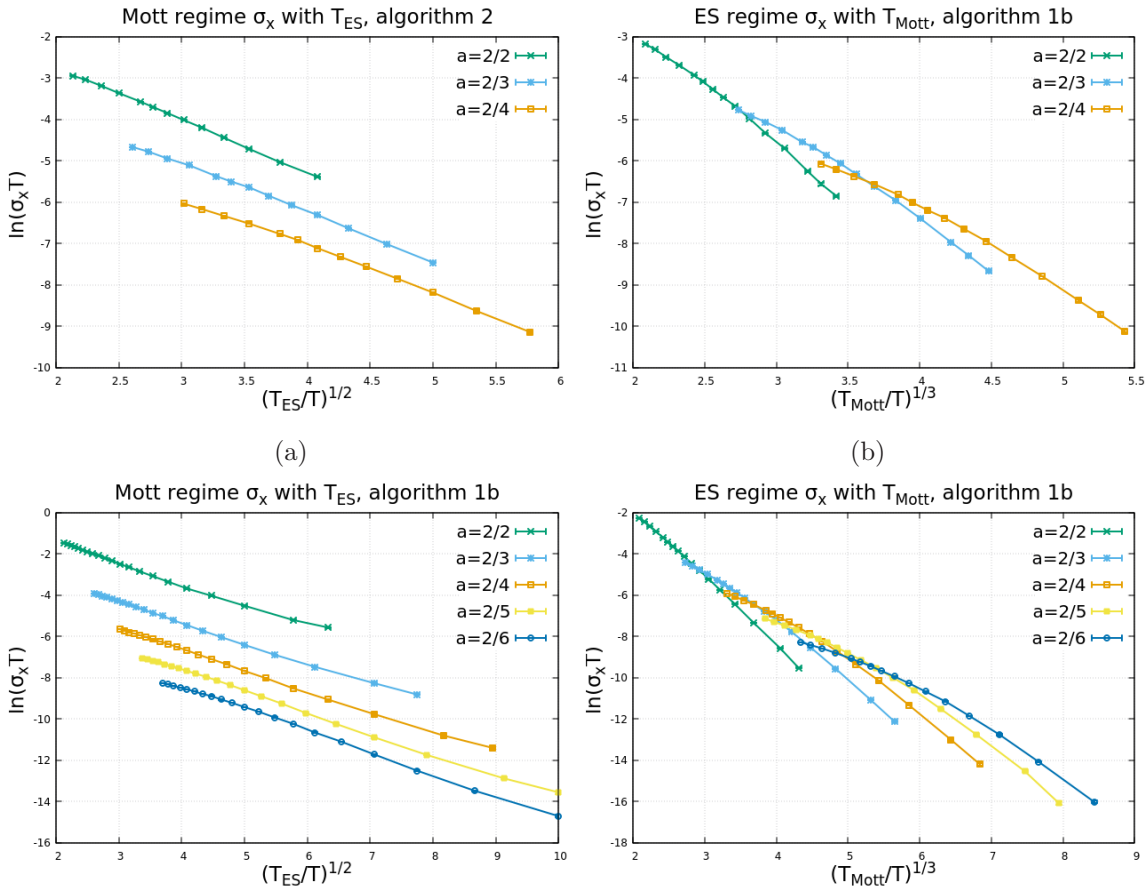

Figure B.3: Plotting regime σ_x as the wrong regime VHR law. Mott regime σ_x as ES's law is plotted in (a) and (c), ES regime σ_x as Mott's law is plotted in (b) and (d). Top row shows algorithm 2 results and bottom row shows algorithm 1b results. No data collapse is possible for these relations. This is used to support the claim of Mott regime conductivity following Mott's law, and ES regime conductivity following ES's law.

Table B.4: Calculated α_{Mott} for $a = 2/3$ using different methods with variable magnetic field. The presented values are calcualted from the temperature constants in table B.5.

H	μ_H and σ_x	σ_H and σ_x	$\sigma_H T \propto (\sigma_x T)^{1+\alpha}$
0.1	0.50 ± 0.14	0.44 ± 0.09	0.51 ± 0.13
0.2	0.44 ± 0.07	0.42 ± 0.08	0.45 ± 0.05
0.3	0.43 ± 0.07	0.42 ± 0.04	0.40 ± 0.03
0.4	0.49 ± 0.03	0.48 ± 0.05	0.48 ± 0.02
0.5	0.40 ± 0.04	0.40 ± 0.07	0.44 ± 0.02

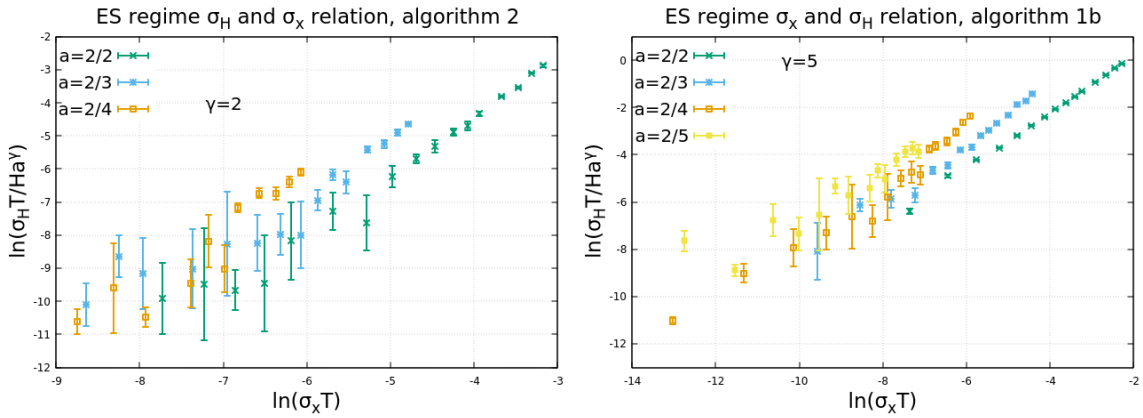

(a) (b)

Figure B.4: ES regime attempted data collapse using the relation between the longitudinal and Hall conductivity (see Eq. 5.6). The γ parameters are the ones found from R_H data collapse. As seen, the data does not collapse for these parameters. This suggests the function form used to derive Eq. 5.6 does not hold for the ES regime conductivity.

Table B.5: Dependence of temperature constants on applied magnetic field using $a = 2/3$. The values are used to calculate the α_{Mott} values in table B.4.

H	$T_{\text{M}}^{1/3}$	$T_{\text{M,H}}^{1/3}$	$\alpha T_{\text{M},\mu_H}^{1/3}$
0.1	4.23 ± 0.04	6.09 ± 0.3	2.1 ± 0.6
0.2	4.25 ± 0.03	6.04 ± 0.3	1.87 ± 0.3
0.3	4.10 ± 0.03	5.81 ± 0.3	1.75 ± 0.3
0.4	4.11 ± 0.03	6.08 ± 0.11	2.01 ± 0.14
0.5	4.08 ± 0.04	5.70 ± 0.18	1.63 ± 0.15

Table B.6: Slope $\alpha T_{\text{M},\mu_H}^{1/3}$ measured from μ_H when using σ_x at $H = 0$ and σ_H at $H = 0.2$ in algorithm 2. The values are used to calculate the α_{Mott} values in tables B.7 and B.8.

H	$a = 2/2$	$a = 2/3$
0.1	1.24 ± 0.06	2.08 ± 0.7
0.2	1.04 ± 0.05	1.72 ± 0.3
0.3	0.85 ± 0.05	1.40 ± 0.2
0.4	0.77 ± 0.04	1.91 ± 0.11
0.5	0.58 ± 0.06	1.46 ± 0.10

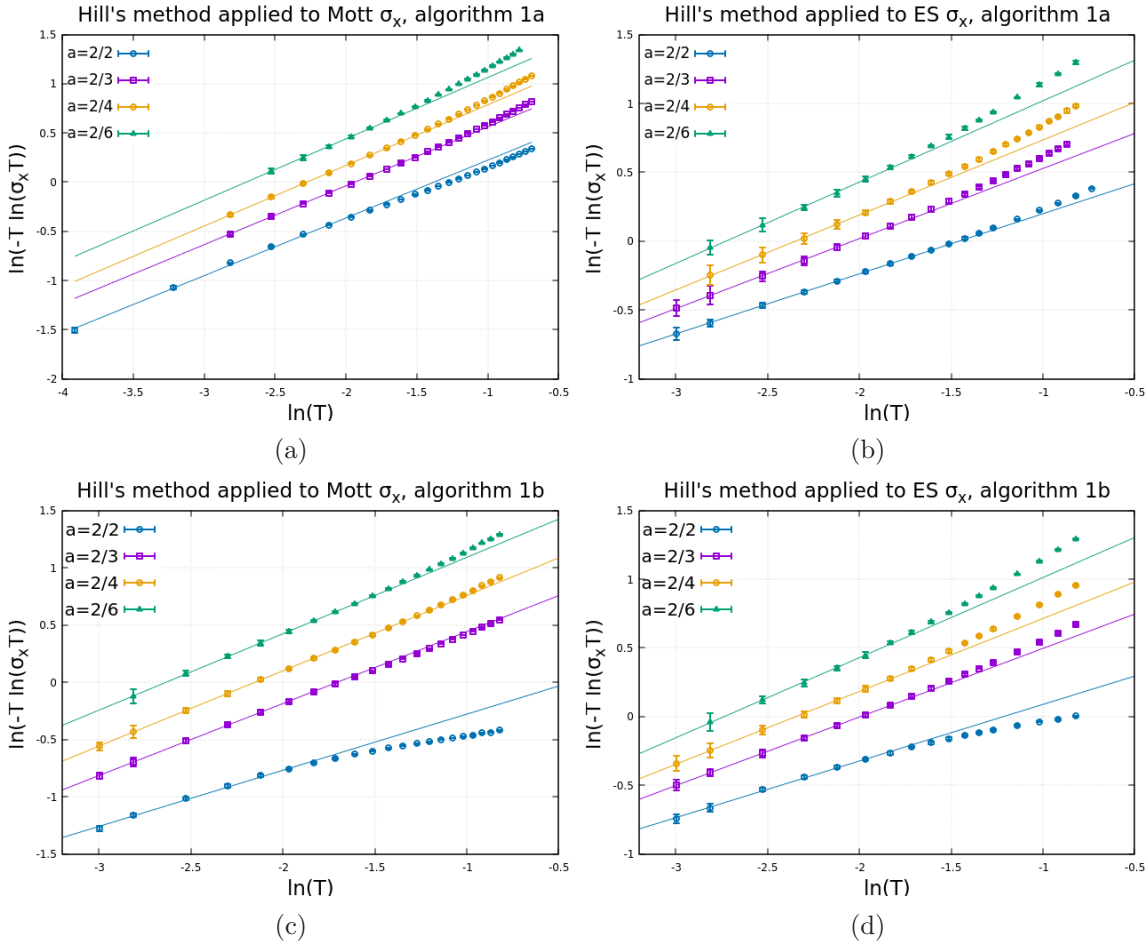

Figure B.5: Log-log plot of ϵ_3 with temperature T for algorithms 1a and 1b for Mott and ES regime. The figures show linear behavior at low temperature, the slope of which should give the exponent. Measured exponents are presented in table 5.4.

Table B.7: Calculated α_{Mott} for $a = 2/2$ using different methods with variable magnetic field. The presented values are calculated using σ_x temperature constant $T_{\text{M}}^{1/3} = 3.66 \pm 0.03$ at $H = 0$. The rest of the values are taken from tables B.3 and B.6.

H	μ_H and σ_x	σ_H and σ_x	$\sigma_H T \propto (\sigma_x T)^{1+\alpha}$
0.1	0.33 ± 0.02	0.34 ± 0.04	0.34 ± 0.02
0.2	0.28 ± 0.01	0.26 ± 0.04	0.28 ± 0.02
0.3	0.23 ± 0.01	0.23 ± 0.04	0.23 ± 0.02
0.4	0.21 ± 0.01	0.21 ± 0.04	0.21 ± 0.01
0.5	0.16 ± 0.01	0.15 ± 0.04	0.17 ± 0.02

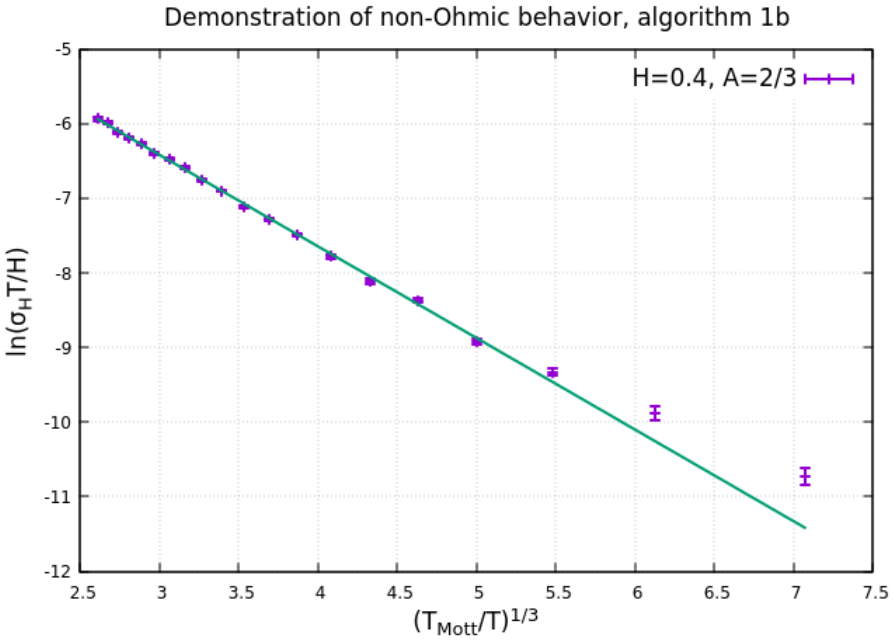

Figure B.6: Demonstration of non-Ohmic behavior for the two (maybe three) lowest simulated temperatures. All the data is generated using $Ex = 0.10$. The lowest three simulated temperatures are $0.06, 0.08$ and 0.10. Plotting like this was used to find the set of optimal electric fields possible to use to simulate Ohmic Hall conductivity with algorithm 1b.

Table B.8: Calculated α_{Mott} for $a = 2/3$ using different methods with variable magnetic field. The presented values are calculated using σ_x temperature constant $T_{\text{M}}^{1/3} = 4.29 \pm 0.03$ at $H = 0$. The rest of the values are taken from tables B.5 and B.6.

H	μ_H and σ_x	σ_H and σ_x	$\sigma_H T \propto (\sigma_x T)^{1+\alpha}$
0.1	0.48 ± 0.16	0.42 ± 0.08	0.49 ± 0.14
0.2	0.40 ± 0.08	0.41 ± 0.08	0.43 ± 0.06
0.3	0.33 ± 0.05	0.35 ± 0.08	0.36 ± 0.04
0.4	0.44 ± 0.02	0.42 ± 0.05	0.43 ± 0.02
0.5	0.34 ± 0.02	0.33 ± 0.06	0.37 ± 0.02

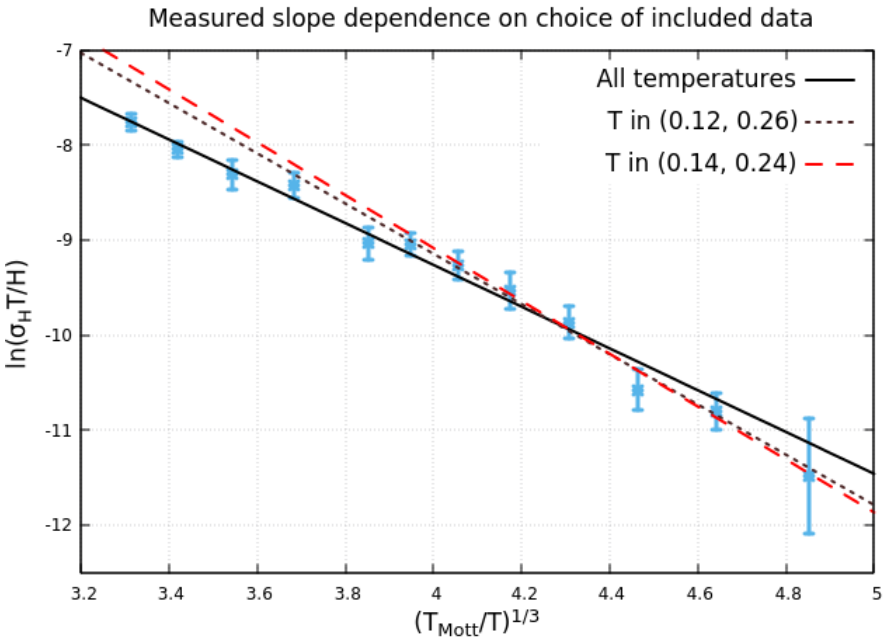

Figure B.7: Temperature dependence of R_H with $a = 2/4$ simulated using algorithm 2. The figure illustrates the difficulty in identifying what is linear behavior, what data points should and should not be included in measurement and the subsequent large error in results. The black filled line has slope= 3.49 ± 0.13, the dotted brown line has slope= $4.20 \pm 0.2$and the dashed red line has slope= 4.4 ± 0.3.

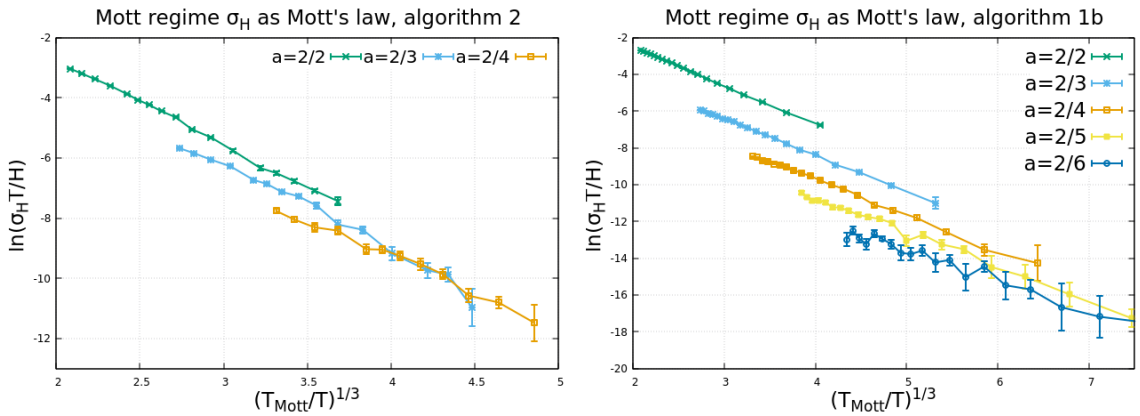

(a) (b)

Figure B.8: Simulated Mott regime Hall conductivity σ_H plotted as standard Mott's law without any $\propto a^\gamma$ dependence using algorithm 2 (a) and algorithm 1b (b). The figure shows vertical gaps between curves with different localization lengths. No data collapse is possible in this case.

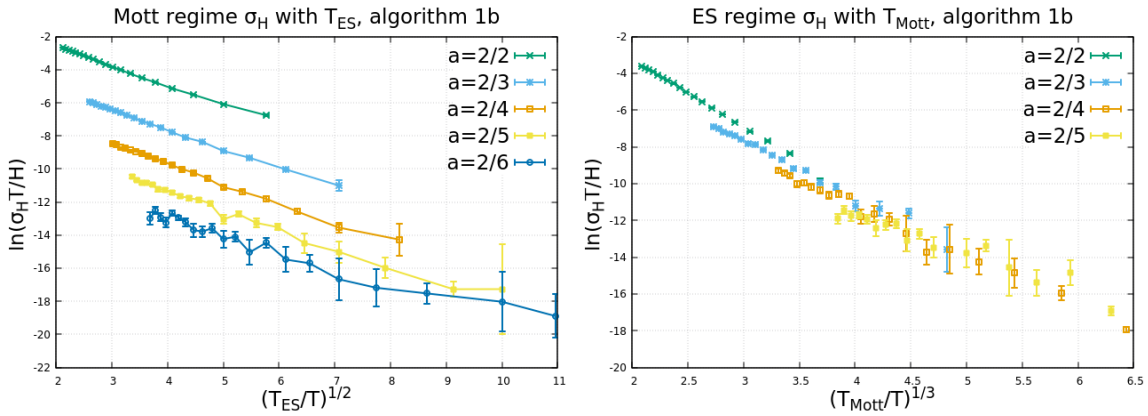

(a) (b)

Figure B.9: Regime generated σ_H plotted using switched a dependency in T_0. (a) is Mott data plotted with T_{ES} and (b) shows ES data plotted with T_{Mott}. No data collapse is possible for these relations. This shows that Mott regime σ_H does not follow ES's law, and that ES regime σ_H does not follow Mott's law.

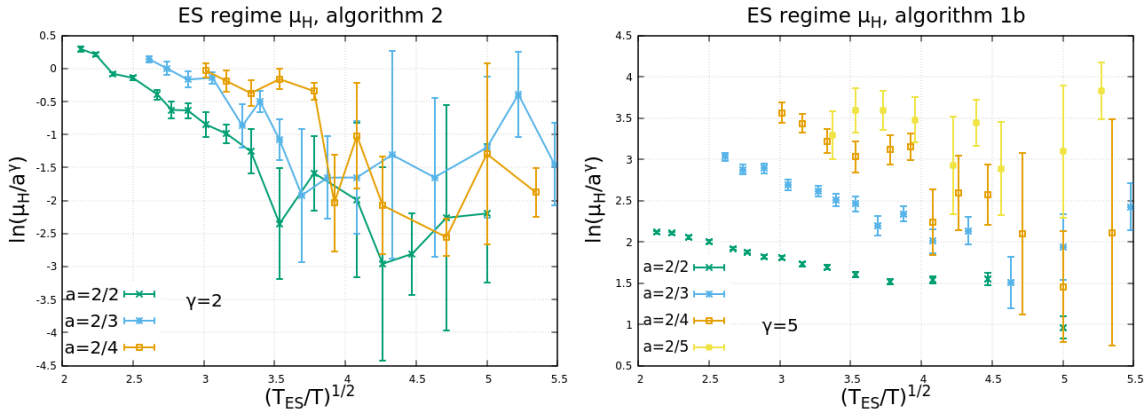

(a) (b)

Figure B.10: ES regime Hall mobility μ_H plotted using values of γ that was found to give the Hall conductvity σ_H the best data collapse. The result is no data collapse. This shows an inconsistency in values found for γ in the ES regime.

APPENDIX C

Comparison of algorithms 1a and 1b

The left column of Fig. C.1 shows the Mott's law plot for algorithms 1a and 1b for localization lengths $a \in (2/2, 2/3, 2/4, 2/6)$. The right column of Fig. C.1 shows the difference between the linear regression, and the data. The linear regression uses measurements from the five smallest simulated temperatures ($T \in [0.05 - 0.12]$). For the largest used localization length $a = 2/2$, we see that both the algorithms increase above their fitted lines before decreasing a little. Algorithm 1b starts to decrease at a higher temperature than algorithm 1a does. Looking at Fig. C.1d, algorithm 1a only has a small "bump" of one data point above the fitted line whereas algorithm 1b has many. In Fig. C.1d algorithm 1b data points deviate first below then above the linear fit line. The behavior of going first below and then above (or opposite) is an indication of systematic behavior not picked up by Mott's law. If σ_x follows Mott's law exactly then there should only be random fluctuations in the figures in the right column of Fig. C.1. The extra systematic behavior to be present for both algorihms for large a, but dissapears for $a \lessapprox 2/3$ in algorithm 1a. It is also more prominent for algorithm 1b.

The effect of introducing three-site jumps in algorithm 1b seems to change the behavior of σ_x to be less like Mott's law. Still, Mott's law is a very good approximation to the simulated σ_x.

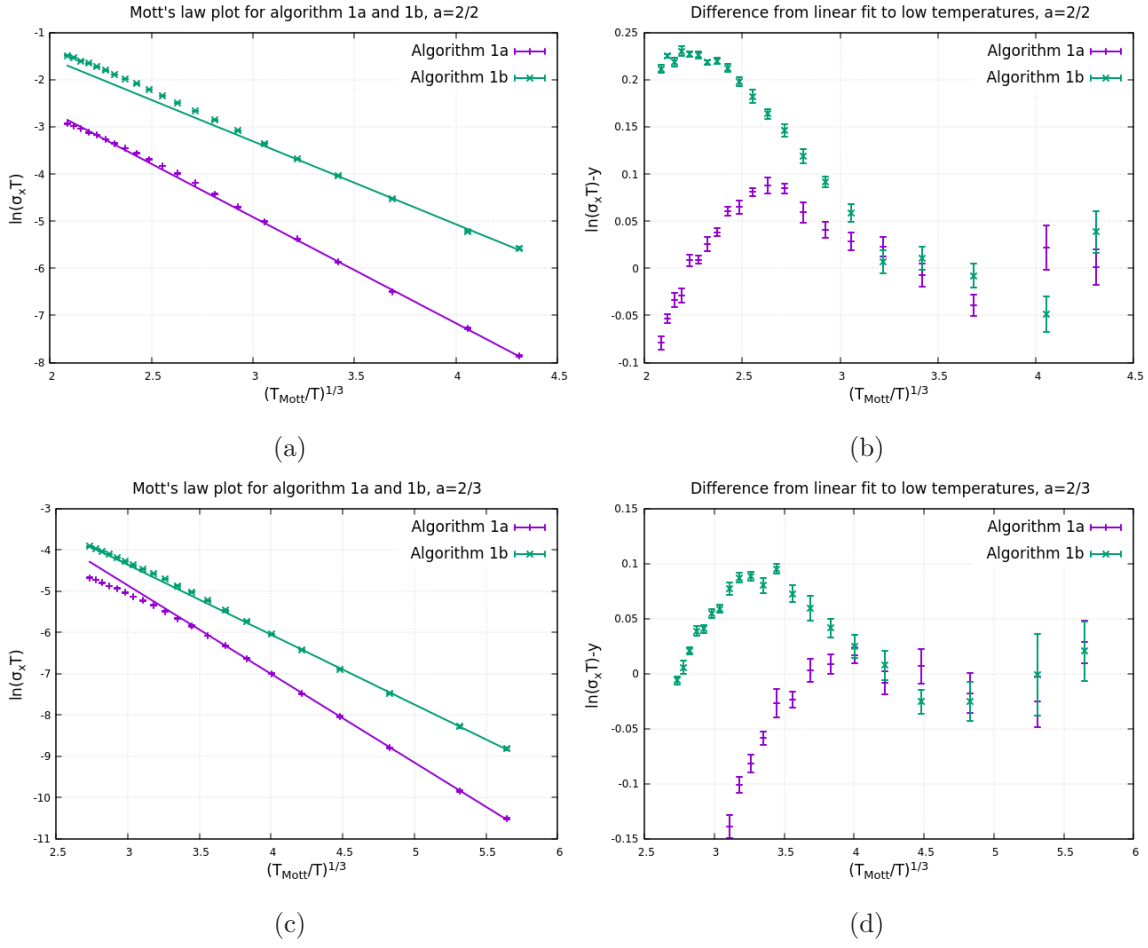

Figure C.1: Comparison between algorithms 1a and 1b when fitting simulated σ_x to Mott's law temperature dependence. Left column graphs show Mott's law plots. Right column graphs show difference between line fitted to the 5 lowest temperature data points.

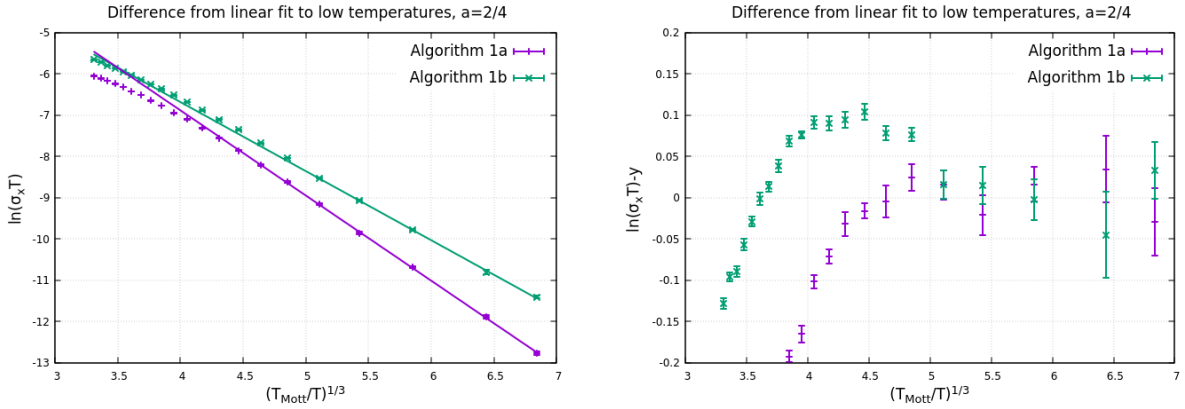

(e)

(f)

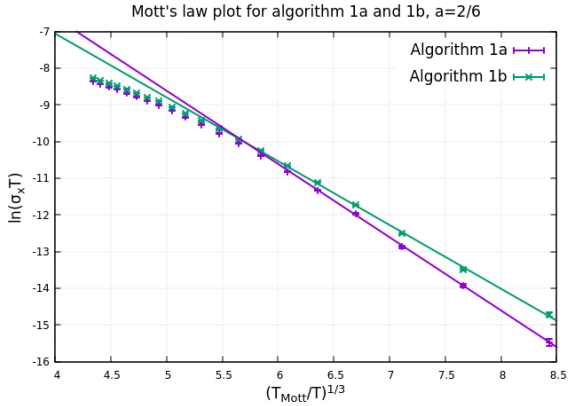

(g)

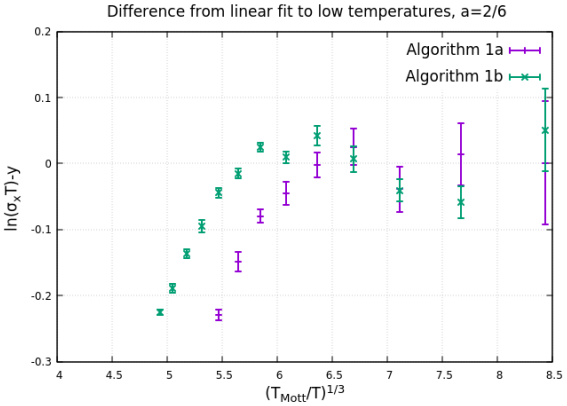

(h)

Figure C.1: Comparison between algorithms 1a and 1b when fitting simulated σ_x to Mott's law temperature dependence. Left column graphs show Mott's law plots. Right column graphs show difference between line fitted to the 5 lowest temperature data points.

APPENDIX D

Impact of not dealing with negative rates in algorithm 1b

In the initialization step of algorithm 1b we set $\Gamma_{ikj}^{(n)T} = 0$ if it instead would be negative. When this is considered σ_H shows a close to linear dependence on H, see Fig. D.1a. If it is not considered, then the dependence is still linear but with a clear discontinuity at $H \approx 0.5$. This is seen in Fig. D.1b where linear regression has been applied to data for only large or small H. These fitted lines intersect between $H = 0.48$ and $H = 0.50$. When $H = 0.5$, jumps with area $A = 2$ have either $\Gamma_{ikj}^{(0)T} = 0$ or $\Gamma_{ikj}^{(1)T} = 0$. Increasing H more, one of the rates becomes negative. Since the discontinuity happens at $H = 0.5$, the discontinuous behavior can be attributed as jumps with $A_{ikj} = 2$ disturbing the system through negative rates. It can be interpreted as jumps with $A_{ikj} = 2$ being the longest jump that is important to the simulations of σ_y. Jumps with larger areas, for example $A_{ikj} = 10$ sets $\Gamma_{ikj}^{T} = 0$ when $H > 0.2$. However for such jumps $\Gamma_{ikj}^{T} \approx 0$ even when $H < 0.2$, and impact of setting them to zero does not have meaningful impact on the simulated dynamics. This is seen as there is no measurable discontinuity or irregularity in Fig. D.1b at $H = 0.2$. Therefore $H = 0.5$ sets an upper bound for simulations using algorithm 1b.

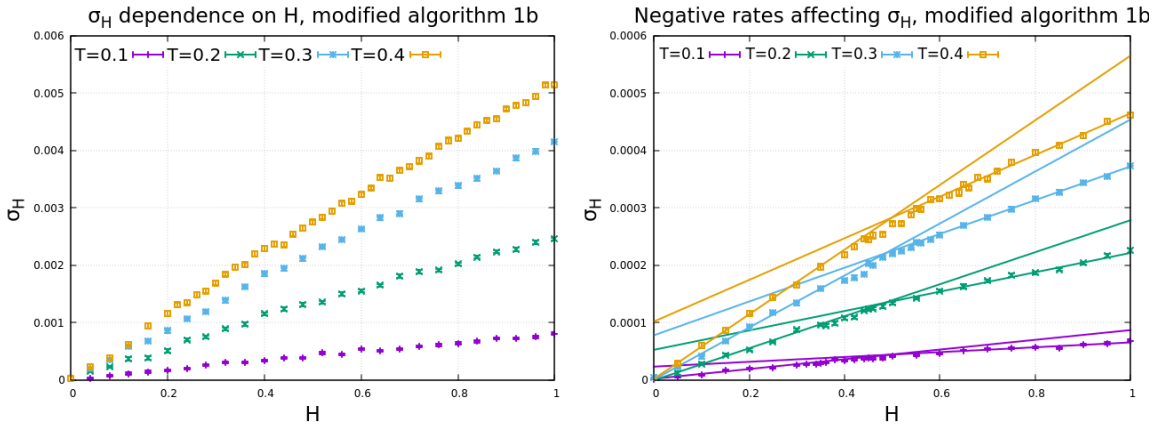

(a) (b)

Figure D.1: (a) Hall conductivity dependence on H when nothing is done to stop negative rates from disturbing simulations. (b) Adjustment $\Gamma_{ikj}^{(n)T} = 0$ used if $\Gamma_{ikj}^{(n)T} < 0$ otherwise.

APPENDIX E

Longitudinal conductivity depenence on H

The effect on σ_x when applying a magnetic field is shown in Fig. E.1 in appendix A. As seen, there is no visible effect for small H but σ_x is increasing with H for large fields in algorithm 2. Experimental results show that σ_x decreases with H. The explanation to the experimental work is magnetoresistance, the magnetic field squeezes the valence electron wavefunction ψ such as to decrease wavefunction overlap between neighboring sites and thus decreasing the conductivity. Magnetic deformations of ψ is not something considered in the development of Eqs. 3.1 and 3.2, and not something considered in these simulations.

The behavior from the two algorithms is clearly different. Algorithm 1b shows close to constant σ_x with variations in H while algorithm 2 shows a steady increase. The increase simulated by algorithm 2 is explained by the phonon probabilities in Γ_{ikj} being larger when moving against $\mathbf{E}$. Therefore $\sum_k \Gamma_{ikj}$ is on average larger when moving against the field than with. And hence the total rate of moving against $\mathbf{E}$ increases with H, increasing σ_x. Perhaps this effect is not felt by algorithm 1b as it only considers one neighbor at a time, while algorithm 2 considers all the important intermediate sites together.

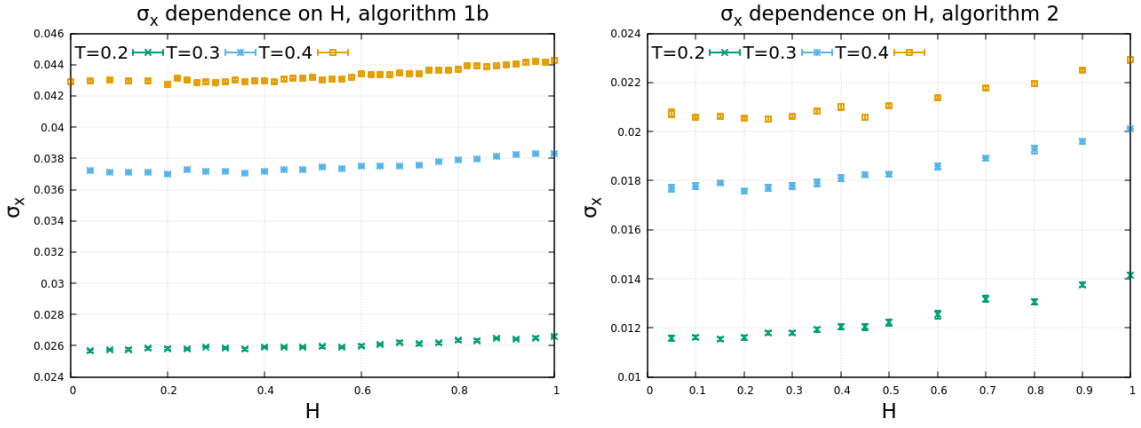

(a) (b)

Figure E.1: σ_x dependence on H for algorithm 1b (a) and alorithm 2 (b). Algorithm 1b finds no σ_x to be seemingly completely independent of H. Algorithm 2 finds a stable σ_x for small H but increasing for large H.